THE INFLUENCE OF REINFORCEMENT ARCHITECTURE ON THE FRACTURE BEHAVIOR OF SELECTIVELY REINFORCED MATERIALS

by

Christopher H. Abada

Thesis submitted to the Faculty of the Virginia Polytechnic Institute and State University in partial fulfillment of the requirements for the degree of

MASTER OF SCIENCE

in

ENGINEERING MECHANICS

M. W. Hyer, Chair
N. E. Dowling
M. P. Singh
G. L. Farley

May 12, 2006
Blacksburg, Virginia

Keywords: Selective Reinforcement, Crack Propagation, Crack Tip Opening Angle

THE INFLUENCE OF REINFORCEMENT ARCHITECTURE ON THE FRACTURE BEHAVIOR OF SELECTIVELY REINFORCED MATERIALS

Christopher H. Abada

ABSTRACT

A computer-based parametric study of the effect of reinforcement architectures on fracture response of aluminum compact-tension (CT) specimens was performed using the finite element code ABAQUS. A three-dimensional crack propagation procedure based on the crack tip opening angle (CTOA) was developed using Python. Eleven different reinforcement architectures consisting of rectangular and triangular cross-section reinforcements were evaluated. Reinforced specimens produced between 13 and 28 percent higher fracture load than achieved with the non-reinforced case. Reinforcements with blunt leading edges (rectangular reinforcements) exhibited superior performance relative to the triangular reinforcements with sharp leading edges. Relative to the rectangular reinforcements, the most important architectural feature was reinforcement thickness. At failure, the reinforcements carried between 58 and 85 percent of the load applied to the specimen, suggesting that there is considerable load transfer between the base material and the reinforcement. The amount of load transfer is linked to strains experienced by the reinforcement ahead of the crack tip.

ACKNOWLEDGEMENTS

First of all, I would like to express my deepest thanks to Prof. Hyer for taking the time to guide me through this work. I would also like to thank Prof. Dowling, Prof. Singh, and Dr. Farley for serving on my graduate committee. I would like to give a special thanks to Dr. Gary Farley at NASA-Langley whose continuous advice and experience was invaluable. I also thank Virginia Tech, the National Institute of Aerospace, and NASA-Langley for this great research opportunity.

I would also like to thank my colleagues and friends at the NIA, NASA-Langley, and the Hampton Roads area; Angela Brickler, Shaun Brown, Jeremy Shidner, Cecile Burg, Neil Kuhn, and many others who have helped to keep me “level” during my graduate research. I would also like to especially thank Tom Jones, Tom Haynie, and the ABAQUS support staff whose technical advice and expertise aided tremendously in this work. Also, I would like to thank all the coffee shop baristas for the caffeinated sleepless nights, as well as the NASA-Langley security officers for letting me in countless times after-hours.

Finally, I would like to thank my friends and my immediate and extended family across the state and across the country for their unwavering love and unrelenting support.

TABLE OF CONTENTS

LIST OF FIGURES

LIST OF TABLES

Chapter 1 INTRODUCTION

The commercial airline industry and military have driven for increased performance and reduced cost of aircraft structural components. Aluminum has been the mainstay material for more than seven decades, fulfilling this role as a strong, lightweight material. However, the aging of current commercial aircraft has raised concerns with regards to the durability and damage tolerance of pressurized aluminum fuselages [1]. Related to this, predicting residual strength has been one of the main objectives of the NASA Aircraft Structural Integrity Program [2].

Aluminum manufacturers have attempted to combat the problems of durability and damage tolerance with advances in alloying techniques. Alcoa, a leading aluminum manufacturer, has developed a number of tailored aluminum alloys for specific parts of the Boeing 777 [3]. For example, a 2000-series aluminum alloy for the fuselage and a high compression strength 7055-T77 aluminum alloy for the upper wing surface were developed.

Although the Boeing 777 illustrates how aluminum is meeting more stringent requirements, it also showcased the potential successor of aluminum as the standard structural material, namely carbon-fiber polymer matrix composites (PMC). Approximately 10 percent of the total weight of the Boeing 777 is composed of carbon-fiber reinforced composites, including most of the tail and rudder assemblies [3]. At that time, this represented the highest use of composites in any Boeing commercial aircraft. The use of high-strength, lightweight composites in the Boeing 777 resulted in an approximate weight savings of 2600 lbs.

Through continuing advances in PMC research, PMC manufacturers have begun to take market share away from aluminum manufacturers. This is becoming more apparent with the recent introduction of the Airbus A380 and Boeing’s up-and-coming 787. Airbus’ A380 is approximately 25 percent composites by weight, including a composite center wing box, pressure bulkhead, and multiple flight control surfaces [4]. Boeing’s 787, to begin major assembly in 2006, is projected to have in excess of 50 percent of its structure composed of composites. This includes the wings and a composite fuselage. According to Michael Bair, the Senior Vice-President of the 787 program, although aluminum manufacturers offered lighter alloys, composites were chosen due to increased strength, decreasing cost, lightweight, "…durability, reduced maintenance requirements, and increased potential for future development." [5].

In order to successfully compete with increasing use of PMC in aerospace structures, aluminum manufacturers must address a number of deficiencies inherent to conventional aluminum. These include, but are not limited to: durability and damage tolerance, specific stiffness and strength, and weight. A study performed by Blichfeldt et al. [6] compared the fatigue and fracture properties of composite structures to all-metal aluminum structures. The study of Blichfeldt et al. [6] showed that compared to aluminum, composite structures gave a 10 to 50 times improvement in fatigue life, as well as improved residual strength-to-weight properties of composites. With respect to stiffness and strength, for a 50 percent fiber volume fraction of a graphite-polymer composite, its fiber direction stiffness is approximately 215 percent greater than aluminum, while its tensile failure stress is about 300 percent greater [7]. To compare weight, the density of a typical carbon-epoxy composite is about 60 percent of commercially available aluminum.

These deficiencies of durability and damage tolerance, and specific stiffness and strength may limit continuing use of aluminum as the primary structural aircraft material. Due to these inherent advantages of PMC's, aluminum manufacturers must now come up with innovative solutions to combat the increased usage of polymer matrix composites in the commercial airline industry.

1.1 Alcoa's 20-20 Vision

Alcoa has presented three concepts to re-establish aluminum's prominence in the aerospace industry: advanced alloys, integral stiffeners, and selective reinforcement [8]. These concepts are part of what is known as Alcoa's 20-20 vision. When applied together, these concepts result in a 20 percent reduction in cost and a 20 percent reduction in structural weight, and make maintaining aluminum's performance competitive with PMCs. Alcoa has focused mainly on several lower wing designs. In order to reduce weight and improve performance, advanced alloys, selective reinforcement, and integral stiffening were used. In order to reduce costs, improved manufacturing concepts, including integral stiffening in conjunction with friction stir welding, were proposed.

One specific concept Alcoa presented, and the main focus of this research, is selective reinforcement (SR). This is a structural design concept where a reinforcing material, such as a unidirectional composite, is applied to specific areas of a structure to improve local or overall performance, such as specific stiffness, strength, durability and damage tolerance, and weight. One advantage to using this approach is that the majority of the base material and structural concepts can remain conventional. This idea resembles, to some extent, that of the integral stiffening concept. Also, since the reinforcements can be less dense than conventional aluminum, a further weight savings can also be realized. Selective reinforcement is a possible solution to the previously mentioned problems inherent with conventional aluminum. Since selective reinforcement is the topic of this research, details of the different approaches to selective reinforcement are discussed.

1.2 Selective Reinforcement

Currently, there are two approaches of selective reinforcement being pursued: the lamination approach and the in-situ approach. Both approaches involve the use of reinforcing material to produce structures having enhanced strength, stiffness, and/or improved durability and damage tolerance.

The lamination approach is the bonding of the reinforcing material onto the surface of an otherwise conventional structure. This is the primary technique that Alcoa has been pursuing, using a fiber-metal laminate, such as GLARE [9]. The lamination concept, as depicted in Figure 1.1 [10], consists of reinforcing material bonded on the inner skin surface near the supporting frame and stringer interfaces. The in-situ approach is defined as the

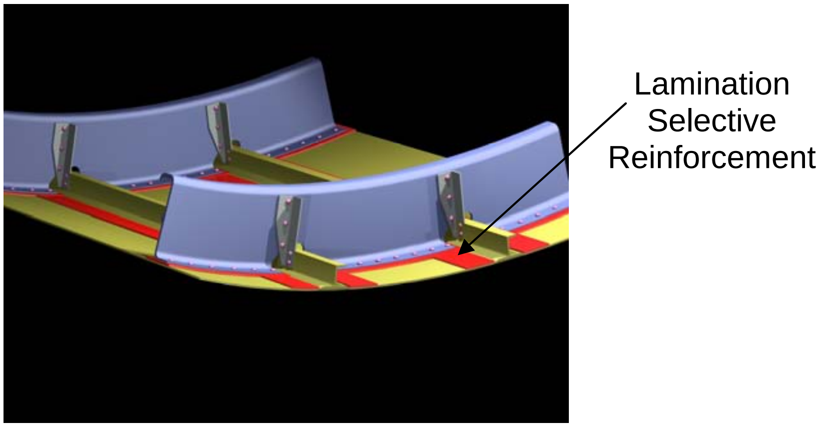

Figure 1.1 Example of Lamination Approach [10]

volumetric replacement of the base material (in this case, aluminum), with a stiffer and/or stronger reinforcement material [11], as depicted in Figure 1.2. The reinforcing material can

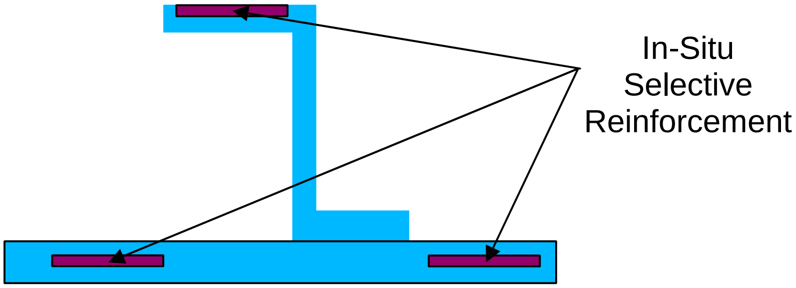

Figure 1.2 Example of In-Situ Approach

be completely embedded anywhere through the thickness of the base material. If the reinforcement is of a lower density than the base material, then both an increase in structural performance, as well as a reduction in structural weight are achieved. Also, discontinuities such as bolt holes, cutouts, or cracks in panels create changes in load path and local stress concentrations. Because of this, local stiffness/strength is decreased, and can lead to catastrophic failure. Selective reinforcement is proposed in this case to increase the local stiffness/strength around geometric discontinuities, in order to provide an adequate load path, thus, in effect, “containing” stress concentrations, and improving overall material response. To more clearly illustrate this concept, Figure 1.3 shows some possible SR skin architectures around cutouts and fastener rows [12].

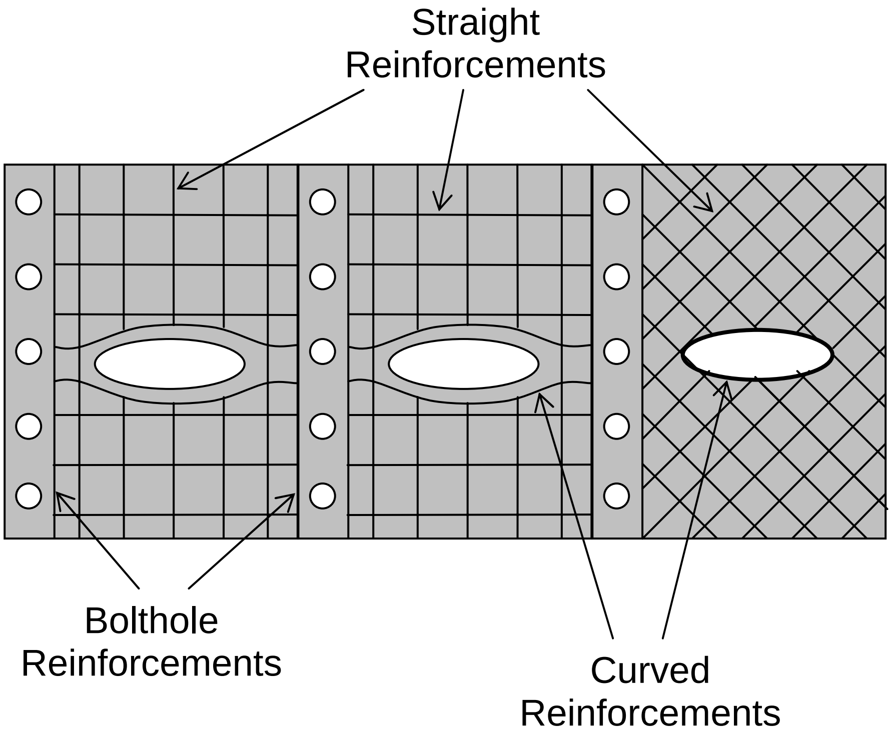

Figure 1.3 Possible In-Situ SR Skin Architectures, Farley et al. [12]

The reinforcing material can be bonded to the base material using a number of different techniques. These include, but are not limited to, welding, a modified pulltrusion technique, or just use of a commercially-available adhesive.

1.3 Objective

The main objective of this research is to develop, through numerical parametric investigation, advanced in-situ selective reinforcement (ISSR) architectures to increase the strength of selectively reinforced metallic materials. Specifically, fracture strength will be considered. The term “architecture” specifically pertains to cross-sectional geometries, reinforcing materials, and combinations of these. The influence of a number of reinforcement architectures on fracture strength is investigated.

The mechanics issues that control the fracture response are also investigated. The investigations include comparisons of the variations of strain and load distributions as a function of reinforcement architecture. Recommendations for reinforcement architectures that lead to significant increases in fracture resistance are given.

Compact-tension (CT) specimen geometries with and without reinforcements are used to assess the fracture strength, which, in this research, will be considered the maximum load experienced by the specimen prior to initiation of unstable crack growth; for the reinforced cases, this corresponds to initial reinforcement failure. Improvement in fracture strength is a measurement of improvement in overall damage tolerance. Eleven different reinforcement architectures with rectangular and triangular cross sections are evaluated.

1.4 Overview of Thesis

A review of literature which discusses selective reinforcement will be provided in Ch. 2. The small amount of research on the in-situ technique, will be reviewed. A review of fracture mechanics related to crack propagation criteria and modelling will also be presented. At the end of Ch. 2, the fracture and material modelling methods to be used in this research will be identified.

The structural modelling of the compact tension specimen, including implementation of the methods discussed in Ch. 2 into the finite-element program ABAQUS, will be discussed in Ch. 3. An unreinforced geometry is described first and is used as a validation case. Comparisons with reinforced geometries are also made. The compact tension geometry, including specimen dimensions and material properties for the base material and reinforcement, will be described. A brief description of ABAQUS and justification for the type of elements used will also be presented. Representative finite-element meshes will be presented to help visualize model generation. The user-written algorithms associated with base material fracture will also be described.

The case studies of the various reinforcement architectures will be presented in Ch. 4. Dimensions, constituent materials, and rationale for investigating each architecture will be provided.

Numerical results for each of the validation cases and for each of the case studies of the different reinforcement architectures will be described in Ch. 5. Discussions of the important mechanics issues will be presented to provide insight as to why certain architectures have superior performance. Before closing this chapter, the results will be summarized in table form to provide a quick overview of the important findings.

Conclusions regarding in-situ selective reinforcement for the specific architectures will be presented in Ch. 6. Finally, in Chapter 6, peripheral comments regarding this research will be made and suggestions for future work will be presented.

Chapter 2 REVIEW OF RELEVANT LITERATURE

2.1 In-Situ Selective Reinforcement

Farley et al. [12] performed a number of two-dimensional parametric numerical studies to assess the fatigue and fracture behavior of in-situ selectively reinforced 7075 aluminum. In this work, a compact tension geometry was considered and the crack tip opening angle was used as the crack propagation criterion.

Examples of the compact tension specimens analysed by Farley et al. [12] are shown in Figure 2.1. The unreinforced specimen is constructed completely of the base 7075 aluminum. The reinforced specimen contains rectangular strips of reinforcing material at the outer surfaces. The cross-sectional geometry of the two reinforcing strips shown in Figure 2.1 is rectangular, and the strips replace the base material at the outer surface on both sides of the specimen. In the current study, cross-sectional reinforcement geometries other than rectangular, and placement of the reinforcement at other locations through the thickness will be considered.

Some experimental data were given for the unreinforced case and a single specific reinforced case. Reinforcement thickness, reinforcement width, and interface stiffness between the base material and reinforcement were all varied in the numerical analysis. The composite reinforcement cross-section was assumed to be rectangular, as the analysis was only two-dimensional. The reinforcement was a unidirectional fiber composite, which failed once the maximum strength of the reinforcement was reached in the fiber direction. This study showed that the fracture toughness of the compact tension specimen, as measured by the maximum load achieved, can be increased by up to 20 percent relative to the unreinforced case when some of the base material is replaced with reinforcement material. It should also

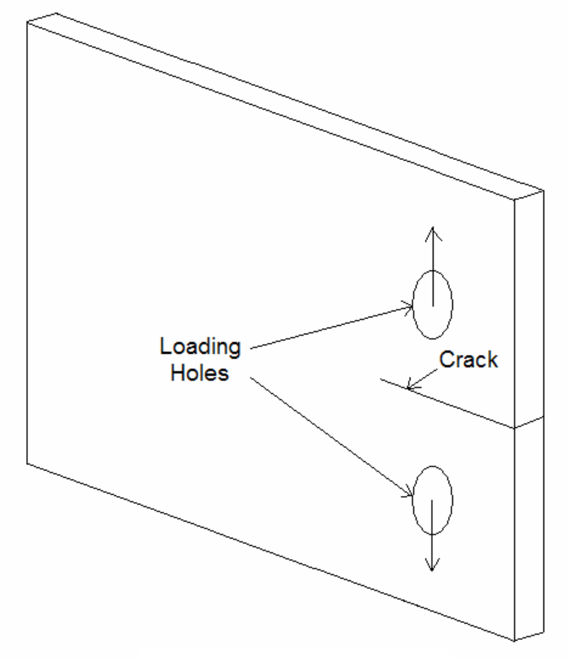

a) Unreinforced

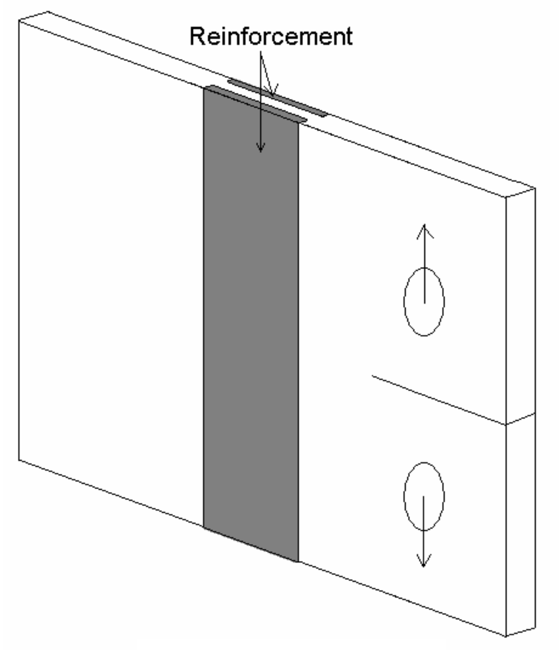

b) Reinforced

Figure 2.1 Unreinforced and Reinforced Compact Tension Specimens be noted for this study that only the applied load and surface crack length were measured in the experimental work with the specific cases tested. No other experimental measurements were taken, in particular, the crack tip opening angle.

For the present research, the same compact-tension specimen geometry, base material, composite reinforcement, and crack propagation criteria employed by Farley et al. [12] are used. ABAQUS [13], a general-purpose, commercially-available finite element code is used to model and analyze each reinforcement architecture considered. In order to benchmark the current analysis, the numerical and experimental results from Farley et al. [12] for an unreinforced specimen geometry are compared to results obtained in the present research. Comparisons for select reinforced specimen geometries are also discussed. Since non-rectangular reinforcement cross-sectional geometries and placement of specific reinforcement cross-sectional geometries at different locations through the thickness are considered in the present research, the two-dimensional analysis used from Farley et al. [12] is insufficient. Therefore, a full three-dimensional analysis is developed. Before this three-dimensional analysis is discussed, a description of the compact tension specimen is given, including previous research, both experimental and finite element modelling, and plasticity modelling. Important through-thickness effects in a thin, ductile material with a propagating crack are also included.

2.2 The Compact Tension Specimen

The compact tension specimen considered here is a standard specimen configuration used to measure the fracture toughness of metallic materials containing a crack [14]. A typical geometry is given in Figure 2.2 along with the coordinate system that will be used in subsequent discussions, where the dimensions are given below, along with typical values of each given in parenthesis:

B = specimen thickness (0.1 inches)

H = specimen height (2.9 inches)

W = specimen width (2.4 inches)

a = surface crack length measured perpendicular from the applied load’s line of action (0.265 inches)

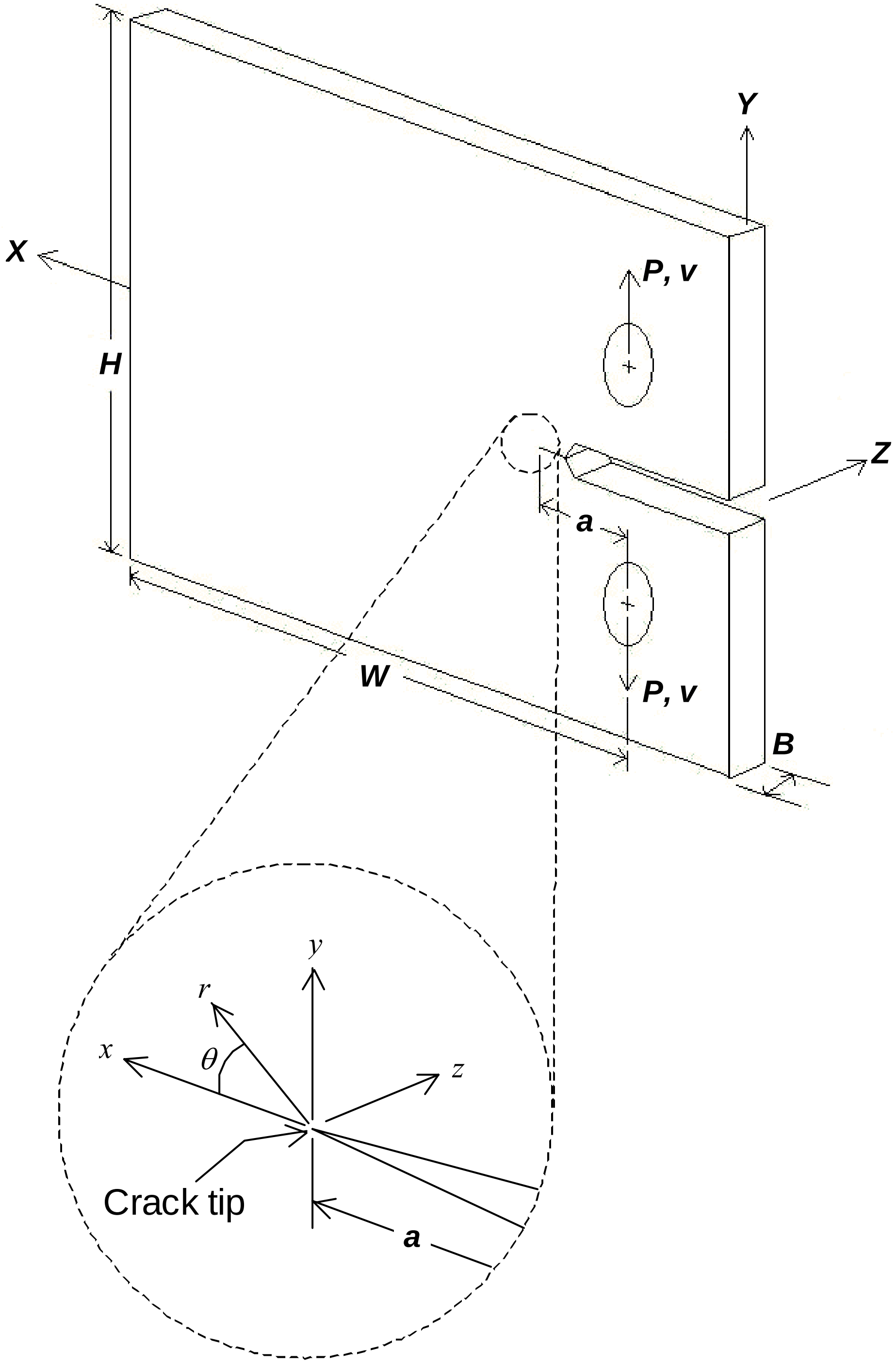

Figure 2.2 Typical Geometry of Compact Tension Specimen

v = applied displacement at point of load measurement

P = applied load

The specimen is designed for a Mode I loading by way of two pins through the two holes in the specimen. To achieve a sharp crack tip, the specimen is initially cracked by cycling the specimen to produce a sharp fatigue crack. The ratio between the minimum load in the cycle to the maximum load, typically referred to as R, is a value between –1 to +0.1. The maximum load in the cycle is chosen such that its calculated stress intensity factor, K, is less than 60 percent of the estimated plane-strain fracture toughness, K_{Ic}, of the material. The stress intensity factor, which is a function of loading and geometry, is used to characterize the severity of the crack. After the sharp fatigue crack has been created, a displacement is applied at the pin locations in opposing directions normal to the crack plane, and the reaction force is recorded. By measuring specific physical variables during the experiment, K_{Ic} for the material can be calculated. The plane-strain fracture toughness, K_{Ic}, is considered a material property for specific combinations of loading and geometry, and is a lower limiting value for the fracture toughness.

Important in these tests is knowledge of the direction in which the specimen material was rolled, extruded, or forged. Since cracking results from void nucleation and coalescence within grains or grain boundaries, material directions within the specimen have an influence on fracture response. The direction in which the material was rolled, extruded, or forged is referred to as the "*L*" direction, while the direction perpendicular to that is referred to as the "*T*" direction. Therefore, a compact tension specimen with the *T-L* orientation will have primary crack propagation in the direction of extrusion; while a specimen with the *L-T* orientation will have primary crack propagation in the direction perpendicular to the extrusion direction. Generally, compact tension specimens with the *L-T* orientation exhibit higher fracture toughnesses than compact tension specimens with the *T-L* orientation due to the tendency for grain boundaries to be oriented parallel to the extrusion direction, and thus the crack propagation direction [15].

In order for the results from the specimen configuration of Figure 2.1 to be considered valid for a linear-elastic fracture mechanics, LEFM, approximation, the plastic zone around the propagating crack tip must not extend to any of the specimen boundaries in the X or Y directions. A distance from these boundaries of four times the plastic zone size is considered sufficient. Dowling [15] gave equations for an estimation of the plastic zone sizes, $2r_0$, for both plane-stress and plane-strain conditions, namely,

$$2r_{0\sigma} = \frac{1}{\pi}\left(\frac{K}{\sigma_0}\right)^2 \quad \text{(For plane stress)} \qquad \text{(Eq. 2.1)}$$

$$2r_{0\varepsilon} = \frac{1}{3\pi}\left(\frac{K}{\sigma_0}\right)^2 \quad \text{(For plane strain)} \qquad \text{(Eq. 2.2)}$$

where

K = Stress intensity factor (60 ksi-in$^{1/2}$)

σ_0 = Yield stress (72.5 ksi)

For the compact tension specimen, K is calculated from [15] as

$$K = F_P\left(\frac{P}{B\sqrt{W}}\right) \qquad \text{(Eq. 2.3)}$$

where

$$F_P = \frac{2+\alpha}{(1-\alpha)^{3/2}}\left(0.886 + 4.64\alpha - 13.32\alpha^2 + 14.72\alpha^3 - 5.6\alpha^4\right) \qquad \text{(Eq. 2.4)}$$

and

$$\alpha = \frac{a}{W} \qquad \text{(Eq. 2.5)}$$

These estimates of plastic zone sizes lead to a number of requirements on in-plane dimensions, including starter crack length. Linear-elastic fracture mechanics is applicable if the equation below is satisfied [15]:

$$a, (W-a), \frac{H}{2} \geq \frac{4}{\pi}\left(\frac{K}{\sigma_0}\right)^2 \qquad \text{(Eq. 2.6)}$$

As seen, the equation uses four times the estimated plane-stress plastic zone size. As will be shown later, for the specimen of Farley et al. [12], the above geometric constraints are not satisfied. The plane-strain fracture toughness, K_{Ic}, is only valid for a compact tension specimen thickness, B, approximately equal to one-half of the width, W [14], a rather thick specimen relative to the current study. This constraint on specimen dimensions ensures that the thickness is large compared to the plastic zone. Therefore, for a large portion of the thickness, the size of the plastic zone is nearly the same as it is at the midplane, or Z = 0 location, thus minimizing boundary effects, similar to the in-plane dimension restrictions for starter crack length and in-plane dimensions. The following equation is the requirement for a plane-strain condition:

$$B \geq 2.5\left(\frac{K}{\sigma_0}\right)^2 \qquad \text{(Eq. 2.7)}$$

In the present research, the specimen is considered sufficiently thin, and thus is closer to a plane-stress condition than a plane-strain condition. Therefore, since both LEFM and plane-strain are not satisfied, using the critical value of K_{Ic} is not a valid crack propagation criterion.

2.2.1 Stress and Strain Estimates Using LEFM

Although LEFM may not be considered valid for the present research in the strict definition of Equation 2.6, approximations to the stress and strain fields can still be made by assuming linear elasticity is valid. The equations below from Dowling [15] are used to estimate stress and strain distributions. These equations assume a purely two-dimensional (X-Y plane) problem, with either an out-of-plane (Z-direction) plane-stress or plane-strain assumption:

$$\begin{aligned}
\sigma_x &= \frac{K}{\sqrt{2\pi r}}\cos\frac{\theta}{2}\left(1-\sin\frac{\theta}{2}\sin\frac{3\theta}{2}\right) \\
\sigma_y &= \frac{K}{\sqrt{2\pi r}}\cos\frac{\theta}{2}\left(1+\sin\frac{\theta}{2}\sin\frac{3\theta}{2}\right) \\
\tau_{xy} &= \frac{K}{\sqrt{2\pi r}}\cos\frac{\theta}{2}\sin\frac{\theta}{2}\cos\frac{3\theta}{2} && \text{(Eqs. 2.8)} \\
\sigma_z &= 0 && \text{(plane stress)} \\
\sigma_z &= \nu\left(\sigma_x+\sigma_y\right) && \text{(plane strain, } \varepsilon_z = 0\text{)} \\
\tau_{yz} &= \tau_{zx} = 0
\end{aligned}$$

where the x-y-z coordinate system with its origin at the crack tip is shown in Figure 2.2.

r = radial distance from the crack tip

θ = angle measured in the x-y plane up from the positive x-axis (i.e., $\theta = 0$ is along the x-axis

K = stress intensity factor as calculated from previous equations for a compact tension specimen

ν = Poisson's ratio

Strains in the y-direction will also be important, since this is the direction of primary loading and crack opening. The y-direction strains are given by

$$\varepsilon_y = \frac{1}{E}\left(\sigma_y - \nu\left(\sigma_x + \sigma_z\right)\right) \qquad \text{(Eq. 2.9)}$$

where

E = Modulus of elasticity (Young's modulus)

As previously mentioned, these equations are merely linear elastic estimates for stresses and strains within an unreinforced compact tension specimen geometry. Although these equations may not exactly apply, they still may give good estimates to compare with the finite element analysis of the current study. Any gross deviations without obvious justifications may help to pinpoint any model deficiencies (i.e., element type, element size, crack propagation procedure, etc.).

Dowling [15] also gives equations that estimate stress and strain variations beyond LEFM. These estimates adjust for the plastic zone by using the elastic field stress equations (Equations 2.8) for a hypothetical crack of length

$$a_e = a + r_{0\sigma} \qquad \text{(Eq. 2.10)}$$

As Equation 2.1 shows, assuming plane-stress, the plastic zone size, $r_{0\sigma}$, is dependent on K, which is dependent on a. This leads to a different form for the calculation of K, specifically,

$$K_e = F_{P,e}\left(\frac{P}{B\sqrt{W}}\right) \qquad \text{(Eq. 2.11)}$$

where, similar to Equation 2.4,

$$F_{P,e} = F_{P,e}\left(\alpha_e\right) = F_{P,e}\left(\frac{a_e}{W}\right) \qquad \text{(Eq. 2.12)}$$

This requires an iterative solution due to the interdependence of the different variables, a_e, $r_{0\sigma}$, and K_e. Once K_e has converged, Equations 2.8 and 2.9 are used to calculate the stress and strain fields. However, it is important to keep in mind that these estimates are for the hypothetical crack length of Equation 2.10, therefore the strain field calculations must be shifted accordingly.

Equations 2.8 are only valid for the unreinforced compact tension specimen, since any inclusion of reinforcement introduces a material discontinuity and local stiffening effects as the crack approaches the region where the reinforcement resides. However, strain variations within the unreinforced specimen help reveal areas of high strain. How these variations change with reinforcement architecture helps to show how one architecture performs better than another, which is a main objective of this research.

2.3 Crack Propagation Criterion

Since K_{Ic} cannot be considered as the crack propagation criterion for the current problem, previous research regarding crack propagation criteria will be mentioned. Specifically, for a certain class of materials and geometries, the material stress intensity factor, K_c, has been used to accurately predict the onset of crack propagation [15]. However, as previously mentioned, this assumes that the plastic zone size is relatively small compared to specimen dimensions, thus limiting use of the material stress intensity factor in fracture research. A reasonably geometry-independent fracture criterion would be preferred for application to large crack growth and large-scale plasticity problems that are beyond the scope of linear-elastic fracture mechanics [16, 17]. A logical fracture criterion would be the J-contour integral. This criterion has had a long history of use to characterize crack growth beyond LEFM, however, recent findings from Yang et al. [18] conclude that J_c is geometry dependent. Others have seen this phenomenon, stating that J_c and the J-R curve are geometry dependent [19 - 21].

The crack tip opening displacement (CTOD) criterion, developed by Wells [22], has been proposed as another crack growth criterion for elastic-perfectly plastic materials. Basically, the criterion states that when the crack tip opening displacement reaches a critical value, the crack will propagate. Considerable analytical, numerical, and experimental research has been performed which supports the use of CTOD as a valid fracture criterion for large-scale plasticity problems. Several types of CTOD measurements exist. The CTOD measurement Rice proposed for a stationary crack [23] was defined to be the opening displacement, δ_{45}, where lines drawn at a 45-degree inclination from the crack tip intercept the crack faces, such as illustrated in Figure 2.3. Research conducted by Shih, et al. [24] and later by Hellman and Schwalbe [25] defined the CTOD as the relative displacement, δ_5, of two points placed 5 mm above and below the original fatigue crack tip location, as shown in Figure 2.3. Andersson [26] and de Koning [27] proposed an alternate use of the CTOD criterion, namely the crack tip opening angle (CTOA). The CTOA criterion has been used by many for fracture studies in thin sheet metals, including Farley et al. [12] for the study of in-situ selectively reinforced aluminum. This criterion assumes that a crack will propagate when the angle, Ψ, created by the two crack surfaces reaches a critical value, Ψ_c. This is

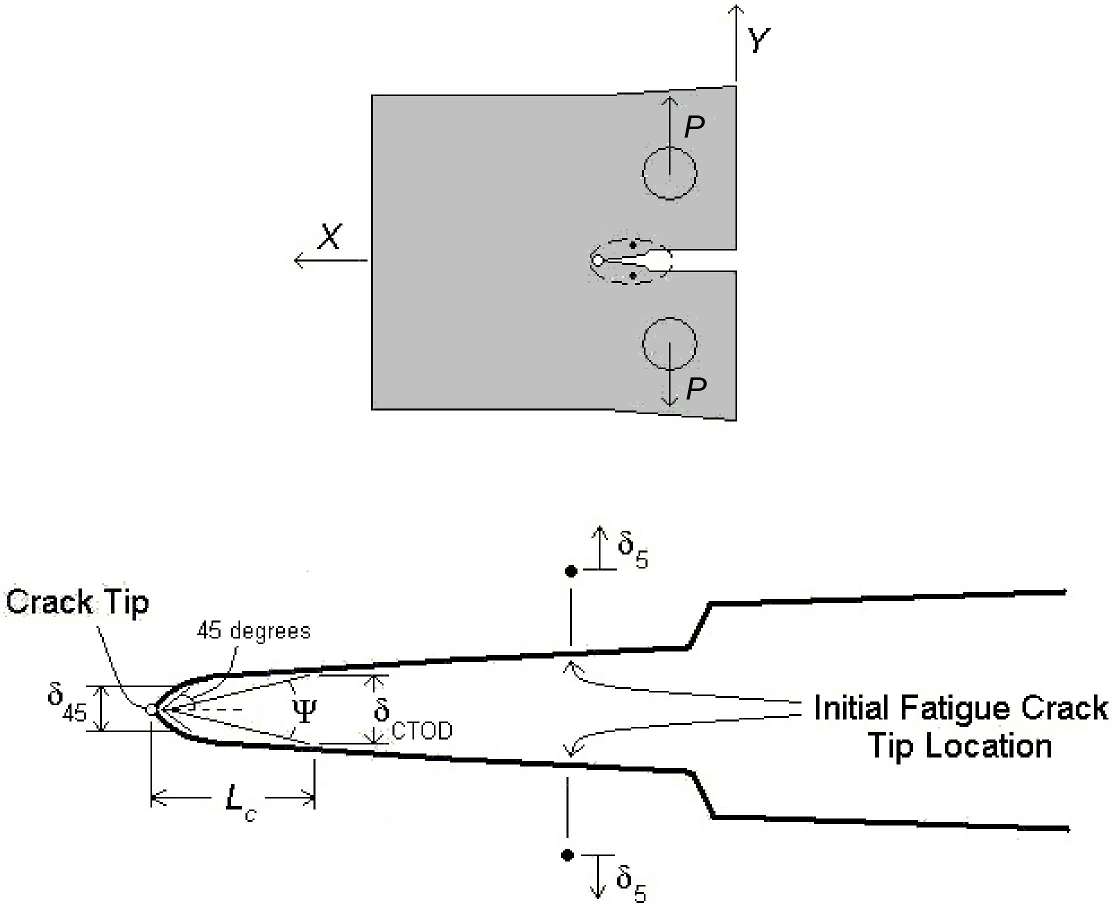

Figure 2.3 Four Different CTOA/CTOD Measurements

directly related to the crack tip opening displacement criterion through the following equation [16]:

$$\Psi = 2\tan^{-1}\left(\frac{\delta_{CTOD}}{L_c}\right) \qquad \text{(Eq. 2.13)}$$

where Ψ is the CTOA and L_c is the distance from the crack tip to the location where the crack tip opening displacement, δ_{CTOD}, is measured. These geometric quantities are illustrated in Figure 2.3. The CTOA criterion has also been extended to full three-dimensional problems, as will be shown later.

The majority of CTOA-based experimental and numerical crack propagation analyses of aluminum structures [16, 17], including Farley et al. [12], has used a constant value of L_c = 1 mm = 0.04 in. This value will be used in the current research as well. However, Sutton et al. [17] suggested some reasoning for the choice of L_c. If L_c is too small, it may be too close to the crack tip to accurately capture displacements when conducting numerical analyses of crack propagation for certain finite element meshes. If L_c is too large, remote-field displacements may be included in the measurement. The use and implications of L_c in both a numerical and experimental analysis will be discussed later in further detail.

2.4 Crack Tip Opening Angle

As mentioned, the CTOA criterion has been used previously for numerical studies of selectively reinforced metals. The CTOA criterion will be used in this study as well. However, the previous studies have been based on two-dimensional analyses. In the present research, three-dimensional effects are included, and thus a more involved approach to using a CTOA criterion is required. To provide a background on the approach, previous work in two- and three-dimensional crack propagation studies using the CTOA criterion are briefly summarized. Experimental work and observations are discussed first. Then, a detailed description of a three-dimensional CTOA analysis is given in order to define terminology and important concepts, such as crack tunnelling and the variation of the initial critical CTOA. Following this, descriptions of two- and three-dimensional so-called straight crack front CTOA models are presented. Also included are further modelling considerations and suggestions from previous authors when using finite-element modelling. Finally, drawing from the previous work, several important concepts to be used in this research are presented.

2.4.1 Other Relevant Research

Several experiments during which the critical surface CTOA, i.e., the crack tip opening angle as measured at $Z = \pm B/2$ in Figure 2.4, were measured have been performed for a number of different 2024 aluminum plate thicknesses and geometries. The experiments, performed by Demofonti and Rizzi [28] and Dawicke et al. [16, 29, 30] on specimens with a central crack and with compact tension specimens showed that during initial crack growth, or during a crack growth length of approximately one specimen thickness, critical CTOAs measured on the surface of the specimen were high compared to values for longer surface crack lengths. After this initial crack growth phase, further crack growth occurred and the critical CTOAs measured on the surface gradually decreased, maintaining an approximately constant value.

Crack tunnelling was also observed in these experimental tests. Tunnelling is the phrase used to refer to the fact that a crack propagates further in the interior of the specimen, i.e., at $Z = 0$ in Figure 2.4, than at the surface. Tunnelling is a result of the existence of a high triaxial stress state in the interior of the specimen as compared to a planar-like stress state at the free surface, where the normal and shear stresses on the free surface, three of the six stress components, must be zero. Enhanced void growth and coalescence would be expected to occur at the midplane, as Sutton et al. [17] suggests. A triaxial stress state was also predicted in several straight crack-front finite-element models from Nakamura and Parks [31] and Newman et al. [32]. The illustration of tunnelling in Figure 2.4 also illustrates the surface CTOA measurement and the measurement distance, L_c. As can be seen, tunnelling results in a curved crack front. The distance away from the crack tip, L_c, used in this experiment from Dawicke et al. [16] was the value mentioned previously, namely, $L_c = 1$ mm $= 0.04$ in. This value of L_c may have been chosen based on the resolution of the CTOA measurement techniques used in those experiments. One measurement technique Dawicke et al. [16] employed involved the use of an optical microscope. The microscope had a resolution of 4 microns over an image area of 2 mm by 2 mm square. It would make sense that the distance L_c be approximately equal to or less than the image area.

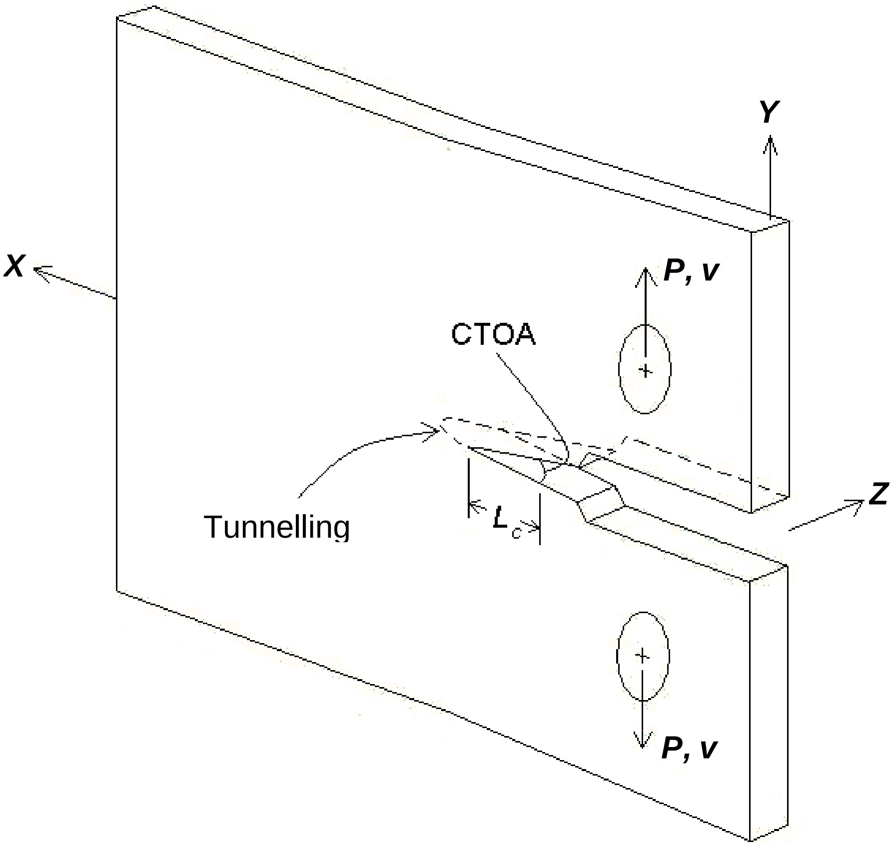

Figure 2.4 Tunnelling with CTOA Surface Measurement and distance L_c

Experimental work from James et al. [33] linked tunnelling effects to fracture surface orientation. For thicker materials, the fracture surface remains perpendicular to the free surface, i.e., perpendicular to the X-Y plane in Figure 2.4, due to the dominance of plane-strain effects. For thinner materials, the fracture surface is not perpendicular to the free surface. In this case the fracture surface is initially flat, then it tunnels, then rotates about the X-axis as it progresses due to the plane-stress [15] conditions at the free surface causing a 45-degree fracture plane. Results from Hom and McMeeking [34] using a straight crack front model showed these 45-degree bands of high strain along the direction of crack propagation. However, Dawicke et al. [16, 29] found that orientation of the fracture surface is also highly dependent on the direction in which the specimen is created, even for fairly thin specimens (e.g., B = 2.3 mm). Dawicke et al. [16, 29] found that for specimens made of 2024 aluminum, *T-L* oriented specimens displayed perpendicular fracture surfaces, while *L-T* oriented specimens displayed rotated fracture surfaces. For a specimen thickness approximately three times this, James et al. [33] observed both perpendicular and rotated fracture surfaces in the *L-T* specimens tested. The observation of both orientations of fracture surfaces may have occurred because the specimen thickness was at a transition point between sufficiently "thick" and sufficiently "thin." For the two different fracture surface orientations, vastly different degrees of tunnelling were also observed.

The crack growth length, Δa, is defined as the distance from the original fatigued crack tip to the current crack tip location along the X-axis. The following equation is used to quantify the tunnelling magnitude, T [33]:

$$T = \Delta a_m - \Delta a_s \qquad \text{(Eq. 2.14)}$$

where:

Δa_s = crack growth length at the free surface ($Z = \pm B/2$)

Δa_m = crack growth length at the midplane ($Z = 0$)

The quantity T is usually normalized by the specimen thickness B. James et al. [33] showed that for perpendicular fracture surfaces, the tunnelling magnitude rose sharply over the first 1 to 2 specimen thicknesses of surface crack growth, and then levelled off at about 1.1 times the specimen thickness, while Dawicke et al. [29] observed levelling off at over 1.7 times the specimen thickness. For rotated fracture surfaces, James et al. [33] observed that T rose only slightly, dropped and then levelled off after a specimen thickness of surface crack growth to a value of about 0.2 times the specimen thickness. Dawicke et al. [16] observed that for rotated fracture surfaces, T levelled off to a value of approximately 0.4 times the specimen thickness. In this experiment, the specimen with the perpendicular fracture surface exhibited approximately 6 percent higher maximum load than specimens with the rotated fracture surface. The presence or absence of this rotation has important implications regarding finite element modelling of crack propagation, which will be discussed later.

It should be noted that in this research, and most other previous analyses of fracture strength, response curves are given in terms of the *surface* crack length, Δa, despite the fact that there could be considerable crack tunnelling. This is important, because going back to the potential application for this research, for aluminum structures containing fatigue cracks, only surface cracks in the base material can be easily detected by a visual inspection.

Before discussing the various numerical analyses employed to study CTOA, it is worth mentioning that there are a few similarities among all of them, namely, the manner in which crack propagation is simulated. Since in most studies the crack is assumed to grow in a quasi-static fashion, crack propagation can be modelled by a number of static steps. For example, for each increment of crack growth, static force equilibrium is reached in the step prior to additional crack growth, and also at the end of the step after the crack has grown. To propagate the crack, nodal constraints along the crack propagation direction are removed. Furthermore, the application of an increment in applied displacement, force, or stress is a static step as well.

In three-dimensional numerical analyses, response is assumed symmetric with respect to the X-Z and X-Y planes of Figure 2.2, i.e., crack plane symmetry and midplane symmetry. The symmetry conditions are illustrated in Figure 2.5, along with two crack front perspectives that will be shown throughout this research. Although all finite-element analyses mentioned here assume symmetry about the midplane, some of the figures of finite-element models show the full thickness for clarity. It should be mentioned that modelling through the use of quarter symmetry precludes rotation of the fracture surface as the crack propagates in the X-direction.

In order to achieve a full understanding of the displacement fields around the crack tip, Dawicke et al. [29] applied experimental results to a three-dimensional numerical analysis based on 8-node hexahedral elements. The experimental results involved specimens that exhibited perpendicular fracture surfaces. To determine the actual crack front shapes and thus measure tunnelling effects, several specimens underwent fracture testing and stable crack growth was allowed to occur. Testing was stopped at various surface crack lengths.

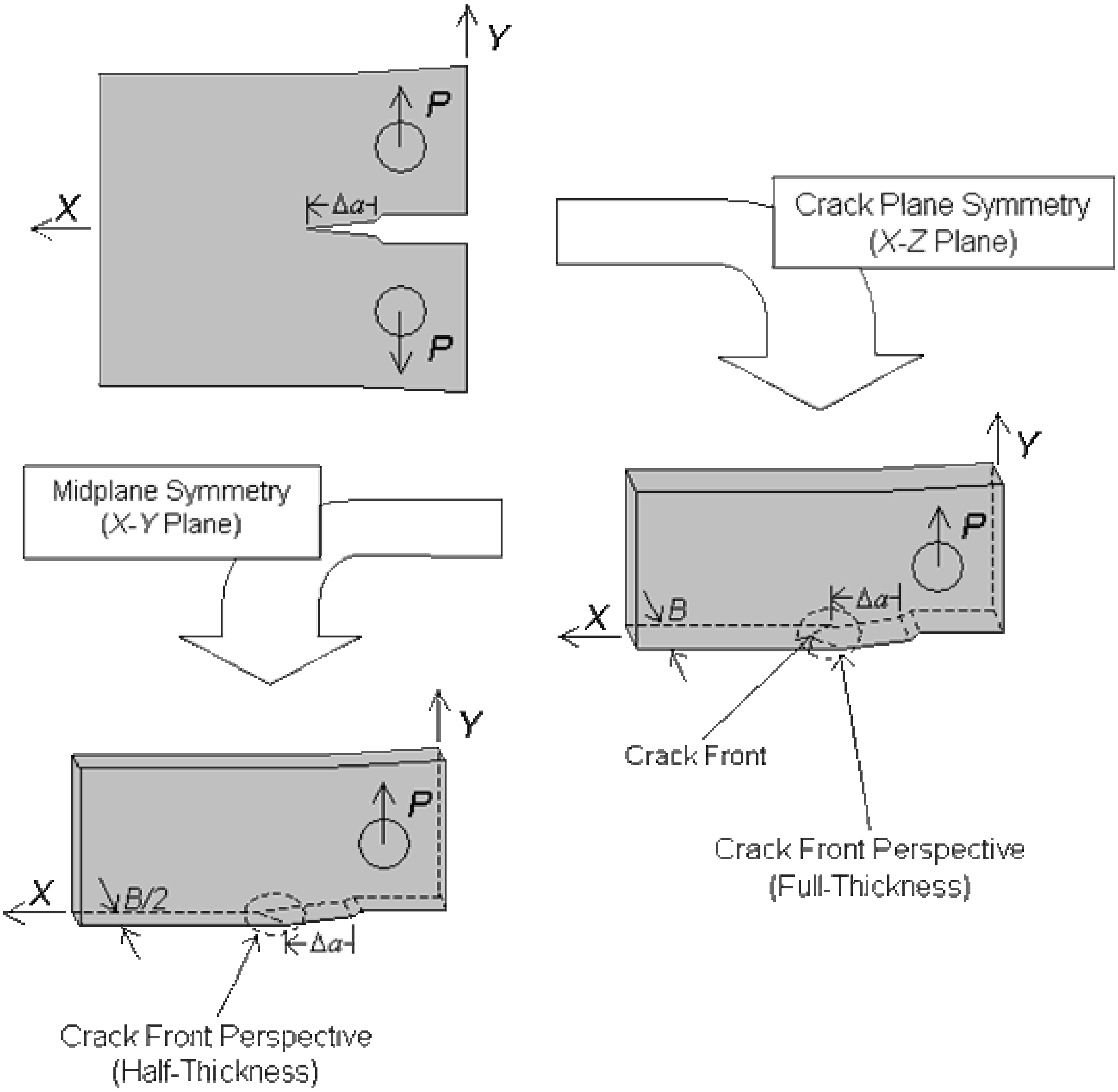

Figure 2.5 Symmetry Considerations for the Compact Tension Specimen Analysis

The specimens were then fatigued at a high cyclic loading rate until failure, and the crack front shape at the end of the further stable crack growth measured. This measurement could be done because the fracture surface created by growing a crack in fatigue appeared different than the fracture surface created by quasi-static stable crack growth and the crack front shape could be identified. Element shapes through the thickness matched the observed crack front shape, as shown in Figure 2.6. To simulate crack propagation, all the nodal constraints along the crack front were removed in the same load step. A curved crack front and nodal constraints are shown in Figure 2.6.

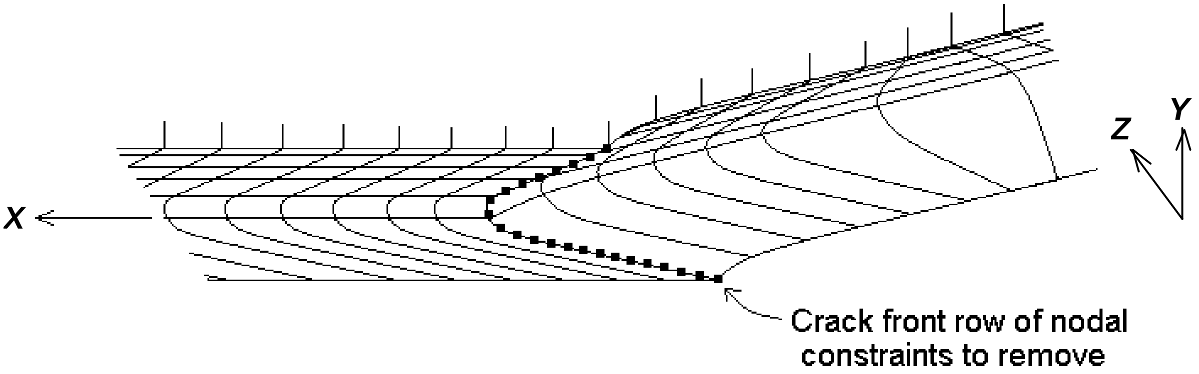

Figure 2.6 Finite Element Mesh of Tunnelled Crack front and Nodal Constraints

The experimentally-determined applied loads were applied to the three-dimensional finite-element model for each increment of crack growth, and the CTOAs were computed at various locations through the thickness using the finite element model. For crack growth lengths, Δa, less than the measurement distance, L_c, the distance at which CTOA was measured was taken at the initial crack tip node. This is shown in Figure 2.7, along with the CTOA measurement distance for larger crack lengths. Using this approach, and comparing

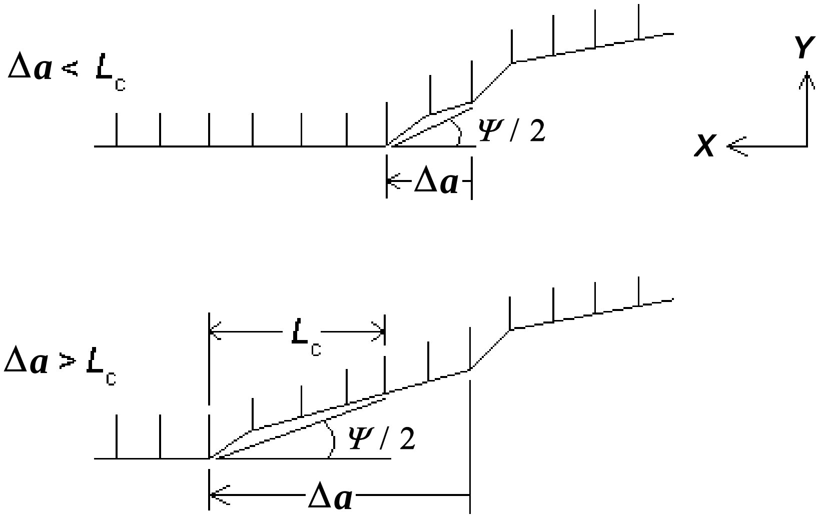

Figure 2.7 CTOA Measurement Distance, L_c, at Two Crack Lengths

the results with the applied loads and surface crack measurements from experiments, the study accurately predicted the through-thickness variation in CTOA. Specifically, during the initial stages of crack growth, i.e., less than a specimen thickness, at the specimen midplane the critical CTOA was computed to be lower than the constant value of the critical CTOA that occurred after a specimen thickness of crack growth. This analysis also showed that the magnitude that the midplane critical CTOA was *below* the constant critical CTOA value was approximately the same magnitude that the free-surface critical CTOA was *above* the constant critical CTOA value. It should be noted that during initial tunnelling, midplane critical CTOA values were not reported in this work of Dawicke et al. [29] due to differences in element size. Along both the free surface and midplane, the measured critical CTOA values converged to the constant value after about a specimen thickness of crack growth.

In this study by Dawicke et al. [29], the analysis was also conducted by assuming a straight crack front, as shown in Figure 2.8. Matching the experimentally determined applied loads and surface crack lengths, the CTOA was measured at both the free surface and the midplane, as shown in Figure 2.8. As expected, there was little variation in critical CTOA through the thickness for the straight crack-front model. However, the initial critical CTOA for the straight crack front was slightly greater than the constant critical CTOA of the curved crack front model just described above by approximately one degree. The critical CTOA for the straight crack front model then also decreased to the constant value after a specimen

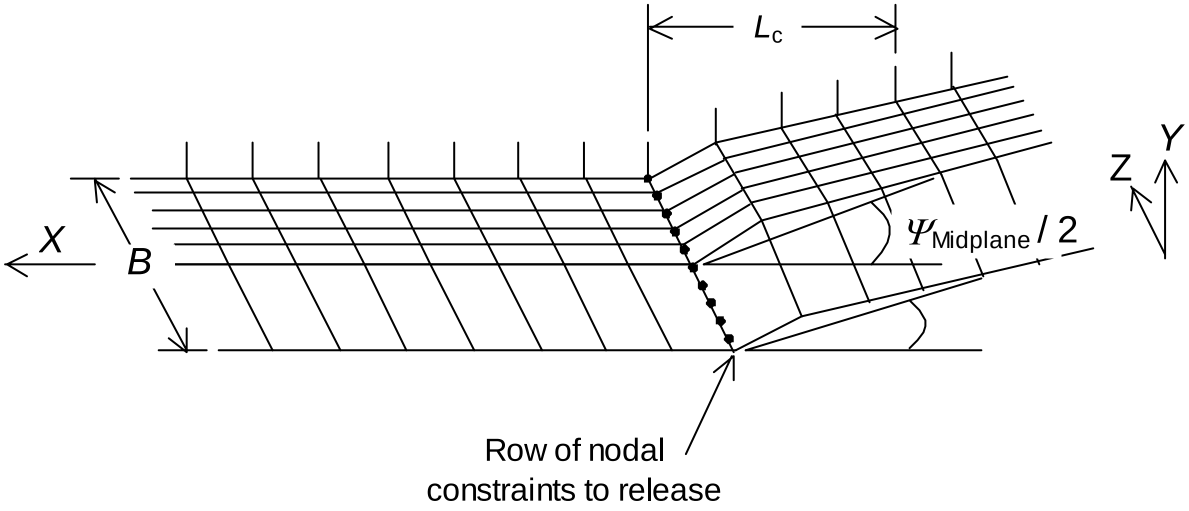

Figure 2.8 Figure Showing Straight Crack Front with CTOA Measurement

thickness of crack growth. The values of the σ_{yy} stresses ahead of the crack tip in the straight crack front model were between the values of the stresses at the midplane and the values at the free surface in the tunnelled model. Since the straight crack front model had an approximately constant critical CTOA value through the thickness (with approximately one degree difference between the initial CTOA and the constant CTOA), and since the stress levels were bracketed between the midplane and free surface values for the model that allowed tunnelling, there is some credence to the use of a two-dimensional approach to predict fracture for relatively thin materials. Verifying the use of a two-dimensional approach was one of the main objectives of this research effort of Dawicke et al. [29].

For investigations conducted using two-dimensional analyses, due to local effects at the crack tip, a compensation must be applied. Specifically, two-dimensional analyses can assume either a plane-stress condition or plane-strain condition prevails. For thin metals in the compact tension configuration [15], the assumption of plane-strain severely underestimates the fracture strength. The assumption of plane-stress, on the other hand, generally overestimates the fracture strength [16]. Because of this bracketing between the plane-stress and plane-strain analyses, using a two-dimensional finite-element model which employs a core of elements along the crack propagation path that satisfies the plane-strain assumption, while modelling the remaining structure with elements that satisfy the plane-stress assumption, is an alternative. This is shown in Figure 2.9, where the dimension of the plane-strain core, $2h$, is adjusted until the fracture response from the numerical analysis matches experiment. Generally, the dimension, h, is approximately equal to the specimen thickness.

Hom and McMeeking [34] first showed this midplane plane-strain phenomenon by numerically analyzing stress fields around a straight crack front in thin elastic-plastic sheets. Their analysis showed that if the specimen is sufficiently thick compared with the crack tip opening, a plane-strain constraint will be present at the midplane of the specimen, near the crack tip, where a triaxial stress state occurs. Plane-stress conditions prevail at the free surface of the crack tip. Therefore, applying the plane-strain assumption around the crack tip in a two-dimensional analysis is necessary.

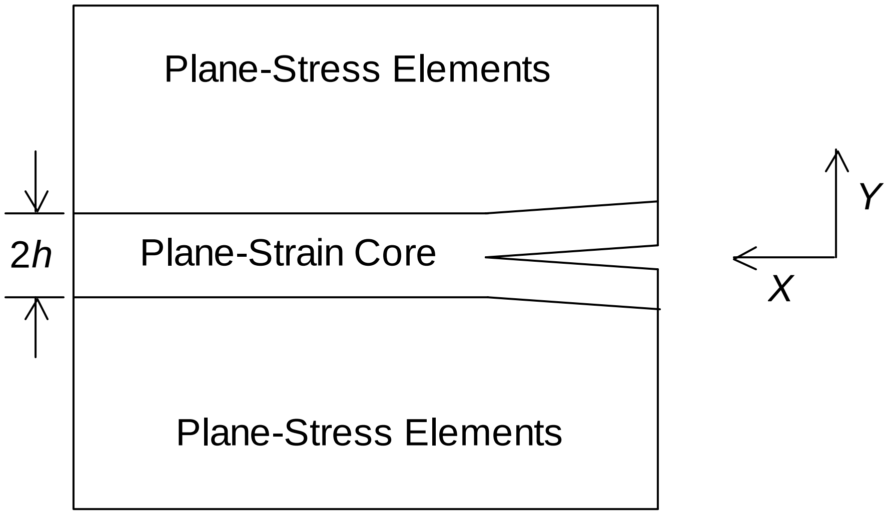

Figure 2.9 Plane-Strain Core Height Measure for 2-D Analysis

Many two-dimensional finite-element analysis based CTOA analyses using a core have been performed to predict fracture as well [16, 17], including Farley et al. [12] for in-situ selectively reinforced metals. These studies have used either triangular or square elements, and have used only the constant critical CTOA throughout the entire crack propagation history. The value of L_c for these cases was equal to the element length in the crack propagation direction.

2.4.2 Considerations for Selectively-Reinforced Materials

Using a two-dimensional approach and employing the concept of a core of plane-strain elements may be appropriate, in some cases, for modelling an unreinforced specimen. However, by placing reinforcement material within the base material, a two-dimensional analysis would not be able to capture important through-the-thickness effects, as mentioned previously. Also, the inclusion of the plane-strain core may not accurately model the stress and strain variations in the base material around the reinforcement ahead of the crack tip. Finally, tunnelling effects would not be captured either. Since various reinforcement geometries and various through-thickness locations for the reinforcements will be investigated in the present study, crack tunnelling may be important. And since understanding of the mechanics issues related to fracture response of selectively reinforced materials is an important objective of the present work, the potential for the existence of important three-dimensional effects must be accounted for. Therefore, as said previously, a three-dimensional analysis will be used.

Most of the three-dimensional finite-element models developed to date have employed a straight crack front and have also used 8-node hexahedral elements. Gullerud et al. [35] accurately described a procedure based on hexahedral elements. Only a single value of critical CTOA was used. The CTOA for these models was measured at the midplane of the specimen, where the highest triaxial stresses occur. This midplane crack tip node was considered the master node. Once the critical CTOA was reached at this master node location, all nodal constraints less than L_c ahead of the crack tip were released, thus simulating crack propagation. The method used for measuring CTOA and nodal release is depicted in Figure 2.10. This three-dimensional straight crack front technique has accurately modelled experimental fracture response. However, as with the two-dimensional approach, crack tunnelling was again not included. The amount of crack tunnelling may change when through-the-thickness reinforcements are considered. Tunnelling effects may change the overall fracture response, and therefore attempts must be made to model them as well.

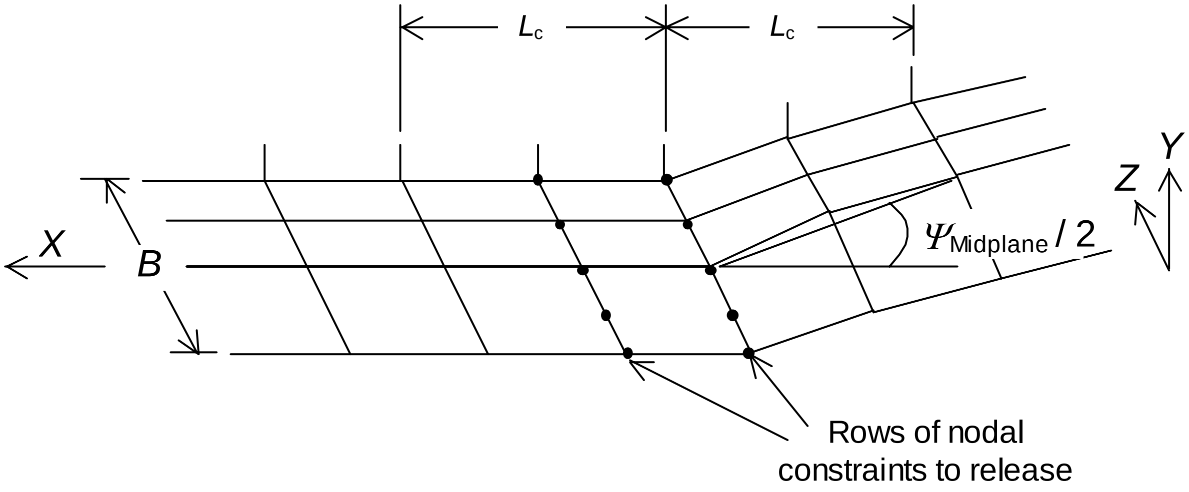

Figure 2.10 Finite Element Model Showing CTOA Measurement for Straight Crack Front and Nodal Release Rows

The finite-element analyses developed to date have assumed that the fracture surface was perpendicular to the free surface, due to the symmetry assumptions used in the analysis. Either perpendicular or rotated fracture surfaces can be assumed, but which one will occur in practice is not always known beforehand. However, the previously mentioned work from

James et al. [33] supports the fact that despite the different orientations of the fracture surface, the overall responses are still similar, and with the maximum load predicted for the perpendicular fracture surface being only slightly greater than the maximum load predicted for a rotated fracture surface, despite vastly different tunnelling characteristics. It should also be noted that neither tunnelling magnitude, nor fracture surface orientation, nor material orientation (*T-L* vs. *L-T*) were discussed by Farley et al. [12]. The current research will assume a perpendicular fracture surface. However, it would be very important to know what effects in-situ selective reinforcement would have on fracture surface orientation, as orientation is closely linked to tunnelling, and vice-versa. Because of the limited scope of the present study, the issue of fracture surface orientation will not be pursued.

Gullerud et al. [35] also described a number of important three-dimensional modelling details related to tunnelling; CTOA measurement distance, the value of L_c; and the coupling of the value of L_c with element size and element aspect ratio. Since the CTOA criterion is a displacement-based fracture criterion, displacement fields in the vicinity of the crack front need to be accurately computed. In order to achieve this using hexahedral elements, an approximately 1:1:1 element geometric aspect ratio must be maintained. This ratio is also recommended for the specific type of hexahedral elements used along the crack front, which will be described in a later chapter. Since tunnelling effects will be included in this analysis, a sufficient number of elements through the thickness must be used. The number of elements used in the current work is based on overall fracture response considerations, and the desire to compare the results of the present work to previous work, where tunnelling was included [33]. In the analysis from Gullerud et al. [35], only two elements through the thickness were used. To keep the element aspect ratio constant requires that the element dimension through the thickness must be equal to the element dimension in the crack propagation direction. This will directly influence the CTOA measurement distance, L_c. In most experimental and analytical studies performed to date, a CTOA measurement distance of $L_c = 0.04$ in. away from the crack tip has been used, as previously mentioned. Since tunnelling was not accounted for in previous two-dimensional and three-dimensional straight crack front models, and therefore the through-the-thickness element dimension not as crucial, these studies either used element dimensions in the crack propagation direction approximately equal to the CTOA measurement distance, L_c, or all nodal constraints less than the measurement distance were released. Therefore, adopting the CTOA measurement technique for crack lengths less than L_c from Dawicke et al. [29] will be required. Also, for a model that includes tunnelling where there are several elements within the measurement distance, L_c, releasing all nodal constraints less than L_c does not make sense. Only a single nodal constraint should be released at a time.

Dawicke et al. [36] also gave suggestions for approximating three-dimensional tunnelling effects in a finite-element model. To approximate tunnelling effects, the displacements at all the nodes along the crack front at a distance L_c behind the crack tip are evaluated, and crack advancement is only allowed at locations through the thickness where the critical CTOA has been achieved. This idea is shown in Figure 2.11, where the crack profiles at different locations through the thickness are illustrated. The terminology crack

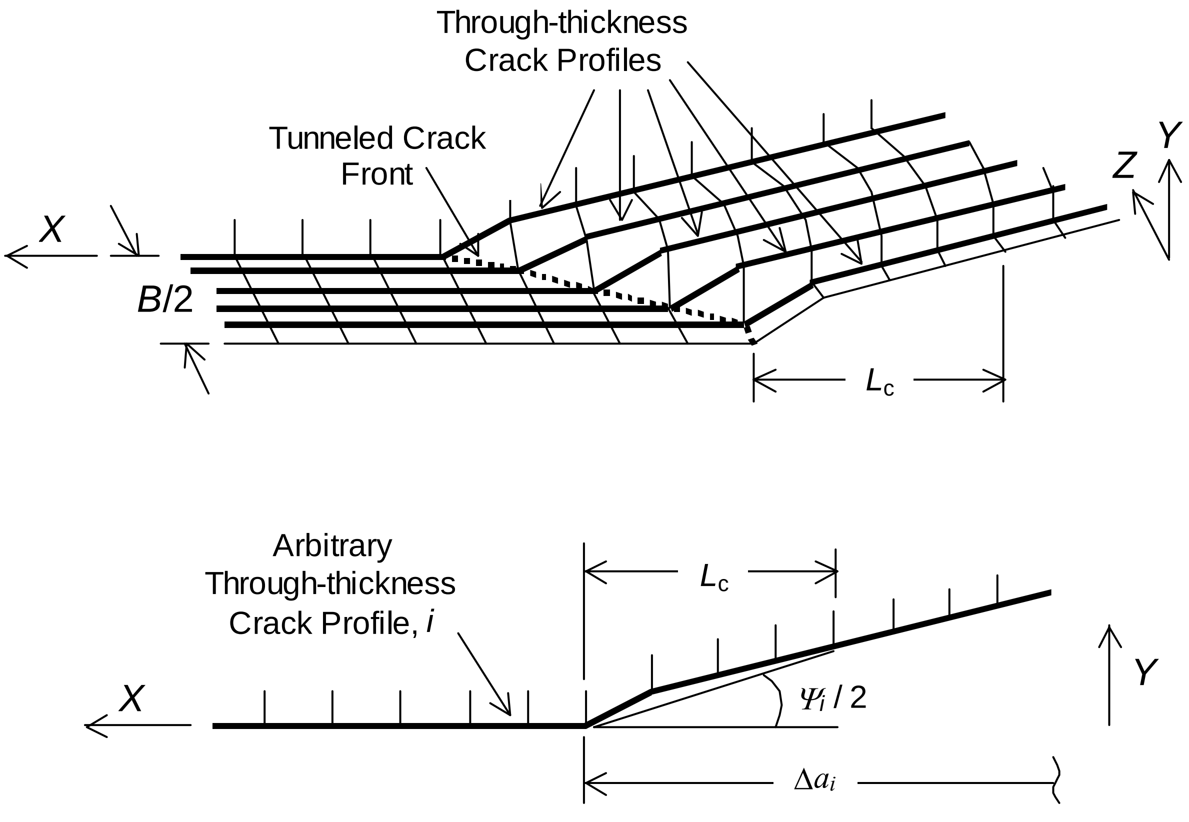

Figure 2.11 CTOA Measurement for Several Different Crack Profiles Through-Thickness

profiles as used here refer to the collection of nodes in planes parallel to the X-Y plane that define the crack opening shape at various Z-locations. The profiles are at various Z-locations identified with an integer, a generic profile being referred to as the ith profile. In Figure 2.11, five crack profiles are illustrated. The research of Dawicke et al. [29, 36] supports this crack advancement approach.

In the two-dimensional and three-dimensional straight crack front finite-element analyses previously mentioned, a single value of critical CTOA is used either at the crack tip, for two-dimensional analyses, or at the midplane for three-dimensional analyses. In these cases, the value of the critical CTOA is found by adjusting the critical value of the CTOA and repeatedly conducting the finite element analyses until the maximum load from the finite-element calculations matches the experimentally-measured maximum load. This is essentially a calibration exercise. Since a calibration specimen was not tested for the current research, the numerical results from Farley et al. [12] with the unreinforced specimen are used for calibration. A straight crack front model is assumed for calibration.

Although using a single value of critical CTOA in a three-dimensional model gives accurate results for maximum load and overall response for larger total crack lengths, in many cases it fails to capture the response at crack lengths less than a plate thickness. Specifically, the crack length computed at maximum load is inaccurate [33, 35 - 37]. For most experiments involving the 2024 aluminum, the finite-element analysis over predicts the surface crack length at maximum load by as much as a specimen thickness, as shown in Figure 2.12 from James et al. [37]. For example, suppose that in experiments the maximum load occurs after a plate thickness of crack growth. Using the single critical CTOA approach in a three-dimensional finite element model, the maximum load may occur at two plate thicknesses of crack growth. The total crack length in the study by Farley et al. [12] is only about three times the specimen thickness. Thus a more accurate measure of surface crack length at maximum load is important. A reason for this discrepancy with the crack length prediction is the simplicity of using a constant value CTOA criterion during initial crack growth, in addition to not accounting for crack tunnelling effects [33, 37]. As Dawicke et al. [16, 29, 30] showed, higher critical surface CTOAs were measured experimentally when crack tunnelling was present. The work from James et al. [33] suggested altering the

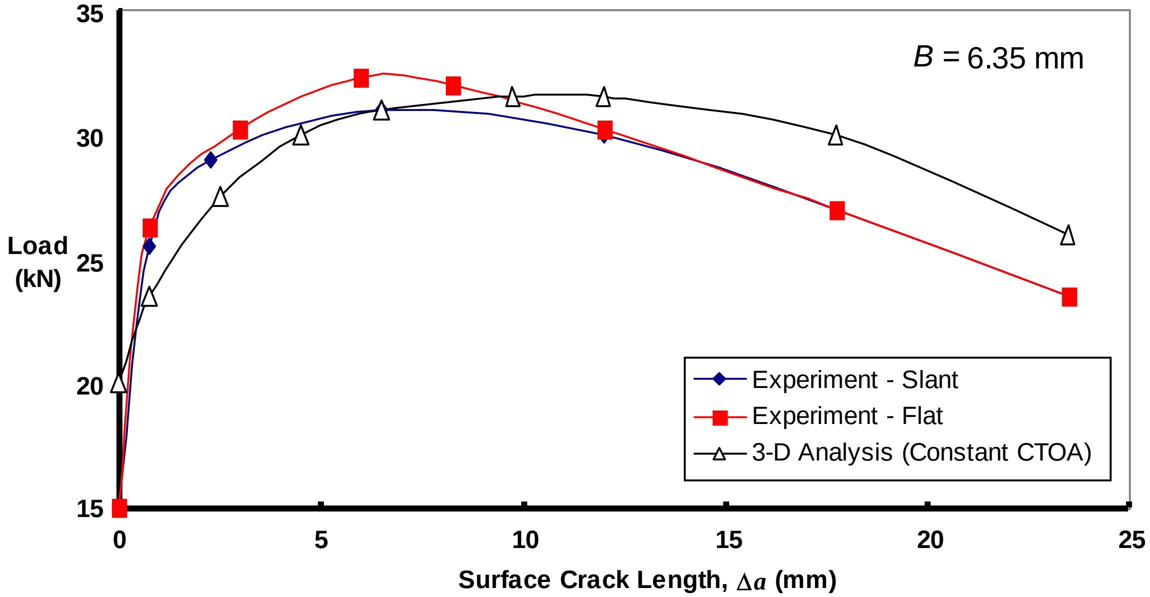

Figure 2.12 Surface Crack Length Overestimation at Max Load for Three-Dimensional Models, James et al. [37]

experimental data (which was done in that particular study), or, more accurately, developing a model that takes into account initial CTOA variation and which also generates its own crack tunnelling by way of the mechanics of the problem. The crack propagation procedure in this current research attempts to develop such a model.

Also illustrated in Figure 2.12 is the difference between a specimen exhibiting a rotated fracture surface, and one exhibiting a flat fracture surface. As previously mentioned, the difference is approximately 6 percent.

Finally, besides the work from Farley et al. [12] supporting the use of CTOA for in-situ selectively reinforced metals, other CTOA-based fracture studies have been performed on metals containing geometric discontinuities. Seshadri and Newman [38] and Dawicke et al. [36] accurately predicted fracture strength in a panel containing multi-site damage using the critical CTOA criterion, in both two-dimensional and three-dimensional straight crack front finite-element analyses. The test by Dawicke et al. [36] consisted of a 0.09 in. thick middle-cracked 2024 aluminum tension specimen, with several other cracks in line with the initial central crack that was created by the fatigue approach. As the central crack grew, it joined with the other cracks and lowered the overall fracture strength of the material. The distance from one end of the central crack to the next adjacent crack was varied from 0.1 to 3 in. The distance from the initial fatigue crack to the leading edge of the reinforcement in the study of Farley et al. [12] was about 0.34 in. Geometric discontinuities such as adjacent cracks in panels with multiple cracks can also be considered a material discontinuity, where, in this case of multiple cracks, the material has zero stiffness. This gives further supporting evidence that the CTOA criterion can be used for in-situ selectively reinforced metals.

Drawing from the points discussed above, the following details of modelling and analysis of CTOA-based crack propagation in selectively-reinforced compact tension specimens will be used in this research:

1) The distance away from the crack tip where the CTOA will be measured is $L_c = 0.04$ in. This distance has been used in a number of different studies involving experimental and numerical analysis and will be employed in the current problem.
2) Tunnelling effects can be approximated by measuring CTOA at nodes located a distance L_c away from crack front locations. Once the CTOA reaches the critical value at a particular crack front location, the constraints at just that corresponding crack front node will be released. This means that a single crack length, Δa is not sufficient, and that CTOA-based crack propagation must be used at each through-thickness crack profile, i, where Δa_i is the crack length along each crack profile from the initial crack tip to the crack front, as shown in Figure 2.11.
3) The elements along the crack propagation plane will be 8-node hexahedral linear displacement elements. These have been used consistently in all three-dimensional crack propagation finite-element models.
4) The elements along the crack propagation plane will maintain an approximately 1:1:1 element aspect ratio.
5) Crack growth will be modelled as a number of consecutive static steps involving applied displacement and nodal constraint release steps, which simulate crack growth, with equilibrium being re-established after each step.

6) For overall crack growth distances shorter than the measurement distance L_c, i.e., right after initial crack tip blunting ($\Delta a_i < L_c$), the point for measuring CTOA will be the node of the blunted crack tip profile, or just Δa_i.
7) For a short distance of crack growth (less than the specimen thickness), a region exists where the critical CTOA will not be constant as a function of crack growth.
8) During this initial phase of crack growth, the critical CTOAs measured are high, and decrease as the crack propagates. CTOA variation during this initial phase of crack growth will be taken into account. This means $\Psi_c = \Psi_c(\Delta a_i)$, for $\Delta a_i < B$.
9) Once crack growth is past this initial phase, the critical CTOA is approximately constant through the thickness of the specimen, and for continued crack growth increments. This means Ψ_c = constant, for $\Delta a_i \geq B$.
10) To obtain the value of the constant critical CTOA, a straight crack front approach is assumed. Pre-determined loads are applied to the model, and the critical CTOA is measured.
11) Crack growth increments are equal to one element length.
12) The compact tension specimen geometry and materials from Farley et al. [12] are used.

With these ideas, the analysis developed in the next chapter is an attempt to accurately model three-dimensional crack propagation, including crack tunnelling and initial CTOA variation in in-situ selectively-reinforced materials.

Chapter 3 ANALYSIS

The purpose of this chapter is to describe the development of the three-dimensional crack propagation modelling procedure applied to the compact tension specimens. An unreinforced specimen is considered first in order to validate the procedure and the finite element mesh. The compact tension specimen geometry, materials, and boundary and symmetry conditions are described in the first section. The finite element program used in this investigation is described in the second section. Considerations of geometric and material nonlinearities, as well as the type of finite elements used, are included. The analysis procedures for crack propagation using the CTOA are described in the next section. The application of some of the procedures from previous authors to the geometry of Farley et al. [12] is considered first. In addition to points mentioned in the literature review, further user-defined approaches to account for element size and the quasi-static analysis are discussed as well. The implementation of the crack propagation procedure into the finite-element program ABAQUS is presented. Validation of the unreinforced model and crack propagation procedure is assessed by comparison with past work. Finally, some reconsiderations for geometry, materials, and mesh are made for the reinforced architectures, and comparisons of reinforced cases from Farley et al. [12] are given.

3.1 Unreinforced Compact Tension Geometry

Continuing with the unreinforced compact tension specimen geometry in Figure 2.1 from Chapter 2, the unreinforced compact tension specimen geometry will be specified in this chapter. Materials used for the unreinforced specimen, along with how they are modelled are also specified. Boundary conditions and symmetry conditions imposed on the model are detailed.

3.1.1 Compact Tension Geometry Dimensions

Figure 3.1 shows the unreinforced compact tension specimen dimensions from Farley et al. [12], which is also used in the present research. As previously mentioned in Chapter 2, this unreinforced case is considered one of the baseline validation cases to compare results from the three-dimensional analysis with the results from Farley et al. [12]. Other cases from Farley et al. [12] are compared later. Knowledge of the unreinforced geometry helps to determine element sizes, and it gives an adequate baseline for developing meshes for the reinforced specimen geometries.

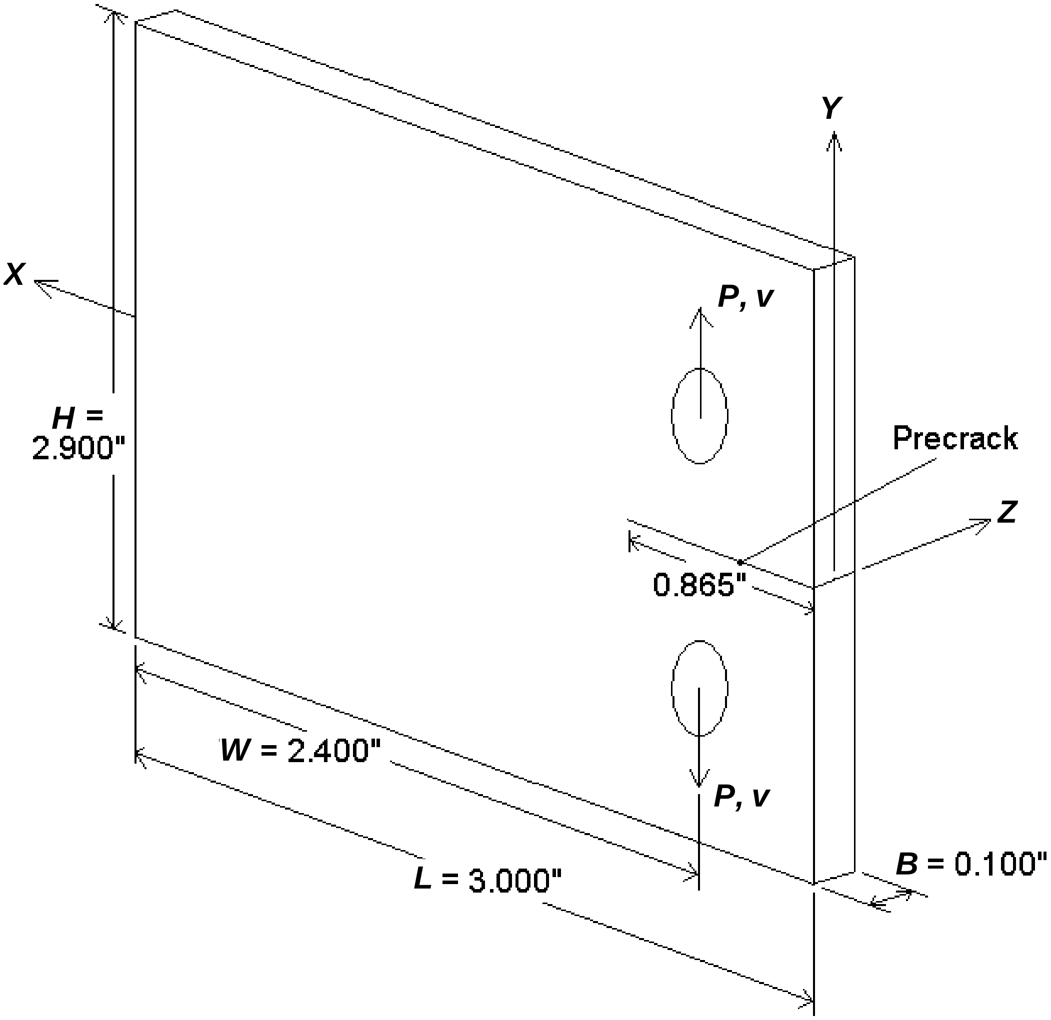

Figure 3.1 Compact Tension Geometry, Dimensions, and Coordinate System

Also shown in Figure 3.1 is the coordinate system that is used herein. As before, the origin lies at the midplane (Z = 0), along the crack plane (Y = 0), and at the surface of the specimen (X = 0). The X-direction is parallel to the crack propagation direction, the Y-direction is parallel to the loading direction, and the Z-direction is directed to conform to the right-hand rule. The initial crack tip (precrack) is also shown in Figure 3.1.

3.1.2 Material Properties

This section details the materials used in the unreinforced compact tension geometry analysis, and how each material is modelled. Table 3.1 lists the mechanical properties and yield stress/strength of the materials used in this analysis. Also included is how the materials are modelled in ABAQUS.

Table 3.1 Properties of Materials Used in Analysis

Material	Elastic Properties	Yield Stress (Strength)	Represented in Analysis
Aluminum 7075-T6	E = 10.0 Msi ν = 0.30	72.5 ksi	Isotropic Elastic-Perfectly Plastic
Steel (Load Introduction Pin)	E = 30 Msi ν = 0.30	N/A	Isotropic Linear-Elastic

The base material through which the crack is propagating is aluminum 7075, and it is modelled as having elastic-perfectly plastic behavior, using the von Mises yield criterion, and the associated plastic flow rule. This is the same material and modelling scheme used in Farley et al. [12]. From Dowling [15], the elastic-perfectly plastic representation of aluminium 7075 appears to be fairly accurate. The load-introduction pin is assumed to be steel, modelled as a linear-elastic material. This is a more accurate representation of the loading pin than used by Farley et al. [12], where the pin material was modelled as a linear-elastic aluminium 7075. In actual compact tension specimen experiments, the loading pins are made of steel. Discussion of how the load from the pin is transferred to the aluminium 7075 is given in the next section.

3.1.3 Boundary and Symmetry Conditions

Due to symmetry in loading and geometry of Figure 3.1, two symmetry planes exist: the through-thickness midplane (the X-Y plane at $Z = 0$), and the crack plane (X-Z plane at $Y = 0$). It is assumed that the crack orientation does not change as it propagates, so only one-quarter of the plate needs to be modelled. These are the same symmetry conditions used in the three-dimensional models mentioned in Chapter 2, shown in Figure 2.5. In order to model the symmetry planes, ABAQUS employs symmetry constraints to the appropriate surfaces. These constraints are considered nodal multipoint constraints that constrain displacement degrees of freedom for 3-D elements. The three boundary constraints are shown in Figure 3.2. On all the nodes at the midplane surface ($Z = 0$), displacements in the Z-direction are constrained ($u_z = 0$). On the nodes along the crack plane ($Y = 0$), excluding the nodes along the precrack, displacements in the Y-direction are constrained ($u_y = 0$), until crack propagation starts. To constrain displacements in the X-direction, nodes along a line through the thickness at $X = L$ and $Y = 0$ are constrained ($u_x = 0$).

To apply the external displacements, a uniform displacement, v, in the Y-direction is applied along a line of nodes parallel to the Z-direction at the center of the load application pin, as shown in Figure 3.3. To transfer the applied load at the pin into the structure, tie constraints are used. This “tie” command in ABAQUS connects two meshed surfaces by requiring that all nodal degrees of freedom on one surface be the same on the connecting surface along the tied surfaces. The nodes do not necessarily have to be coincident, as ABAQUS interpolates displacements between nodes. To more accurately model the actual experiment, a steel pin was used, the pin was modelled as a cylinder, and only the upper-half of the pin was tied to the inner surface of the load application hole, as also shown in Figure 3.3. In the finite-element analysis from Farley et al. [12], the circular geometry of the pin was not modelled. Also from the analysis by Farley et al. [12], the external displacement was applied to a node where the displacement at the pin center would be, and the connecting

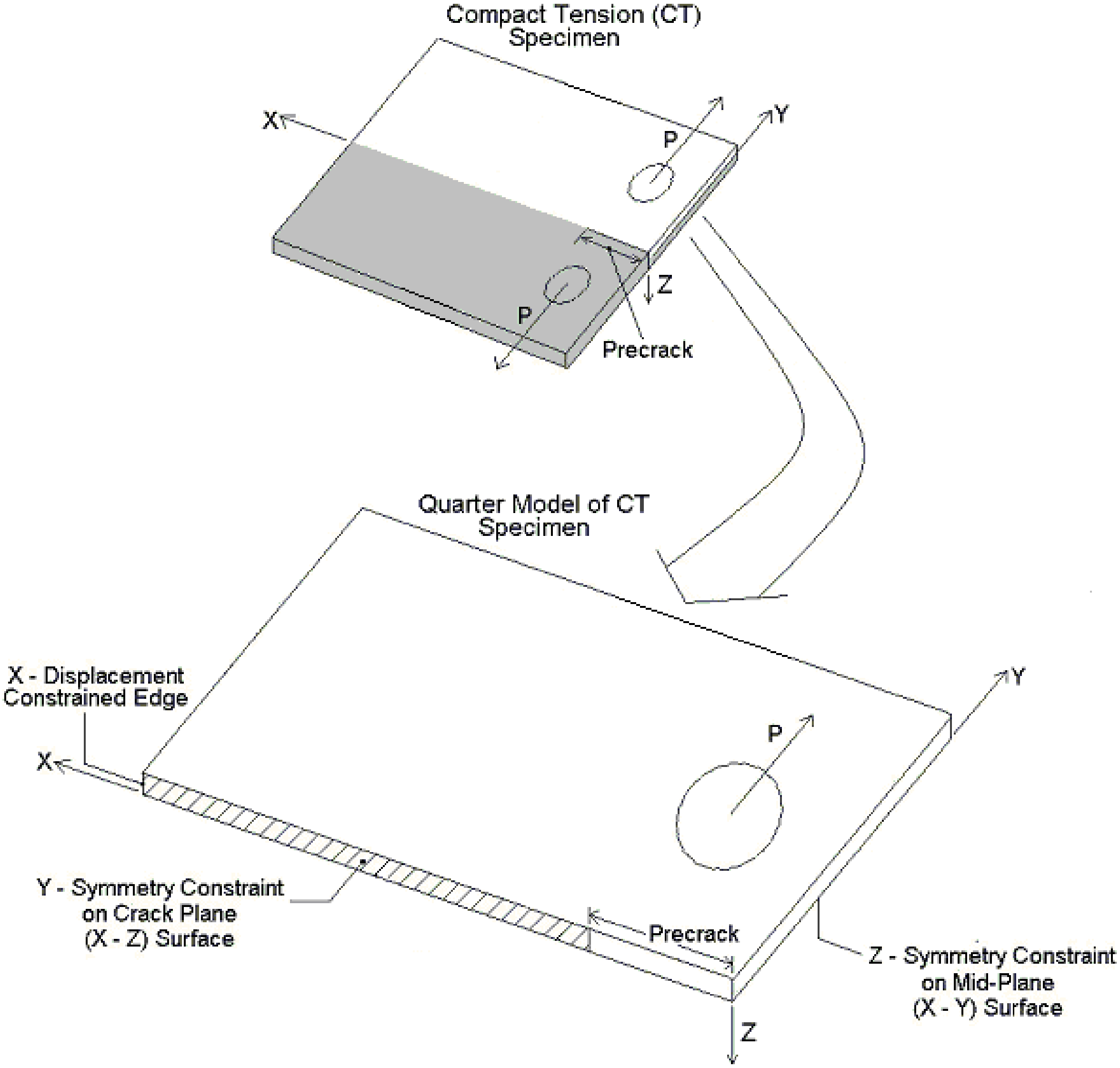

Figure 3.2 Quarter-Symmetry Model of Unreinforced Specimen, Boundary Conditions, and Displacement Application

elements to that node were modelled as linear-elastic, as previously mentioned. This scheme permits tensile stresses to develop along the bottom surface of the pin elements. In an actual experiment, only the upper half of the loading pin actually contacts and transfers load into the remaining structure, while the bottom half is not connected and is actually traction free.

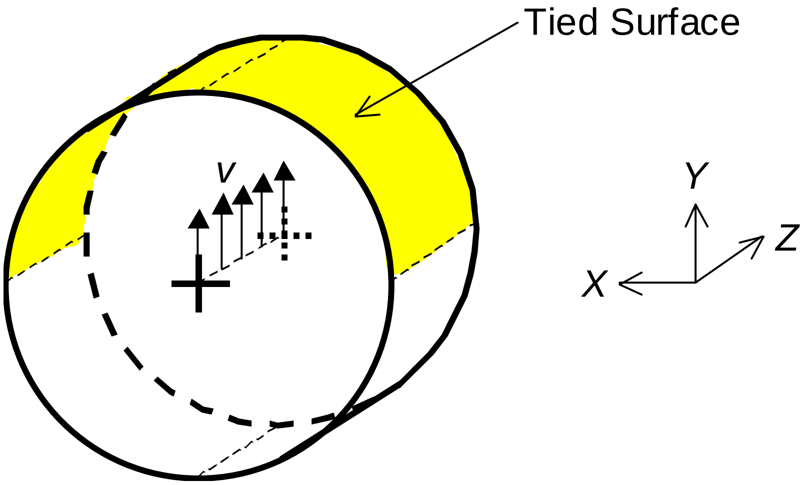

Figure 3.3 Steel Pin and Tied Surface

The unreinforced compact specimen dimensions, materials, and symmetry and boundary conditions have now been discussed. Further details of the finite-element package used, element type, and mesh are given in the next section.

3.2 Finite Element Modelling of Unreinforced Compact Tension Geometry

In order to properly explain the methods used in analyzing the problem, the capabilities, elements used, and other tools used in ABAQUS are detailed in this section. Overviews of the modelling and analysis packages are given here as well. Following the details concerning nonlinearities, a description of the element types chosen and mesh are given.

3.2.1 ABAQUS Modelling and Analysis Packages

ABAQUS/CAE is used to create the model geometries, initial loads, meshes, element types, and to review analysis results. This module provides a way in which to visually create and model complex geometries. A number of the functions used in the analysis package are also included in ABAQUS/CAE. Once the models are setup within ABAQUS/CAE, the input file is created by the software. Crack propagation is then automated using a user-written code that is discussed later.

The crack propagation problem is considered quasi-static. This means that crack propagation and displacement application can be modelled by a number of static steps, as mentioned in Chapter 2. ABAQUS/Standard was used to actually execute each analysis step. This analysis package is the preferred method in which to execute static and quasi-static problems in ABAQUS, since this is considered a relatively “low-speed” analysis with negligible inertial effects.

3.2.2 Nonlinearities

As mentioned, aluminum of 7075 alloy is modelled as an elastic-perfectly plastic material. In ABAQUS, this material nonlinearity is accounted for just by defining the yield stress and elastic modulus of the material.

In problems involving relatively small strains and displacements, the nonlinear terms within the strain-displacement relations are neglected. This class of problems is considered geometrically linear. However, in the problem considered here, large displacements due to large-scale plasticity may cause the nonlinear terms to become too large to be neglected. Therefore, a geometric nonlinear analysis, which includes the nonlinear strain-displacement terms, may be necessary, and is included.

3.2.3 Finite Element Mesh

Once the analysis package and nonlinearity considerations have been defined, elements must be chosen for each region of the compact tension geometry. Farley et al. [12] used two-dimensional quadratic triangles. Since the analysis used in the current research is three-dimensional, only three-dimensional elements are discussed.

ABAQUS/Standard offers a large choice of three-dimensional element types, including different types of tetrahedral, wedge, and hexahedral (brick) elements, as well as linear and quadratic displacement variations of each. For linear brick elements, different sub-types exist as well: full-integration, reduced-integration, and incompatible mode elements. Several element types are not considered for various reasons.

Tetrahedral elements are not considered appropriate, due to their overly stiff response, creating a "volumetric locking" effect, as mentioned in Cook et al. [39]. Wedge elements are also not considered for the same reason.

Although quadratic elements more accurately predict displacement fields around discontinuities, they are also not considered, since using quadratic elements causes irregular crack profiles. The reason for this is similar to the irregular profiles seen by Gullerud et al. [35]. When a single quadratic element is released to simulate crack propagation, both the crack tip node and the midside node constraints are released simultaneously. Since the plastic strain at the crack tip node is slightly larger than at the midside node, the element becomes distorted. Although this may be sufficient for two-dimensional models where crack tunnelling is not possible, or even stationary three-dimensional cracks, in three-dimensional models involving tunnelling and crack propagation, the through-thickness shape of the crack profiles may be influenced by the alternating amounts of plastic strain within each element. Quadratic elements are also not used due to the large increase in degrees of freedom. Computer execution time would be increased dramatically. A single analysis using all quadratic brick elements increased the time per step by more than an order of magnitude. Although remeshing and repartitioning of the structure could be done to accommodate quadratic elements, using smaller, linear elements around regions of interest would still have comparable accuracy.

Due to these limitations, the majority of the structure is modelled using linear hexahedral elements. This is the suggested element type to use from Dawicke et al. [36] and is used in most three-dimensional crack propagation finite element studies [33, 35, 37]. Linear elements would not cause the same irregular profile problem of the quadratic elements, since they have no midside nodes. Therefore, releasing a nodal constraint does not cause any change in shape within the element.

Special element consideration must be given to elements at and around the crack propagation path. Displacement accuracy is essential in this main region of interest. Unfortunately, linear 8-node brick elements fail to capture bending, and are susceptible to "shear locking" [39]. To better understand this idea of shear locking, consider a three-dimensional brick of material undergoing a prescribed bending deformation in the X-Y plane.

For a three-dimensional finite element brick, the edges parallel to the X-axis remain parallel, and instead the top edges shorten, and the bottom edges elongate to achieve the prescribed bending displacement, as shown in Figure 3.4a). This causes a fictitious shear strain in the element. This parasitic strain absorbs strain energy, and thus the reactionary moment is actually larger for linear brick elements. This phenomenon is mainly due to the linear element's inability to capture quadratic variations of the displacement with respect to the local element ξ, η, and ζ coordinates. Although the overall structure is not considered to be under a bending-type deformation, around the crack tip the elements do undergo local bending. From preliminary models, using linear bricks created extremely irregular crack profiles.

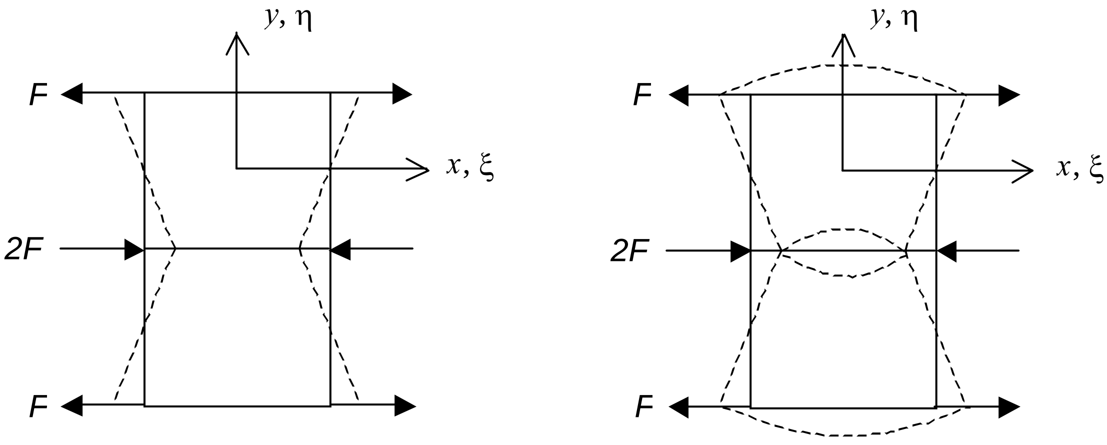

a) Linear Element **b) Incompatible Mode Element**

Figure 3.4 Figure of Linear Element and Incompatible Mode Element in Bending [39]

Incompatible mode brick elements (C3D8I), shown in Figure 3.4b), are used to remedy the irregular crack profile problem. For these elements, quadratic terms in purely ξ, η, and ζ are included in the element's displacement function. Since only quadratic variations of the displacements with respect to the coordinate variables are involved, incompatible mode elements still use fewer shape functions than a quadratic element, thus a shorter computation time. Also, since there are still only eight nodes, they are completely mesh-compatible with other linear brick elements. Incompatible mode elements perform best when the aspect ratio is close to 1:1:1, which coincidentally agrees with the findings of Gullerud et al. [35] concerning the crack surface element aspect ratios for a tunnelled crack front. Gullerud et al. [35] also experienced this "shear locking" problem, and alterations to the element formulations were made. Incompatible mode elements have also been used for crack propagation studies from Kapania et al. [40].

To put these incompatible mode elements into perspective, consider a single displacement direction, u. A regular 8-node brick involves four different shape functions, all in terms: a constant term; three linear terms of ξ, η, and ζ; three cross-terms of $\xi\eta$, $\eta\zeta$, and $\xi\zeta$; and a trilinear term of $\xi\eta\zeta$. This results in eight independent constants to describe the displacement field. For a fully quadratic element, eight shape functions are involved: the linear, cross, and trilinear terms mentioned above; along with three purely quadratic terms of ξ^2, η^2, and ζ^2; six quadratic-cross terms; and three quartic terms. This results in 20 independent unknown constants. On the other hand, an incompatible mode element involves the eight shape functions described for the linear 8-node brick, with only three added purely quadratic terms of ξ^2, η^2, and ζ^2. This results in only 11 independent constants. As is shown later, these elements predict displacement response fairly well for this problem.

The steel displacement pin and a region around it are modelled with wedge elements (C3D6) in order to capture the pin curvature. Although wedge elements are also prone to the aforementioned “volumetric locking” phenomenon, the steel pin is considerably stiffer than the base aluminium so large bending is not an issue.

In the remaining “far-field” areas of the compact tension model, reduced-integration, linear brick elements (C3D8R) are used. These are computationally inexpensive brick elements due to the use of a single integration point calculation, yet still fairly accurate. Where this “far-field” area lies is discussed next.

Incompatible mode elements are used along the crack plane, for the reasons previously mentioned, as well as some distance away from the crack plane. This is done in order to more accurately capture out-of-plane Poisson contractions around the crack tip within the plastic zone. These Poisson effects affect local displacements and may influence tunnelling. The plastic zone region can extend anywhere from one to two plate thicknesses in the Y-direction from the crack plane, depending on magnitude of the applied force, according to the results from Nakamura and Parks [31]. Using Equation 2.1 on the data from Farley et al. [12] for a plane-stress plastic zone size estimation, the main area of interest lies approximately 0.15 inches in the Y-direction from the crack plane. Therefore, the mesh of

C3D8I elements is small and uniform up to this point. The size of these elements is 0.01 inches (about 250 microns) in each of the three directions. This is the same *X*-direction element size used by Dawicke et al. [16]. At any *Y*-coordinate greater than 0.15 inches (i.e., “far-field”), the element size in the *Y*-direction gradually increases to 0.08 inches, and consists of C3D8R elements.

This element size of 0.01 inches was deemed sufficient, as the baseline validation analyses show, and any smaller element size would also incur a large penalty in computation time. An analysis was conducted where the number of elements was doubled through the thickness, which also required the number of elements along the crack propagation direction to double, and also an increased number of elements in the *Y*-direction, in order to maintain the 1:1:1 element aspect ratio. The same number of steps was required to go approximately half the distance. Added onto this time, each step also required a longer computing time, due to the increased number of elements in all three directions. The overall results were similar, and the difference in maximum load computed was approximately 1 percent.

As previously mentioned, wedge elements are only used for the steel loading pin and close to the loading pin hole. The typical element size of these wedge elements is also approximately 0.08 inches. From subsequent remeshing, it was found that further refined meshing of the loading pin and around the loading pin hole had little effect on the overall response, therefore the mesh refinement in this area is deemed sufficient.

A typical finite element mesh of the unreinforced case is shown in Figure 3.5. As discussed, two different types of three-dimensional elements are used for this analysis: wedge and brick elements. Of the brick elements, two linear sub-types are used: incompatible mode elements (C3D8I) and reduced integration elements (C3D8R). The wedge elements used are full integration linear wedges (C3D6). Figure 3.5 shows the location of each element type within the compact tension geometry. As Figure 3.5 shows, the mesh is much more refined around the crack propagation area. From the initial crack tip, the C3D8I elements extend 1.10 inches along the *X*-direction.

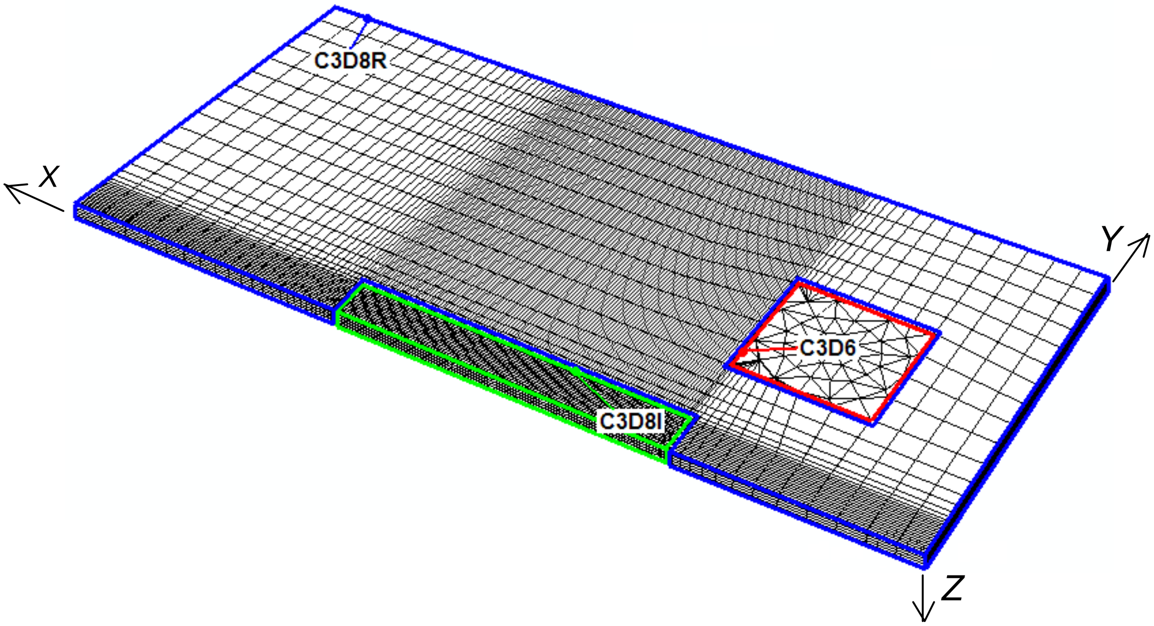

Figure 3.5 Finite Element Mesh of Unreinforced Compact Tension Specimen with Element Types Highlighted

Details on the material models and element types used for the unreinforced compact tension geometry have now been considered and chosen. These important choices have been made based on the previous work of others, time and computation considerations, as well as trial and error. Details on the CTOA-based crack propagation procedure are explained in the next section.

3.3 CTOA-Based Crack Propagation Approach

The approach for using a CTOA-based crack propagation criterion is described in this section. It includes the calibration procedure to define the variation of critical CTOA as a function of crack length. Also, the crack propagation procedure and its implementation in ABAQUS are presented.

3.3.1 Application of Previous Research

The approach used in this research is a modification to the straight crack front approach from Gullerud et al. [35], which was based on a three-dimensional model. However, before making any changes to the straight crack front procedure, some of the ideas on incrementing crack growth and allowing for crack tunnelling are tested and the load, P, as a function of surface crack length, Δa, relations compared to the procedure from Gullerud et al. [35]. The three-dimensional model of the unreinforced 7075 aluminum compact tension specimen geometry was used.

The procedure from Gullerud et al. [35] was first applied to this three-dimensional model. To summarize this procedure again, a straight crack front is assumed, the CTOA is measured at the midplane, and the crack growth increments are equal to the measurement distance L_c = 0.04 inches, as shown in Figure 2.10. Although Figure 2.10 does show only two nodal rows released, Gullerud et al. [35] did show that response is fairly insensitive for any element lengths smaller than the measurement distance, L_c. Therefore, with the mesh described in the previous section, for each time critical CTOA is reached, four rows of nodes are released to simulate crack growth. The overall shape of the force versus surface crack growth relation was similar to the two-dimensional analysis from Farley et al. [12], with a maximum load within 1.5 percent. However, the maximum load occurred at a surface crack length of approximately 0.2 inches, while the maximum load of the analysis and experiment from Farley et al. [12] occurred at a surface crack length of approximately 0.1 inches. This difference represents one specimen thickness, an amount consistent with the previous research mentioned in the literature review.

In an effort to overcome the surface crack growth length prediction problem and to help account for tunnelling, the first variant to the procedure from Gullerud et al. [35] was to release only a single row of nodes, rather than four. This allowed for a more accurate representation of crack growth in that the crack growth increments were not limited by $\Delta a = L_c$, as assumed from Gullerud et al. [35]. This type of analysis, used by Dawicke et al. [16], still assumes a straight crack front, with the CTOA being measured at the midplane only. Changing the scheme to incorporate single nodal release would also be important when considering tunnelling effects. A depiction of this technique was shown in Figure 2.8. Despite this refinement, there was negligible difference between this single element row removal analysis and the multiple element row removal analysis from Gullerud et al. [35]. The maximum load was still adequately close to the analysis from Farley et al. [12], but the crack length at maximum load was still greater by a plate thickness.

To continue to overcome the crack growth length prediction problem and also allow for tunnelling in an approximate sense, another procedure mentioned by Dawicke et al. [36] was employed. This procedure uses a single nodal constraint release, but approximates tunnelling by computing and monitoring the CTOA at individual crack profiles through the thickness and by allowing the crack front to propagate when one of the calculated CTOAs reaches the critical value. This procedure is shown in Figure 2.11. The effect of this modification was again negligible.

Since there was no difference in response among these three schemes for crack propagation, and since the surface crack length at maximum load was still over predicted by the model, a procedure to account for the variation of the critical CTOA with crack length, particularly just as the crack begins to propagate, was implemented. The procedure includes initial critical CTOA variation at the specimen midplane obtained from the straight crack front model. Independent nodal release at the crack front along each crack profile was also included. This procedure is described next.

3.3.2 Determining the Critical CTOA as a Function of Crack Length

As mentioned in the literature review, there is evidence that the critical CTOA varies as the crack begins to grow and then assumes a constant value for longer crack growth lengths. Although the presence of an initial region where the critical CTOA changes with crack growth length would not be that important for larger total crack propagation distances, in this analysis, this initial region is almost one-third of the total propagation distance. Because of this, a region within which the critical CTOA varies will be taken into account here. To that end, critical CTOA as a function of crack length data from a 2000-series aluminum for this distance from Dawicke's straight crack front analysis [16] was fit to a quadratic function. The quadratic variation was assumed to be true for the 7075 aluminum compact tension configuration studied here. The quadratic function for this material is assumed to be valid for every profile crack length through the thickness, Δa_i, where the index i corresponds to a through-thickness crack profile. With the straight crack front model being used, it was assumed that the only crack length of consequence was the midplane crack length, Δa_m. The midplane critical CTOA was assumed to have the following form:

$$\Psi_c(\Delta a_m) = b_2(\Delta a_m)^2 + b_1(\Delta a_m) + b_0 \qquad \text{for } \Delta a_m < B$$

$$\Psi_c(\Delta a_m) = \text{constant} \qquad \text{for } \Delta a_m \geq B \qquad \text{(Eqs. 3.1)}$$

where, recall, B is the specimen thickness and Δa_m is the crack growth at the midplane. In order to calculate the coefficients, b_n (where n = 0, 1, 2) and the constant value of the critical CTOA at crack lengths larger than B, the following procedure is used:

1) A displacement is applied to the model at the loading pin in order to achieve a pin reaction load equal to that obtained from the load versus crack length results from Farley et al. [12] for $\Delta a_m = 0$.
2) The nodal CTOA is measured at the midplane of the specimen, at the distance L_c from the crack tip, as depicted in Figure 3.6. This is done by measuring the CTOD at a distance L_c from the crack front, and the CTOA is computed from CTOD, δ_{CTOD}, from Equation 2.10.

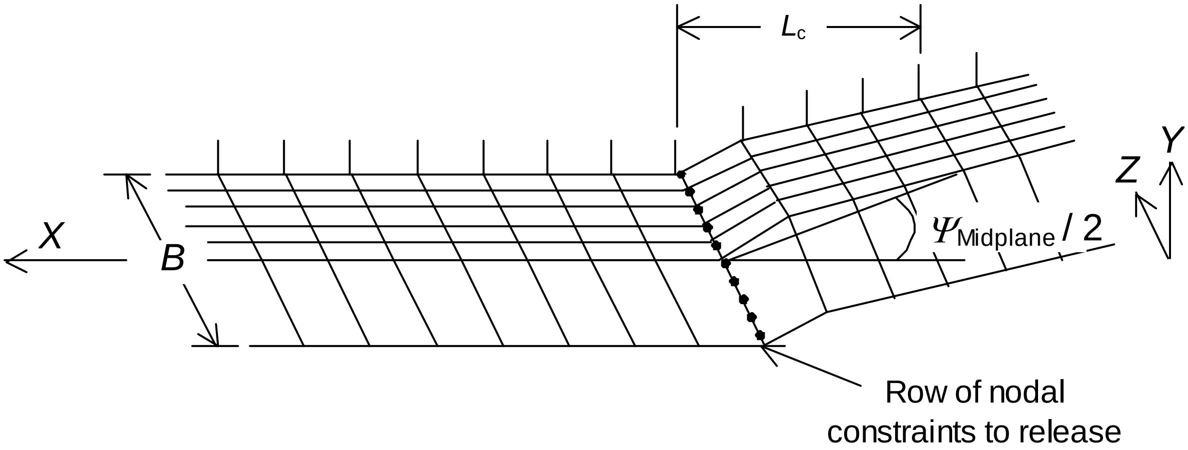

Figure 3.6 Straight Crack Front, Initial Blunting, CTOA Measurement, and Nodal Constraints

3) Nodal constraints are released along the next row of elements to simulate crack propagation, as shown in Figure 3.6.

4) The load at the next increment of crack length from Farley et al. [12] is achieved by applying a larger pin displacement.

5) Steps 2) through 4) are repeated for subsequent applied loads and surface crack lengths. The CTOA measurement for longer surface crack lengths is shown in Figure 3.7.

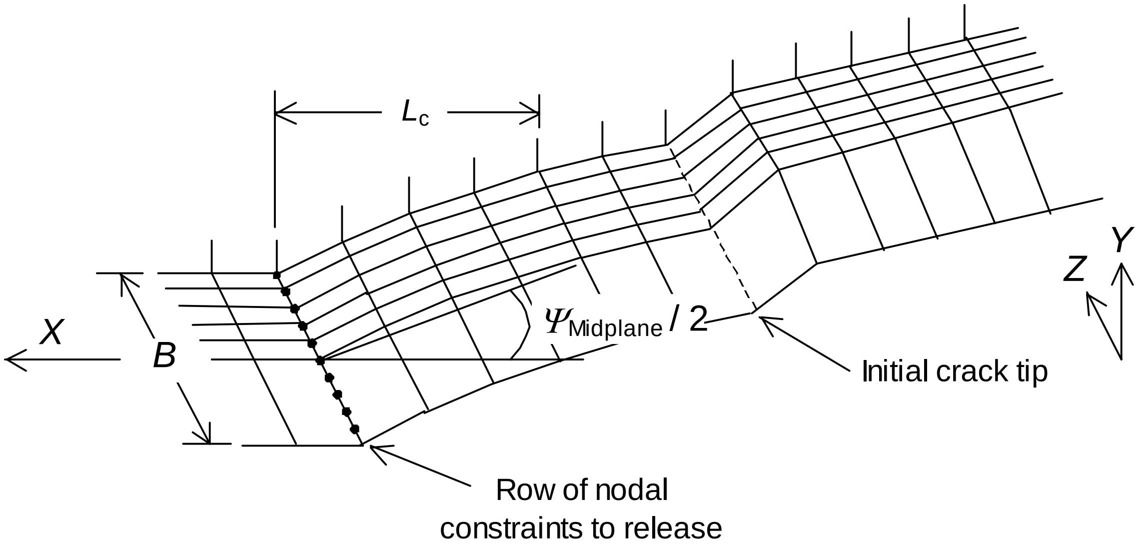

Figure 3.7 Straight Crack Front, Longer Crack Lengths, Blunted Tip, and CTOA Measurement

Two important values are obtained from this calibration: the initial critical value of CTOA, and the constant critical value of CTOA after the initial crack growth. Using the previously mentioned quadratic variation, the conditions that: 1) the quadratic function is equal to the initial critical CTOA at $\Delta a_m = 0$, 2) the function is equal to the constant critical value for $\Delta a_m = B$, and 3) the slope of the function at $\Delta a_m = B$ is equal to zero. With these conditions, all the coefficients of the quadratic variation given by Equation 3.1 can be solved for, the constant value of the critical CTOA in Equation 3.1 is automatically known, and the critical CTOA as a function of Δa_m is known.

3.3.3 Crack Propagation

The following describes the procedure used to model three-dimensional crack growth using the CTOA criterion, while also accounting for crack tunnelling. In order to accommodate crack tunnelling, Equation 3.1 is assumed to be valid for the crack growth increment, Δa_i (i = 1, N), at each of the i profiles through the thickness, where N is the number of through-thickness crack profiles in the finite element model, and i is the crack profile number, where $i = 1$ is the profile at the midplane and $i = N$ is the profile closest to the surface. The steps in this procedure are:

1) The critical CTOA as a function of crack length, $\Psi_c(\Delta a_i)$, is assumed known, as just described.
2) A displacement is applied at the center of the loading pin to open the crack and the analysis iterates to an equilibrium state. The applied displacement is adjusted so that the calculated CTOA at the midplane crack profile equals the critical CTOA. To do this, CTOD is measured 0.04 inches from the crack front, and CTOA is computed from CTOD, δ_{CTOD}, from Equation 2.10.
3) When the calculated CTOA at the midplane crack tip exceeds the critical CTOA, the applied displacement at the pin is held constant, and the constraint at the midplane crack tip is removed.
4) While the crack profile length is less than the measurement point of L_c = 0.04 inches, nodes at the initial crack tip are used to provide the CTOA for each through-thickness crack profile. This calculation for CTOA uses a modified version of Equation 2.10, namely:

$$\Psi = \tan^{-1}\left(\frac{\delta_{\mathrm{OCTL}}}{\Delta a_{\mathrm{i}}}\right) \qquad \text{(Eq. 3.2)}$$

   where δ_{OCTL} is the calculated CTOD at the original crack tip location. A depiction of this is given in Figure 3.8.

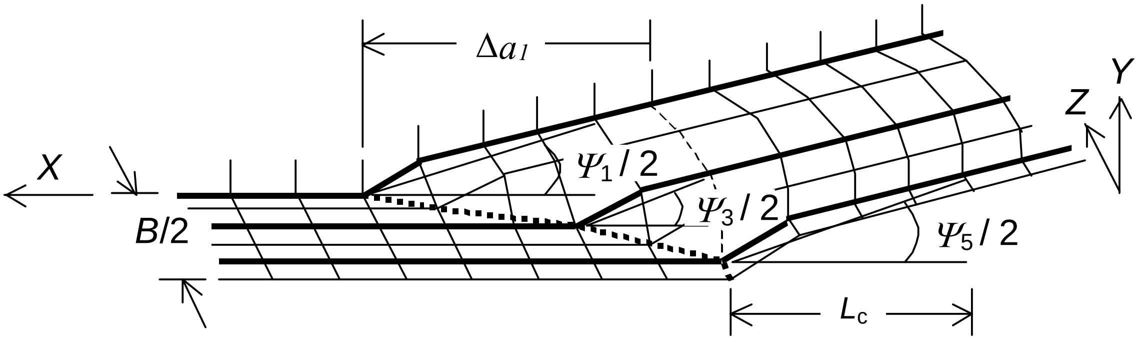

Figure 3.8 Various Crack Profiles, Δa_i, and CTOA Measurements for Tunnelled Crack Front

5) While the measured CTOA exceeds the critical CTOA for a particular crack profile, i, where $\Delta a_i > 0$, the applied displacement at the pin is held constant, and the next nodal symmetry constraint at that profile crack tip is removed.
6) Excluding the initial loading step, for the following N consecutive steps, the nodal constraint at profile i-1 is removed at step number i. This will be subsequently described in detail.
7) After all nodal constraints are removed, the solution algorithm is allowed to iterate to an equilibrium state with no further application of applied displacement at the pin, thus simulating crack growth.
8) At this new equilibrium state, CTOA measurements along the crack front are performed. If any other computed CTOA along the crack front exceeds its corresponding critical values, or if step N has not been reached, then return to step 4). If the user-defined total crack length has been reached (or, for reinforced geometries, if the reinforcement has failed) then stop the analysis. Otherwise, go on to step 9).
9) Once all measured CTOA values are less than their corresponding critical CTOA values, an additional displacement is applied to the pin and equilibrium is again reached. Displacements are added until another critical CTOA situation is reached at the crack front.
10) If reinforcement is included and the reinforcement has failed, stop the analysis, otherwise return to step 4).

Expanding on Step 6): Because crack tunnelling at the midplane of the specimen will occur over a very short initial surface crack length, i.e., the crack length at profile *N*, once the model is created and the initial pin displacement is applied, an initial constraint release procedure must be adopted to release the first row of nodal constraints on the elements along the initially straight crack front. In an attempt to more accurately initiate this phenomenon, the nodal constraints are removed consecutively from step to step from the midplane to the surface.

It should be noted that profile *N* is the profile *closest* to the surface. This profile does not actually lie at the surface, due to the nature of the initial model setups. Constraint removal for $i = 1$ to N-1 consists of a single node. Profile *N* lies one element length in from the outer surface in the Z-direction, as shown in Figure 3.8, where the CTOA measurement, Ψ_5, is measured at profile *N*. Once the critical CTOA at profile *N* is reached, both the nodal constraint at profile *N* and the nodal constraint at the surface are removed in the same step. Even though this may not be exact, the measured CTOA at profile *N* was still within 1.5 percent of the CTOA at the surface, the use of smaller elements still gave similar load vs. surface crack length curves, and the overall load vs. crack length curves compared well with previous work as will be shown later.

Although a general procedure for crack propagation is given at this point, further details had to be accounted for. These are described in the next section.

3.3.4 Important Considerations and Compensations

Displacement Convergence Scheme

An applied displacement convergence scheme is used to help minimize the number of required consecutive displacement steps to reach the critical CTOA at each profile. The convergence scheme uses the difference between the largest measured CTOD at $L_c = 0.04$ in. and its corresponding critical CTOD. Just using this difference to add onto the applied displacement would not be large enough. This is shown in Figure 3.9 where similar triangles

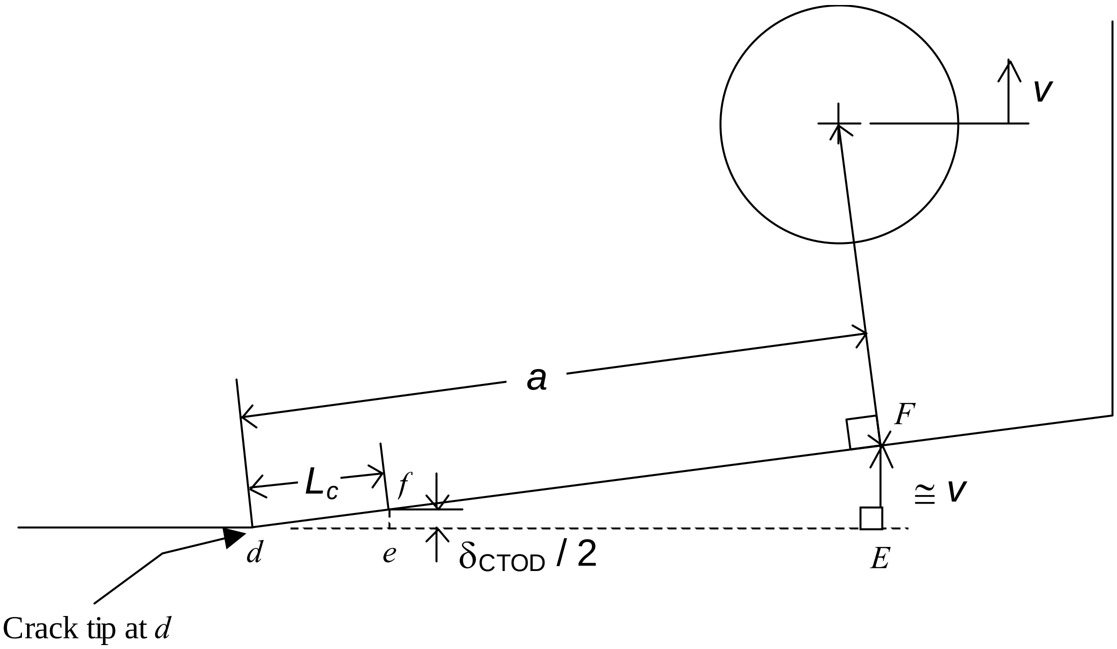

Figure 3.9 Straight Crack Profile

def and *dEF* are identified. From these triangles, the relations of Equations 3.3 are derived from Figure 3.9.

$$\frac{v}{a} = \frac{\delta_{\mathrm{CTOD}}}{2L_c}$$

$$v = \left(\frac{a}{2L_c}\right)\delta_{\mathrm{CTOD}} \qquad \text{(Eqs. 3.3)}$$

For the geometry considered here ($a = 0.235$ in., $L_c = 0.04$ in.), Equations 3.3 results in:

$$v \cong 3\delta_{\mathrm{CTOD}}$$

From this relation, the scale factor between δ_{CTOD} and the applied displacement, v, used to guide convergence is approximately three. However, this is not exactly the case. The profile is slightly curved close to the crack tip. Therefore, the difference between the largest measured CTOD and its corresponding critical CTOD is multiplied by a more conservative convergence factor of 1.5. The only crucial detail of this convergence scheme is to minimize the number of consecutive steps to reach a critical CTOA situation (i.e., minimize computation time), but also to make sure that the critical CTOA is not "overshot" by more than a few percent.

An unreinforced compact tension specimen analysis was analyzed using the above-mentioned displacement convergence scheme. The results from the analysis showed that after one displacement step, the computed critical CTOAs were greater than the target values, but well within 1 percent. In some cases, the amount of calculated pin displacement to add was on the order of 10^{-11} inches, below the displacement tolerances set in ABAQUS. Therefore, although the calculated CTOA was close enough to the critical values, the structure remained “motionless” due to the negligible amount of added displacement. This was considered accurate enough for this investigation. Although the analysis did require a relatively large number of consecutive displacement steps (approximately 30 steps in some cases) to reach a critical CTOA, this is only of secondary importance to the accuracy. For comparison, only a single step is required to release a nodal constraint (i.e., grow the crack). The only time that the calculated CTOA exceeded the critical value by more than one percent was in consecutive removal steps, which is an undesirable situation. This causes excessive element deformation, thus excessive element plasticity at the crack front. Steps to correct this problem will be discussed in more detail next.

Excessive Element Deformation

Due to the nature of the crack propagation criteria, accurate prediction of the crack profile shape is crucial. Any unintentional excessive element deformation can cause excessive local plastic strain at a node, and thus affect adjacent elements, as well as lead to eventual inaccurately calculated CTOD values. Excessive element deformation worsens when this single node of unaccounted large plastic strain coincides with a measurement point. At that step, the applied displacement is thus increased until the node at the measurement point reaches the critical CTOD, thus causing erroneous excessive plastic strain at the new crack tip of that profile. This creates unwanted fluctuations in the load crack vs. growth relations, as well as irregular crack profiles. Unfortunately, original crack tip deformation causes the unwanted effect in that the initial row of elements undergoes the majority of strain and displacement. This problem was also encountered by Gullerud et al. [35], as well as earlier attempts of this research. A depiction of this phenomenon is shown in Figure 3.10. As mentioned in Chapter 2, Gullerud et al. [35] circumvented this problem by removing all nodal constraints less than L_c ahead of the crack front, and therefore accepting the irregular crack profile shape in Figure 3.10. For a tunnelled model, doing this is not

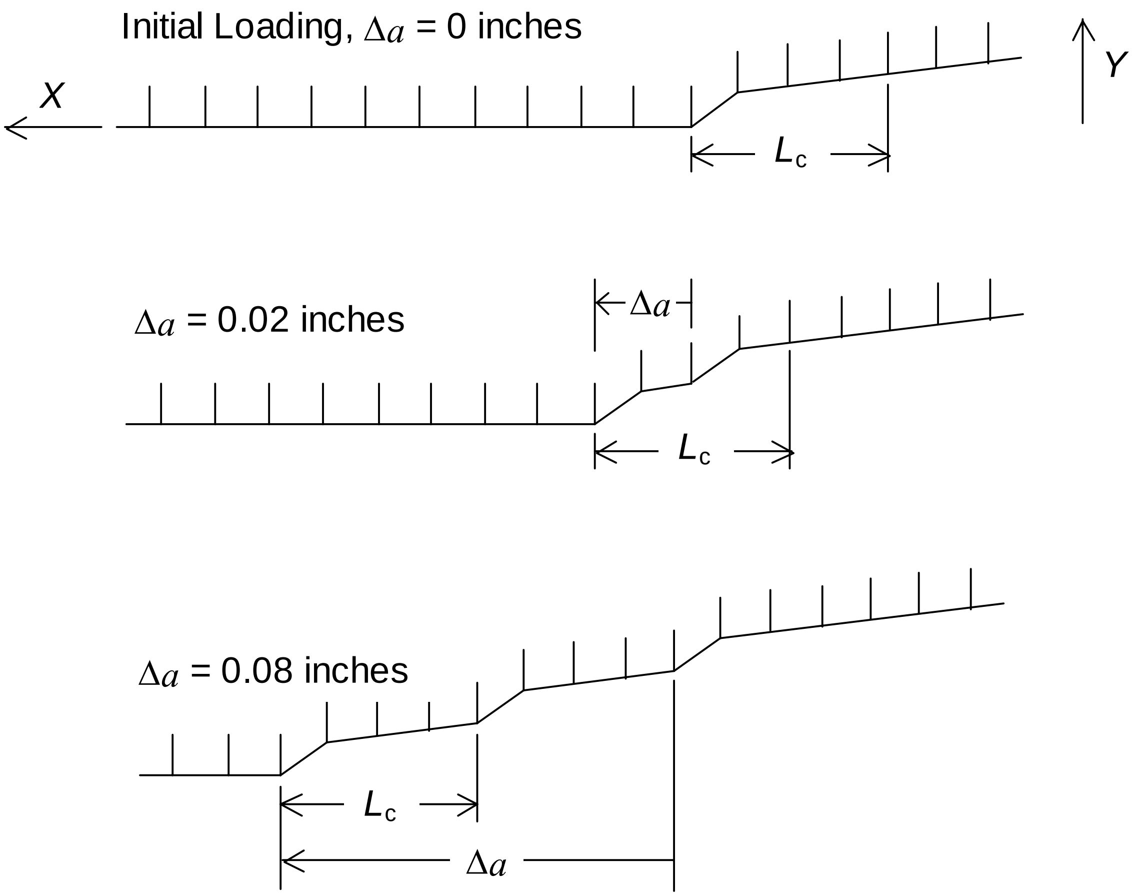

Figure 3.10 Irregular Crack Profile Due to Excessive Element Deformation Due to Plasticity

acceptable. Excessive element deformation is further aggravated by the static nature of each analysis step, specifically for consecutive constraint removals. At the end of a constraint removal step, equilibrium is reached, the applied displacement remains the same, and another node along a different profile may exceed the critical CTOD. To more clearly illustrate this, assume there is a specific step in the analysis such that a particular measured CTOD at a specific profile is close to, but has not quite exceeded, its corresponding critical CTOD. Next, assume at this same step, a CTOD along a different through-thickness crack profile exceeds its critical CTOD. The pin displacement is held constant, but the subsequent release of this constraint causes a redistribution of load, which leads to increased displacements elsewhere. The problem of increased calculated displacements is especially pronounced when the nodes on the outer surface element are released. These relatively larger displacements occur because during tunnelling there are no constrained interior material elements to support the load, thus the finite elements at the surface carry a relatively large portion of it. The resulting calculated CTOD that was close to reaching critical at the beginning of the step may exceed the critical CTOD by some large margin at the end of the step. Thus, this excessively deformed element contributes to larger applied loads, as mentioned above, when this overly-strained node coincides with a measurement point. A depiction of this problem is shown in Figure 3.11. These excessively deformed elements also effect tunnelling, since these elements would resist element deformation through the thickness as well.

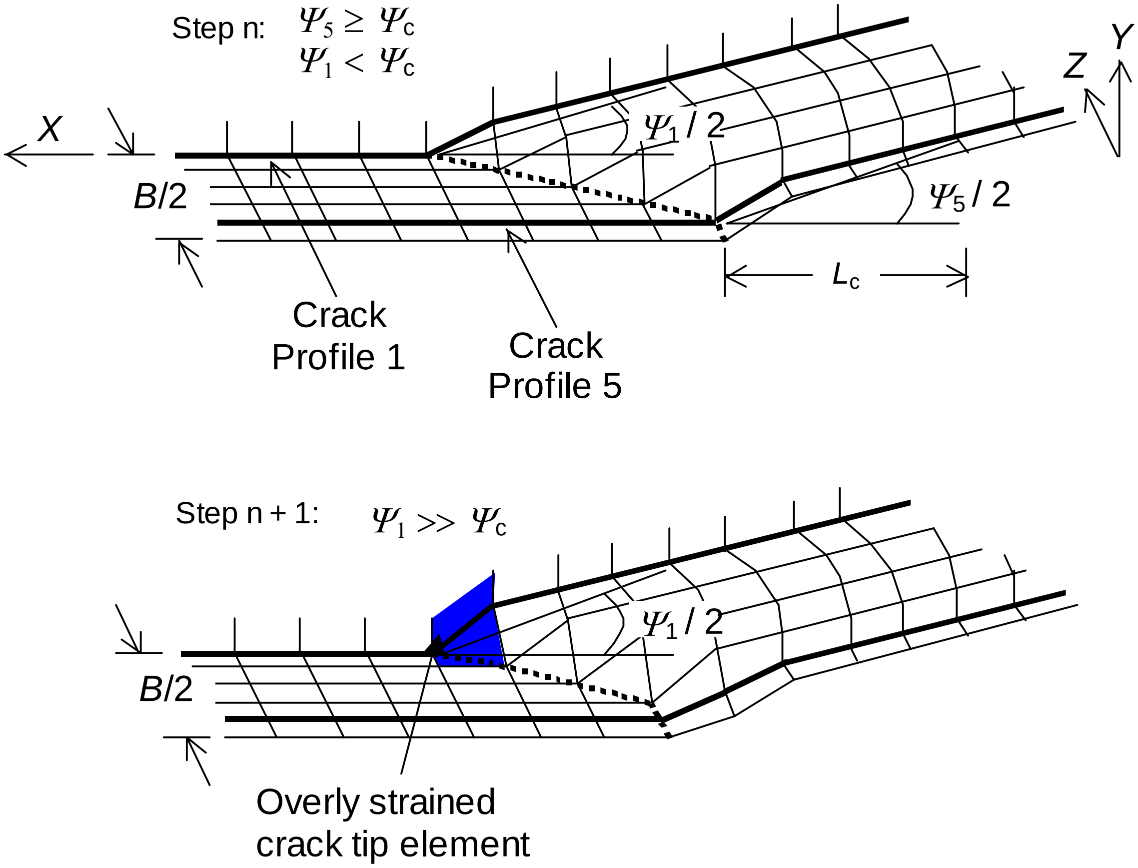

Figure 3.11 Overly-Strained Elements

The constraint release procedure for $\Delta a_i < L_c$ adopted from Dawicke et al. [16] helps to minimize the problem with excessive plastic deformation. But in order to further account for all of the issues previously mentioned, three methods are employed: small X-direction element size, calculated averaged CTODs, and employing a range of critical CTOD values, rather than one specific value.

A relatively small element size in the X-direction (i.e., crack propagation direction) also helps to minimize CTOD increase due to sequential constraint removal steps. With the larger elements, more material is being released from a constraint and displacements along other crack profiles increase. The measured CTOD that was almost at the critical CTOD at one node at the beginning of the step now exceeds the critical CTOD by a larger degree. Using smaller elements, less material is released from a constraint, thus helping to minimize the resulting increase in measured CTODs after a constraint removal.

A CTOD averaging technique was used to further smooth the crack profiles. This technique uses the same weighting factors as used in a trapezoidal or rectangular integration rule. The nodal displacements on a specific profile one element distance before and one element distance after the nodal measurement point are averaged. This averaged CTOD value is then averaged with the nodal displacement at the measurement point. Linearity of the crack profile is assumed, but only over a very short distance. Figure 3.12 shows the difference in predicted crack profiles between an analysis without averaging, and an analysis with averaging. As shown in Figure 3.12a), despite adopting the procedure from Dawicke et al. [16], some periodicity in the crack profiles is still seen every four element lengths (i.e., L_c). This is undesirable for a tunnelled model. Averaging, shown in Figure 3.12b), smoothes out the crack profiles much better.

Finally, redefining the critical value of CTOD to be any value of CTOD within a certain "range" of the critical CTOD helps lessen the problem with excessive element displacement after consecutive constraint removal steps. This range of critical CTODs encompasses other measured CTOD values that are close to their critical CTOD values. So, consider the aforementioned situation of the ith profile CTOD that is close to but less than the critical value, and another CTOD along the jth profile that has reached the critical value at the same step. The next step is a constraint removal. After constraint removal, the solution iterates to equilibrium and the CTOD at the jth profile can exceed the critical value by more than 5 percent while the node of the ith profile is not released. This excessive

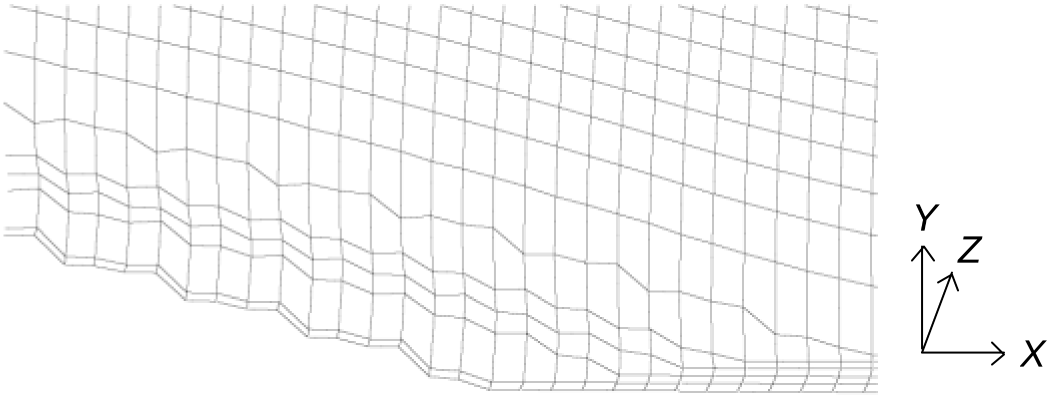

a) No Averaging

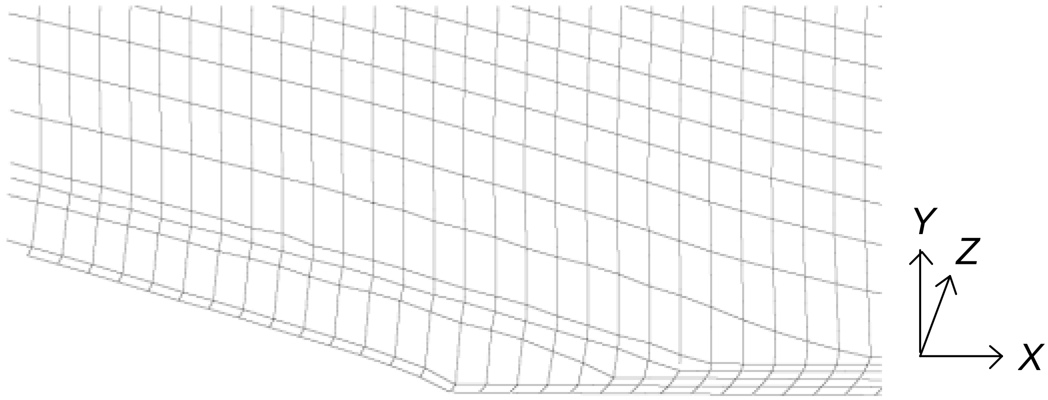

b) Averaging

Figure 3.12 Figure Showing No Averaging vs. Averaging

displacement creates the previously mentioned problem of the fluctuating response curves. However, with a range of critical CTODs, both constraints will be removed in the same step (assuming the critical CTOD range is sufficient). Allowing a range of critical CTOD of 0.000025 inches, which represents less than a 2.0 percent change in the critical CTOD, but is still sufficiently close to the actual value, helps alleviate the problem. The worst-case scenario of this situation would be the unreinforced specimen, since the use of the reinforcement will resist crack tip opening displacements. The baseline, unreinforced analysis was performed, and a maximum difference in measured and critical CTOD recorded. This maximum difference was only 4 percent over the critical CTOA. Although this difference between with and without this "range" is small, the case with averaging also "centered" the average of all CTODs within the "range" around the critical values better. As will be shown later, creating a "range" of critical CTODs does not make a large difference in overall response. The greatest advantage of including a “range” of critical CTODs is reducing the number of consecutive displacement steps from approximately thirty to five or less.

3.3.5 Implementation of CTOA-Based Crack Propagation

To summarize, ABAQUS/CAE is first used to create the model geometry and mesh, boundary conditions, and to apply an initial pin displacement. The initial displacement is adjusted to a value that creates a critical CTOA condition at the midplane crack tip profile. This initial critical CTOA is calculated from the previously mentioned quadratic CTOA function at zero crack length. This is considered the first step. The next step is a constraint removal step at the first midplane node (i = 1), thus simulating tunnelling. From there, iteration is required to remove constraints at other nodes and to simulate crack propagation.

A computer code written in the Python programming language [41], given in Appendix I, was used to automate the successive application of loading pin displacements and subsequent determination of crack propagation. Each equilibrium step consists of either of an applied displacement, or a crack propagation (i.e., constraint removal) step, as previously mentioned. Once equilibrium is established after applying the initial displacement, the Python code calculates critical CTODs from the user-defined form of the critical CTOA, i.e., the quadratic form in Equation 3.1. Then, the code reads in the calculated CTODs from the ABAQUS output, and determines whether or not the critical CTOD has been reached at another crack profile. If so, the next step is a constraint removal step. If not, an additional increment in load pin displacement step is applied to achieve crack gowth. To achieve this in ABAQUS, two different text files are pre-defined: one containing all the necessary information to remove nodal constraints, simulating crack propagation; and another containing the necessary information to apply a displacement. Depending on which of the two situations occurs, the appropriate text file is altered to reflect the change, and is then appended to the next input file for execution. A flow chart of this is shown in Figure 3.13. As the flowchart shows, additional logic is built-in to account for whether or not

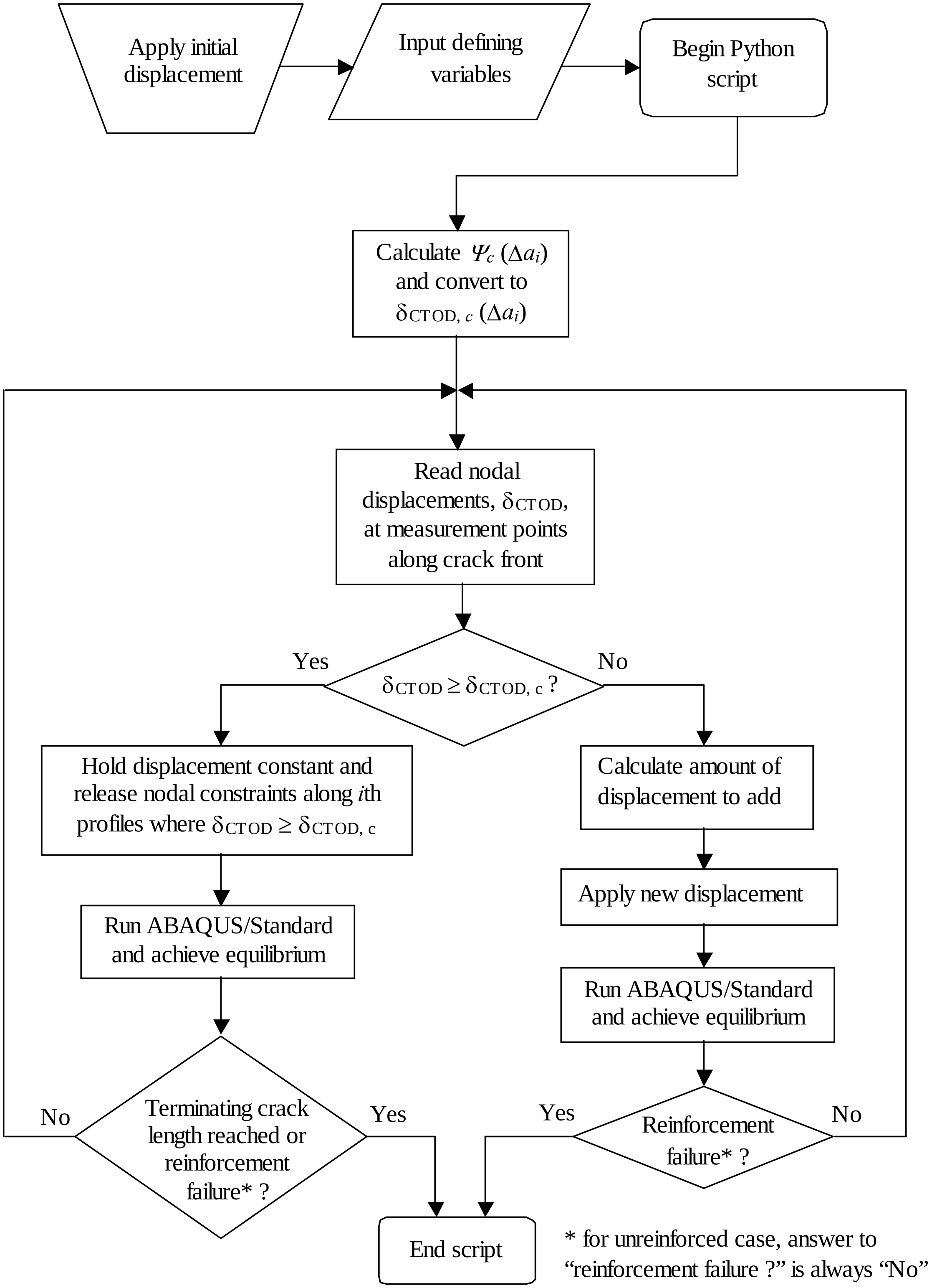

* for unreinforced case, answer to "reinforcement failure ?" is always "No"

Figure 3.13 Flowchart of Crack Propagation Procedure

reinforcement is included. Since only an unreinforced case has been discussed up to this point, the question of “reinforcement failure ?” is always “No”, according to the footnote. Once architectures with reinforcements are modelled and analyzed, the reinforcement strains are checked at the end of each step. In these cases, the question of “reinforcement failure ?” may be either “Yes” or “No”.

ABAQUS implementation of a general CTOA-based crack propagation procedure has been detailed for an unreinforced compact tension specimen. Before discussing certain model reconsiderations for the reinforced cases, the validation of the unreinforced model and the crack propagation procedure are next.

3.3.6 Validation

The ABAQUS three-dimensional finite element analysis and user-written routines were used to analyze the unreinforced compact tension specimen studied by Farley et al. [12]. Comparisons were made with the results of Farley et al. [12] to validate the three-dimensional analysis to the degree a three-dimensional analysis can be compared with a two-dimensional analysis. Farley et al. [12] mainly focused on the initial 0.335 inches of surface crack length for all cases. This is the distance from the crack tip developed by fatiguing the specimen to the leading edge of the reinforcement. However, the work of Farley et al. [12] also included an unreinforced case that had a much larger crack length. The finite element mesh of Figure 3.5 was used, and the maximum crack length extended to 1.10 inches in order to compare to the experimental and analytical results from Farley et al. [12].

Using the procedure for calculating the initial variation of the critical CTOA in Section 3.3.2, the coefficients of Equation 3.1 are known and calculated. The following equations are the forms of the critical CTOA that are used from this point on:

$$\Psi_c(\Delta a_i) = (100(\Delta a_i)^2 - 20(\Delta a_i) + 5.7) \text{ degrees} \qquad \text{for } \Delta a_i < B$$

$$\text{(Eqs. 3.4)}$$

$$\Psi_c(\Delta a_i) = 4.7 \text{ degrees} \qquad \text{for } \Delta a_i \geq B$$

where Δa_i and B are in inches. The constant value of the critical CTOA seems to be fairly consistent with that of other aluminium alloys. From previous literature [12, 16, 17, 36 - 38], for most 2000-series aluminium alloys, the constant critical CTOA is around 5 degrees at a similar distance L_c.

Load as a function of surface crack length relations are shown in Figure 3.14. Five relations are shown in this figure: two from Farley et al. [12] and three using the developed three-dimensional ABAQUS analysis. Of the two relations from Farley et al. [12], one is from the experiment and the other is from the numerical two-dimensional analysis based on the FRANC2D code. Of the three three-dimensional ABAQUS relations, three different crack propagation procedures were used: one does not utilize the "ranged" critical CTOD, one does not use CTOD averaging, and one uses both of these procedures. As shown in the

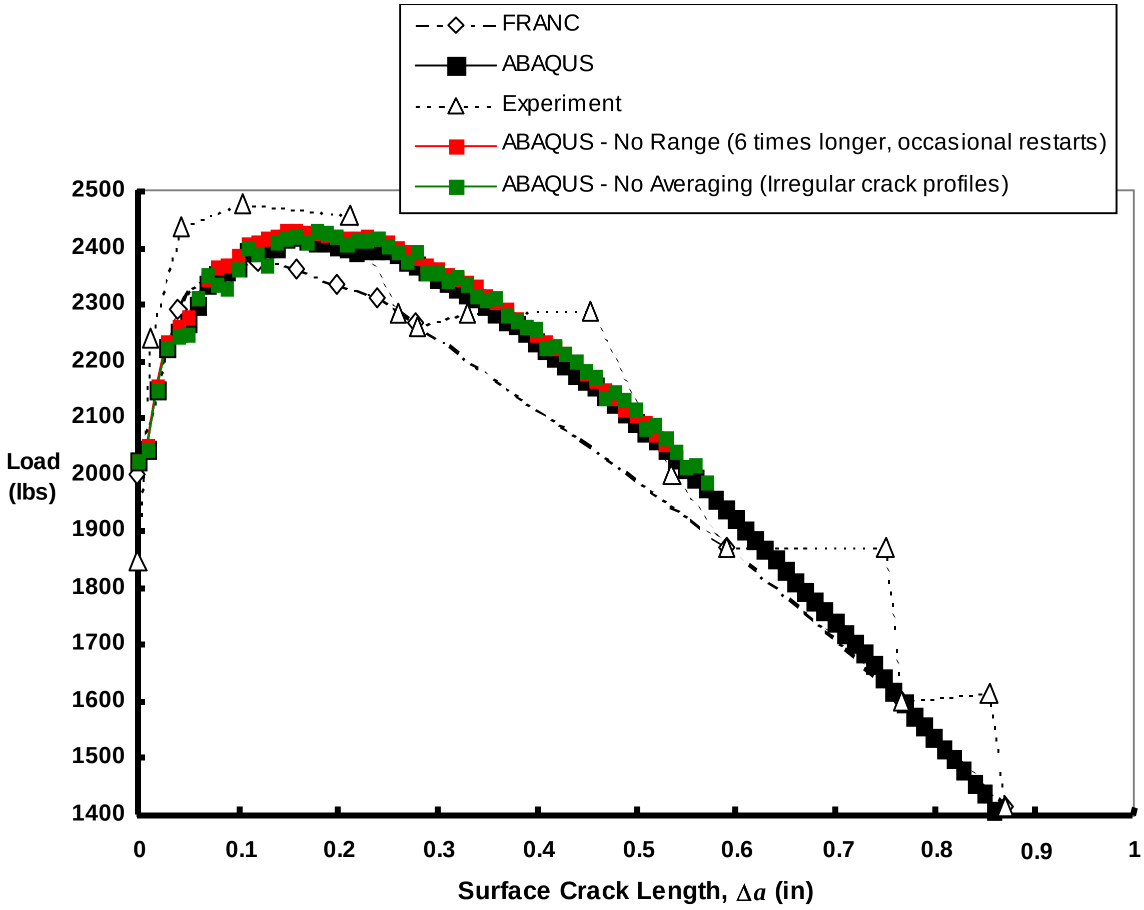

Figure 3.14 Load vs. Surface Crack Length Relations: Unreinforced Geometry with Different Crack Propagation Schemes

figure, there is little difference among the three three-dimensional ABAQUS analysis relations. However, without using a “ranged” critical CTOD, the runtime is approximately six times longer than with using a “ranged” critical CTOD. The drawback of not using CTOD averaging is the irregular crack profiles, previously shown in Figure 3.12. Not using CTOD averaging also leads to the more erratic load as a function of crack length curve shown in Figure 3.14, especially within the first 0.2 inches of crack growth, which is a main region of interest. Due to the large difference in runtime and smoother crack profiles, the ABAQUS procedure that uses both a “ranged” critical CTOD and averaged CTOD was used.

From Figure 3.14 it is seen that the ABAQUS analysis accurately follows the initial relation of the two-dimensional numerical analysis from Farley et al. [12]. However, the ABAQUS analysis reaches a higher load level, more like the load level reached in the experiment. The load predicted by the ABAQUS analysis reached a maximum of 2425 lbs, about 2 percent lower than the maximum load reached in the experiment, and about 2 percent higher than the numerical two-dimensional analysis. The surface crack length at maximum load from the ABAQUS analysis is 0.16 inches, while for both the experimental data and the two-dimensional analysis prediction the maximum load occurs at approximately 0.11 – 0.12 inches of crack growth, considerably less than the prediction from the ABAQUS analysis. As previously mentioned, there was only one experimental test performed by Farley et al. [12] on unreinforced specimens, so the surface crack length at maximum load could well average to 0.16 inches for a larger number of tests. The discrepancy in surface crack length between the ABAQUS results and the two-dimensional numerical analysis is linked to the inability of the two-dimensional analysis to capture tunnelling effects and initial CTOA variation, as mentioned in the literature review, effects the ABAQUS analysis attempts to capture. The ABAQUS analysis does give a closer estimation for surface crack length at maximum load than the plate thickness over-estimation of other three-dimensional models given in Chapter 2. Although the two-dimensional analysis gives a more accurate value of surface crack length at maximum load when compared to the experiment, the two-dimensional maximum load value is not as accurate as the predicted value by ABAQUS. Since measurement of the maximum load is the main objective of this research, this is a more critical value than the crack length. Generally, the fracture relation generated from the ABAQUS models lies between the relation from the experiment and the relation from the two-dimensional analysis for the main area of interest (i.e., within the initial 0.335 in. of surface crack length). After this initial portion, the ABAQUS relation remained within the scatter of the experiment, and was slightly higher than the relation from the two-dimensional FRANC2D analysis, but only by a maximum of approximately 5 percent.

The maximum load from the ABAQUS analysis of this unreinforced case is used as a normalization parameter for all subsequent reinforced cases. The ratio formed by normalizing is used as a measure of performance compared to the unreinforced case.

The tunnelling magnitude, T, calculated from Equation 2.11 from the ABAQUS analysis is shown in Figure 3.15 as a function of surface crack length, Δa. As shown in

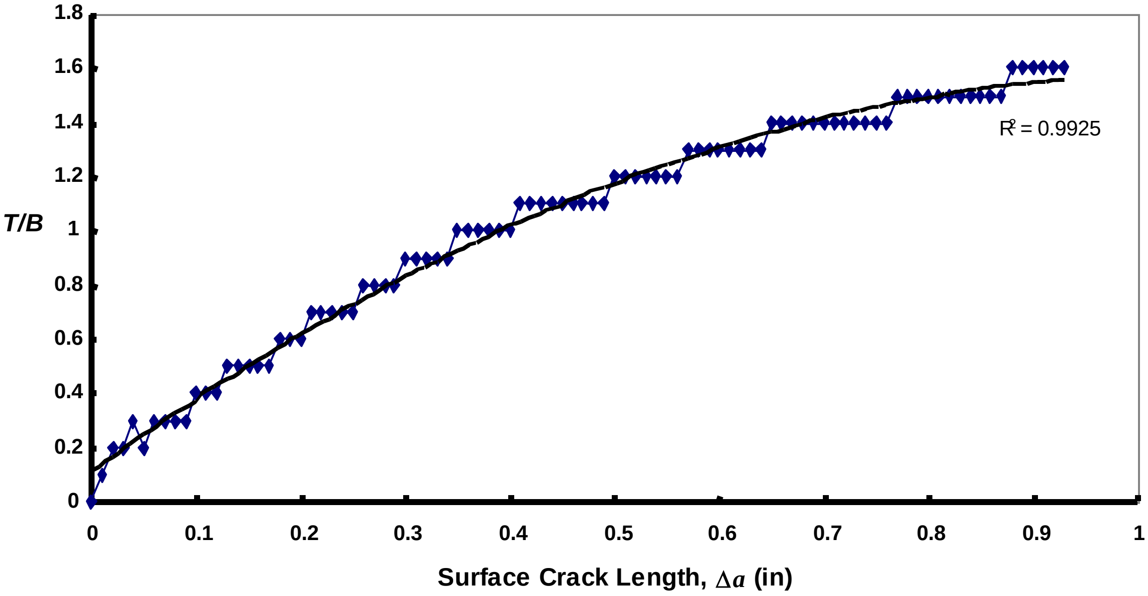

Figure 3.15 Tunnelling Magnitude, T

Figure 3.15, T continually increases as the crack grows, and begins to level off to a value of $T/B = 1.6$ at $\Delta a = 0.9$ in., or at approximately nine specimen thicknesses of crack growth. As mentioned in Chapter 2, James et al. [33] reported a normalized maximum tunnelling magnitude of approximately 1.1 and Dawicke et al. [16] reported a maximum magnitude of approximately 1.7, both occurring at one to two specimen thicknesses of surface crack growth, considerably less than nine specimen thicknesses. However, the ABAQUS analysis does seem to eventually level off close to the tunnelling magnitude of Dawicke et al. [16].

Even the ABAQUS analysis using the smaller 0.005 inch element size had approximately the same tunnelling magnitude.

Recall the analysis from Dawicke et al. [16] was based on a plate thickness similar to the current study. Both of the studies of James et al. [33] and Dawicke et al. [16] used a 2000-series aluminium. It is not clear that 7075 aluminum behaves the same way, as empirical data for this alloy and this geometry are not available in the literature. Assuming the two alloys do behave similarly, one reason for the discrepancy of the tunnelling magnitude could be the variation of the initial critical CTOA through the thickness of the specimen, as previously mentioned in Chapter 2 from Dawicke et al. [16]. To implement this procedure in ABAQUS would require a more involved determination of the initial critical CTOA variation, and further knowledge of midplane CTOA variation that was not fully detailed in Dawicke et al. [16]. Implementation of such a procedure would require experimental measurement of the critical CTOA at the midplane. This would be difficult to do. Despite this possible overestimation of surface crack length as it relates to the tunnelling magnitude, the load vs. surface crack length relations are close, tunnelling is being modelled, and there is further evidence that the ABAQUS analysis is credible, as discussed next.

Besides overall response such as the load vs. surface crack length relations, more detailed results from the ABAQUS analysis of the unreinforced compact tension were compared to the equations for estimation of the plane-stress plastic zone size from Equation 2.1. The plastic zone size along $Y = 0$ (the crack plane) and at $Z = -B/2$ (the free surface) as a function of surface crack length is given in Figure 3.16. The equations used for this plot assume plane-stress conditions, since that is what occurs at the free surface. As can be seen from Equation 2.1, given the same material and geometry, all that is needed to calculate the plastic zone size is the stress intensity factor, K, from the load vs. surface crack length relation. Four different calculations are shown in Figure 3.16: three of which use Equation 2.1 to calculate the plastic zone size, and one of which comes directly from the ABAQUS

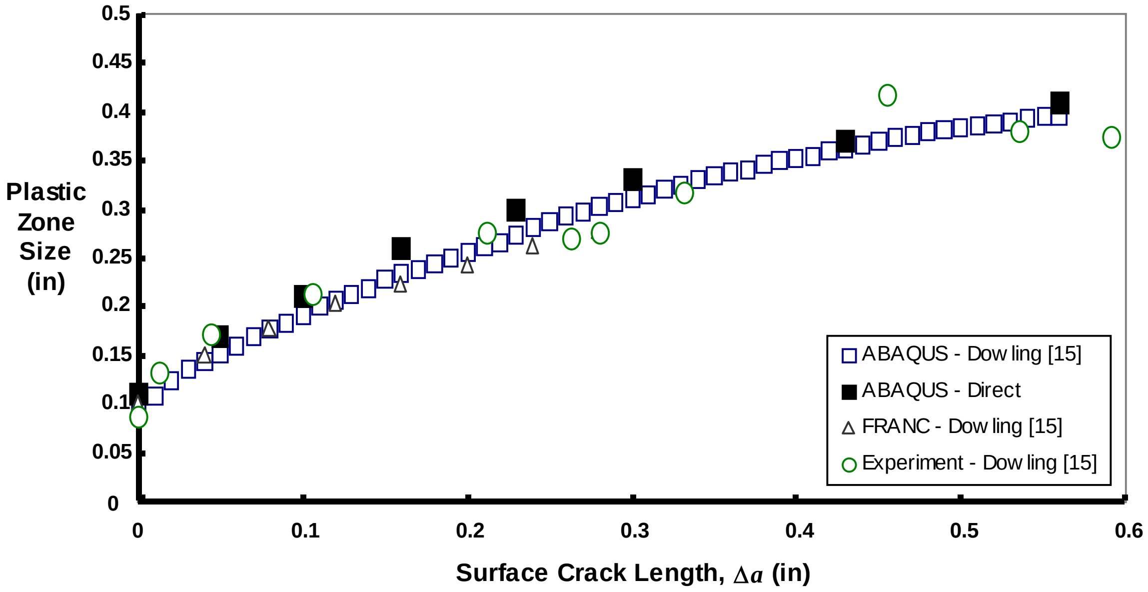

Figure 3.16 Plane-Stress Plastic Zone Size Comparison as a Function of Surface Crack Length

analysis. Of the three calculations of the plastic zone size based on Equation 2.1, one uses the experimental data from Farley et al. [12], another uses load and crack length results from the two-dimensional finite element analysis from Farley et al. [12], and one uses load and crack length results from the ABAQUS analysis.

As seen from Figure 3.16, the plastic zone size directly from the ABAQUS analysis and prediction from Equation 2.1 using the load and crack length data from the ABAQUS analysis are within 10 percent of each other. The difference is greatest for shorter surface crack lengths, i.e., Δa less than 0.22 inches. The reason for this difference is the validity of the calculation for the stress intensity factor, K, from Equation 2.3. The surface crack length value of 0.22 inches corresponds to an a/W of 0.2. The calculation of F_p given in Equation 2.4 is within 10 percent only for a/W values greater than 0.2. Despite this difference, the plastic zone sizes are still fairly close to the calculated approximations. This gives evidence that the mesh size and mesh type used in the ABAQUS analysis are sufficient.

Comparing the results from the ABAQUS analyses with the calculated plastic zone sizes from the experimental and as predicted using FRANC data, the agreement is quite good, as shown in Figure 3.16. This gives evidence that not only is the mesh size and type used in the ABAQUS analysis sufficient, this also shows that the plasticity formulation and crack propagation procedure are also valid.

Finally, strain variations assuming LEFM is valid are calculated. The assumptions of LEFM are not technically applicable for this large-scale plasticity problem, according to the limiting conditions of Equation 2.6. The reason is that the surface crack length is too small compared to four times the plane-stress plastic zone size. However, the surface crack length is still approximately two or more times the size of the plane-stress plastic zone size when using experimental data and results from FRANC2D and ABAQUS analyses as a basis. Therefore, the stress and strain fields based on LEFM may still provide an approximation to the stresses and strains for this problem. The strain ε_{yy} is the primary focus, since reinforcement failure will eventually be based on ε_{yy}, as previously stated, and as this is the component of strain causing the crack to propagate.

The stress intensity factors are calculated from both Equation 2.3 and 2.11, with the latter using the plastic zone size adjustment. Equation 2.11 is considered "fully converged" after eight iterations, as the difference in K_e (Δa = 0.3 inches) from the previous step is less than 0.2 percent. All other K_e values for Δa less than 0.3 inches is less than 0.2 percent from the previous step. Equations 2.8 and 2.9 with a plane-stress assumption are used to calculate the distribution of strain component ε_{yy} when Δa = 0.12 inches and with $\theta = 0$. These two distributions, shown in Figure 3.17, are compared to two distributions calculated from ABAQUS. One ABAQUS analysis is the full elastic-plastic analysis, and the other analysis uses the same applied load and crack length, however the model assumes a straight crack front, and the material is linear-elastic. Using this crack length of Δa = 0.12 inches assumes that the calculation of the stress intensity factor, K, is close enough to the experiment from the previous calculation of the plastic zone size. The plastic zone size is approximately 0.2 inches for this combination of geometry and loading, so comparisons to the elastic-plastic ABAQUS analysis should only be made for distances greater than 0.2 inches. This surface crack length was chosen since in the ABAQUS analysis this surface crack length and corresponding maximum load extends the yield strain contour to where the leading edge of the reinforcement would be located.

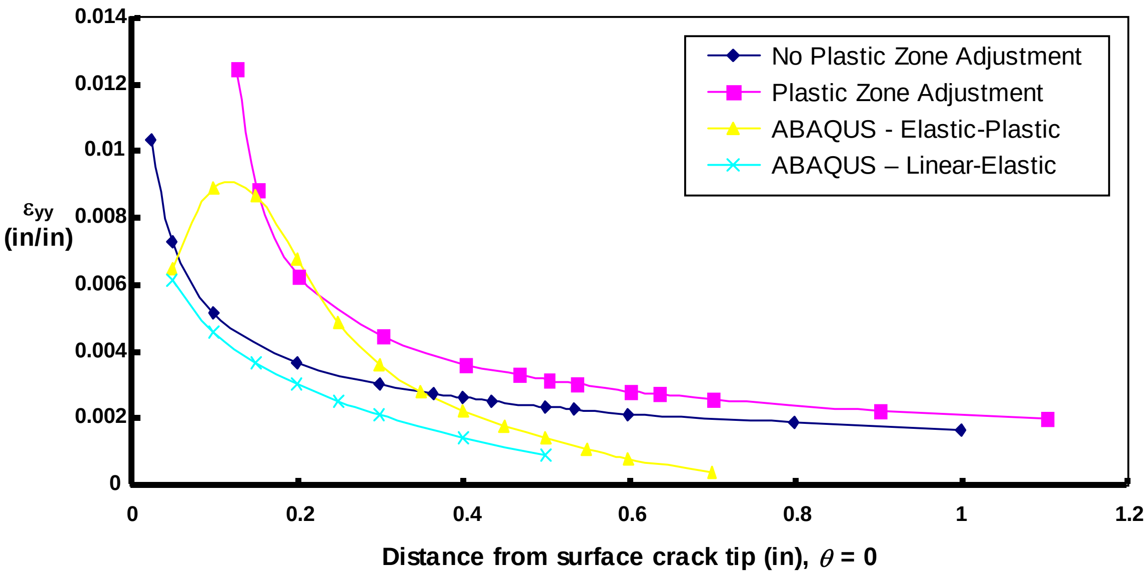

Figure 3.17 ε_{yy} **Strain Comparisons as Function of Distance Ahead of Crack Tip (*X*-*Y* plane)**

As shown in Figure 3.17, the difference between the two calculated LEFM curves of Equations 2.3 and 2.11 is similar to the difference between the two ABAQUS curves. However, although the overall shapes are similar, both ABAQUS analyses show a much more rapid drop in strain than the LEFM predictions, and at some point the ABAQUS analyses actually go negative. There are several reasons to this, most of which are related to Equation 2.6 for LEFM validation. First of all, LEFM assumes an approximately infinite plate subjected to a uniform tensile load. This is why the LEFM approximations never go below zero, as it is impossible according to Equations 2.8. In the case of a compact tension specimen, in order for this type of infinite plate/uniform tensile load approximation to be valid, the applied pin load must be sufficiently far away from the crack tip. As previously mentioned, according to Equation 2.6, it is not. The crack length is still too short for LEFM to be applicable. The applied load is too close, thus creating a moment and tensile *X*-direction stress at the crack tip, creating a superposition of stresses due to this moment and the crack tip singularity. As shown in Figure 3.17, this is why there is a drop in ε_{yy} strain closer to the crack tip. σ_{xx} stresses are higher due to the relatively close proximity of the applied moment. This actually limits ε_{yy} due to Poisson contraction. From LEFM, at $\theta = 0$, the *X*- and *Y*-direction stresses are the same. From the ABAQUS analyses, they are not, as the moment causes additional σ_{xx} on top of the crack tip singularity stresses. The σ_{xx} stresses even extend further out in the X-direction than σ_{yy}. This again causes Poisson contraction, and thus lowering ε_{yy}. If plasticity is strictly the reason for this difference in ε_{yy} between the ABAQUS and LEFM predictions, the linear-elastic ABAQUS analysis would decrease at a rate similar to the LEFM prediction, but it does not. The results of the linear-elastic ABAQUS analysis also suggest this superposition of local moment and crack tip singularity. Finally, close to the crack tip, the element type would not be sufficient. For a crack tip, due to the $1/\sqrt{r}$ dependence from Equations 2.8, elements with nodes at ¼ points along each element length would capture crack tip stresses more accurately, as suggested from Sanford [42]. These elements were not used due to the 1:1:1 element aspect ratio and the requirement on linear elements discussed in Section 3.3.2. As already shown, the overall unreinforced fracture response is accurate for this case. This also suggests that the distance L_c is far enough away from the crack tip singularity to not be affected. Therefore, despite the capturing of stress and strain fields right at the crack tip singularity, overall response is still adequate for this investigation.

From the ABAQUS analysis, as seen in Figure 3.18 and normalizing by the yield strain, ε_0, the maximum strain occurs at $\theta = 60$ degrees, with the absolute maximum peak at a

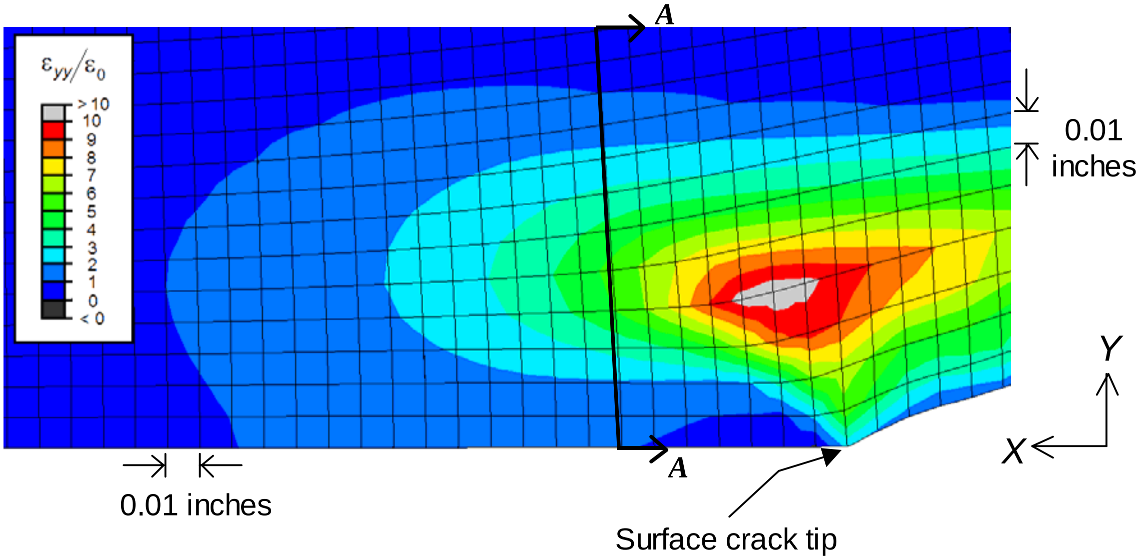

Figure 3.18 ε_{yy} Contour Plot (X-Y Plane, Z = -B/2), Section A-A Shown for Figure 3.20

Y-position of 0.04 - 0.05 inches, as shown in Figure 3.18. It is interesting to note from Equation 2.8 that for $\theta = 60$ degrees the shear stress is zero, and therefore, the resulting X-

and *Y*-direction stresses are principle stresses. At this angle, the *Y*-direction stress is a maximum, therefore a larger *Y*-principle strain. Keep in mind that the material within a 0.1 radial distance from $Y = 0$ and 0.1 inches ahead of the crack tip is all plastic, including this point of maximum strain on the surface. So, despite the strict limitation of Equation 2.6 to the linear-elastic stress and strain calculations of Equations 2.8 and 2.9, LEFM approximations with and without the plastic zone adjustment can still show the general strain trends for this combination of geometry and loading, as well as shed some additional insight into the strain variations.

At this point, the ABAQUS unreinforced compact tension model and crack propagation procedure have been validated. This validation is based on comparisons of experimental data, the results of a two-dimensional numerical analysis, as well as analytical approximations to the three-dimensional problem. However, before turning attention to the reinforced models, several additional points must be mentioned regarding the *Y*-direction strain fields.

Since composite reinforcement failure is based on the maximum value of strain component ε_{yy}, it will be important to see how the contours of maximum strain change and interact with the reinforcement leading edge as a function of reinforcement architecture. As will be shown later, since the failure strain of the composite reinforcement is approximately equal to the yield strain of the base aluminum, the relatively large plastic zone size (more than two times the plate thickness) suggests that composite reinforcement failure occurs well before the surface crack reaches the reinforcement leading edge for the fracture surface orientation assumed from the ABAQUS analyses. To that end, the variations in strain component ε_{yy} along the crack plane (the *X*-*Z* plane) are shown in Figure 3.19. As depicted in Figure 3.19, the highest extensional strain contour extends furthest in the *Y*-direction at the midplane of the compact tension specimen ($Z = 0$). This is similar to what has been seen in previous work from Hom and McMeeking [34]. Newman et al. [32] observed large through-thickness gradients of the stress component σ_{yy} for thin metals, which would give rise to such a phenomenon. This variation through the thickness of the extensional strains ε_{yy} also gives rise to the tunnelling effect.

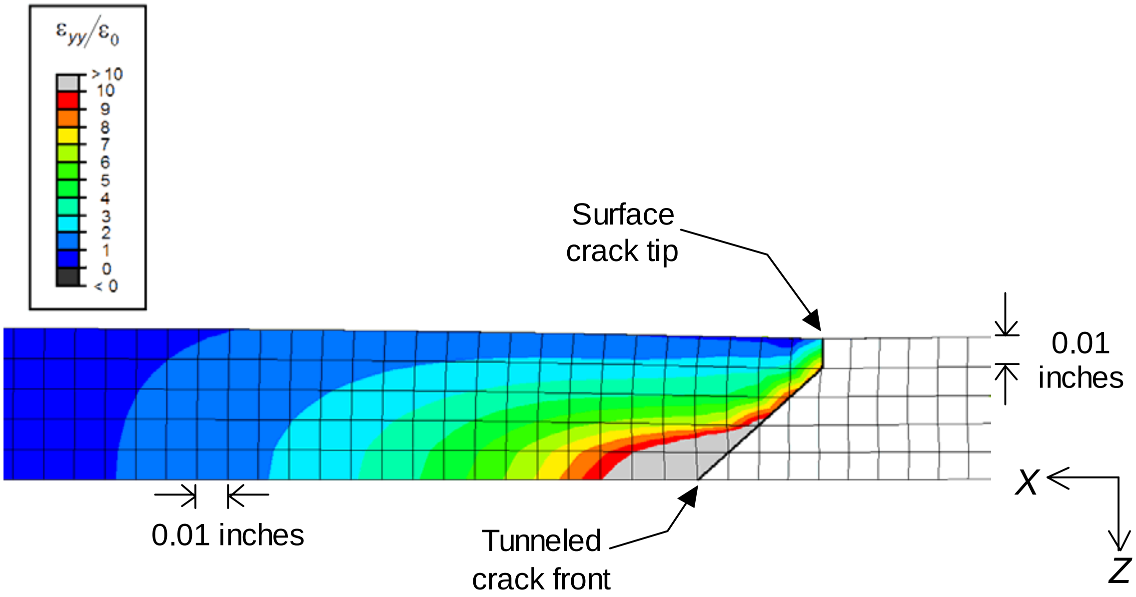

Figure 3.19 ε_{yy} Contour Plot (*X*-*Z* Plane, *Y* = 0)

The 45-degree locus of maximum value of strain component ε_{yy} through the thickness for thin materials, as seen from the model of Hom and McMeeking [34] and experimentally for others mentioned in Chapter 2, is shown in Figures 3.18 and 3.19. At a given *Y*-*Z* plane location ahead of the crack front, the maximum strain occurs at the specimen midplane (Figure 3.19) along the crack plane, and along an approximately 45-degree angle to the outer surface. Figure 3.20 is shown to more clearly illustrate this effect. A careful examination of Figure 3.20 will reveal that the actual angle of maximum strain contour is between 35 degrees and 45 degrees relative to the horizontal. The former angle corresponds to failure along an octahedral plane [15]. Assuming that material orientation (*T*-*L* vs. *L*-*T*) does not matter, the fact that a rotated fracture surface is definitely possible for this geometry is supported by Figures 3.18 - 3.20. The maximum strain magnitudes at the midplane extend only slightly further from the surface crack tip than at the free surface (approximately 0.02 – 0.04 inches). The extensional strain contours ε_{yy} are shown in Figure 3.21. These contours

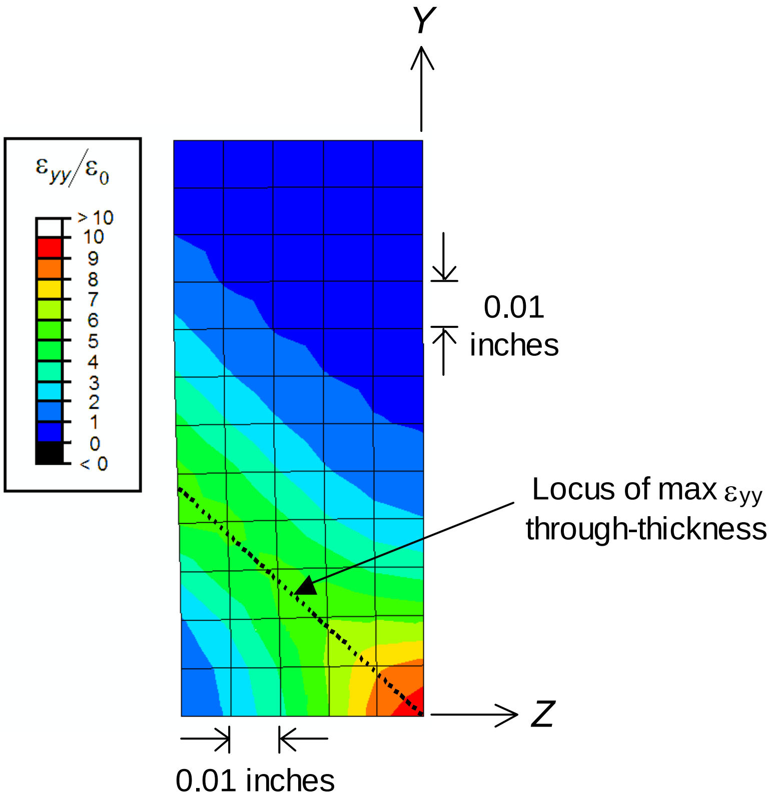

Figure 3.20 ε_{yy} Contour Plot (*Y-Z* Plane, Section *A-A* from Figure 3.18)

also correlate with the results from James et al. [33] and Dawicke et al. [36] that conclude that for a rotated crack, the tunnelling magnitude is relatively low (0.02 – 0.04 inches). As previously mentioned, although a rotated fracture surface is not considered in this research, and is, in fact, precluded due to the quarter-symmetry assumptions, it would be interesting to know what effect of allowing the fracture to rotate would have on the strain fields.

As the contour plot of Figure 3.21 shows, strain contours along the *X*-direction at the midplane tunnelled crack front start relatively high and die off fairly quickly. Once reinforcement is included, where these high strain levels reside and change gives clues as to the reasons why one architecture outperforms another.

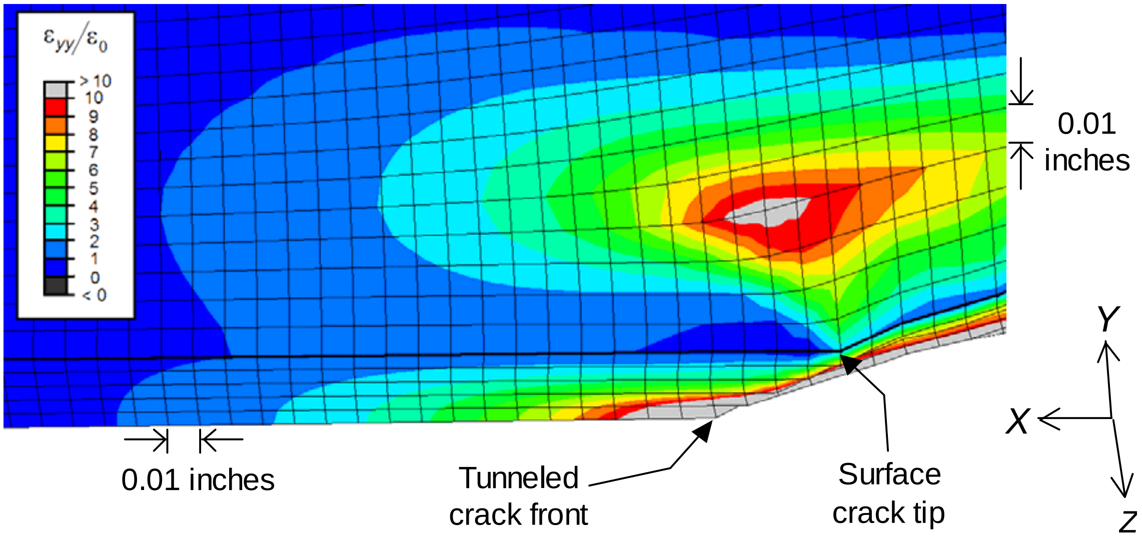

Figure 3.21 Rotated ε_{yy} Contour Plot

Details on the maximum ε_{yy} strain contours for the unreinforced case have now been given. As shown in Figure 3.21 above, these contours extend furthest at the midplane, while also extending 0.04 – 0.05 inches away from the crack plane in the *Y*-direction on the surface. The maximum strain contour on the surface "lags" behind the midplane strain by approximately 0.02 – 0.04 inches.

The unreinforced model and crack propagation procedure have been discussed in detail and the predictions compared with past results. The details of the modelling reinforced cases are similar, however there are certain modelling considerations that are discussed in the next section.

3.4 Considerations for Modelling of Reinforced Compact Tension Specimens

Certain considerations for analysing the reinforced compact tension geometries are discussed in this section. Similar to the discussion for the unreinforced geometry, dimensional considerations are given first, followed by the identification of different materials used, then consideration of boundary and symmetry conditions, and finally, consideration of the finite element mesh. Comparisons between maximum load predicted by the three-dimensional ABAQUS analysis of a reinforced specimen and the results of Farley et al. [12] are discussed.

3.4.1 Dimensions

The overall dimensions of the compact tension specimen remain the same as the unreinforced case. However, due to the in-situ reinforcement, some regions of the specimen consist of a reinforcement material rather than 7075 aluminum. One of the reinforcement geometries used in Farley et al. [12], and used here, is shown in Figure 3.22. This figure

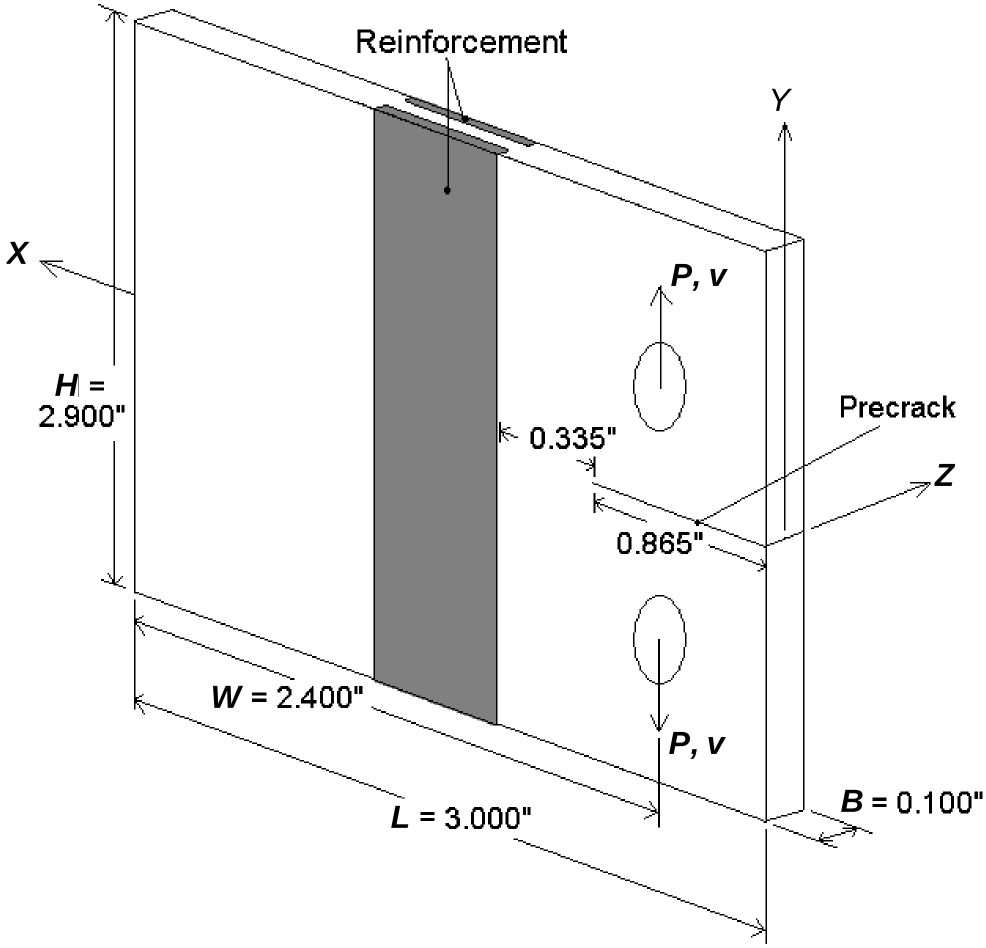

Figure 3.22 Reinforced Compact Tension geometry, Dimensions, and Coordinate System

shows a reinforcement scheme that uses a rectangular reinforcement embedded within the free surface. In a later section, this specific reinforcement geometry will be referred to as architecture 1. The distance in the X-direction between the initial crack tip and the nearest reinforcement edge is 0.335 inches. This distance between the initial crack tip and the reinforcement leading edge is the same for all architectures.

To facilitate the comparison of the performance of different reinforcement architectures, the cross-sectional area of all reinforcement architectures are designed to be the same. The total cross-sectional area of the reinforcement shown in Figure 3.22 and used in Farley et al. [12] was 0.02 in^2 and this area is maintained throughout the present study. Consider a reinforcement cross-section with a leading edge at $x = 0$ and trailing edge at $x = w$, as illustrated in Figure 3.23. The reinforcement is symmetric about a plane parallel to the Y-Z plane, which passes through the point $x = w/2$. The reason for this symmetry about the Y-Z plane is that in actual structures containing in-situ selective reinforcement, the direction from which cracks approach the reinforcement would not be known a priori.

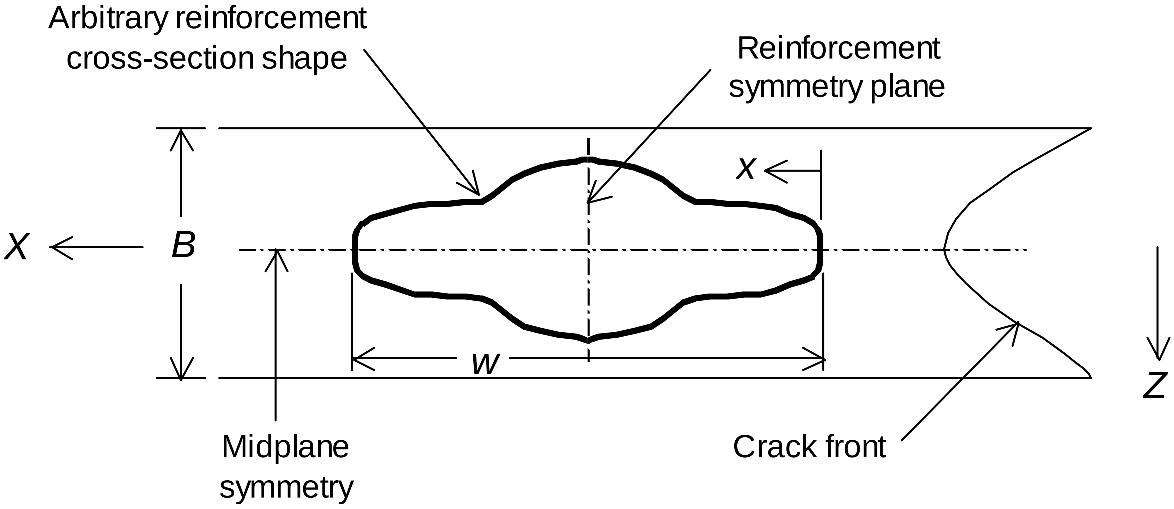

Figure 3.23 Reinforcement Symmetry

Specifics regarding the reinforcement placement, cross-sectional shape, and symmetry considerations have now been given. Descriptions of the different reinforcement materials and how each is modelled are given in the next section.

3.4.2 Reinforcement Materials

Besides variations in reinforcement architecture geometry, as previously stated, various reinforcement materials are used as well. Table 3.2 lists the mechanical properties and yield stress or ultimate strength of the reinforcing materials used in this study. In parenthesis are the calculated failure strains. Also included is how the materials are modelled in ABAQUS.

As seen in Table 3.2, two other aluminum alloys are considered in this analysis: an 1100-H18 alloy [43] and an aluminium-lithium alloy [44]. These two different alloys were chosen since they both have similar tensile moduli to the base aluminum 7075, but their yield strengths differ. The aluminium-lithium material has an approximately 30 percent higher yield stress than the base aluminum, while the aluminum 1100-H18 has a yield stress approximately 30 percent of the base aluminum. All aluminum alloys are assumed to be elastic-perfectly plastic, as most aluminum alloys are approximately described by this behavior. The aluminium alloys will be used with the unidirectional composite as a means of

Table 3.2 Material Properties of Reinforcement Materials Used in Analysis

Material	Elastic Properties	Yield Stress or Ultimate Strength (Failure Strain)	Represented in Analysis
Unidirectional Composite (Volume Fraction = 50%)	E_{11} = 19.0 Msi E_{22} = 35.0 Msi E_{33} = 19.0 Msi ν_{12} = 0.14 ν_{23} = 0.30 ν_{13} = 0.25 G_{12} = 6.84 Msi G_{23} = 3.85 Msi G_{13} = 6.84 Msi	250.0 ksi ($7.143(10^{-3})$ in/in)	Transversely Isotropic (Orthotropic) Linear-Elastic, Brittle
Aluminum 1100-H18	E = 10.0 Msi ν = 0.30	22.0 ksi (0.100 in/in)	Isotropic Elastic-Perfectly Plastic
Aluminum – Lithium Alloy	E = 11.0 Msi ν = 0.30	94.5 ksi (0.0800 in/in)	Isotropic Elastic-Perfectly Plastic

reducing the sharpness of the edges of the reinforcement. This will be discussed in the next chapter.

The unidirectional reinforcement used is the same reinforcement used in Farley et al. [12]. This reinforcement consists of a 50 percent volume fraction of alumina oxide (Al_2O_3) fibers embedded in an aluminum 1100 matrix. The reinforcement is modelled as an orthotropic linear elastic material, as is common for most composites. The reciprocity relations are used to calculate minor Poisson's ratios. Failure values of the composite in the shear directions and in the direction perpendicular to the fibers were not given, and failure in these directions not considered in Farley et al. [12]. Only fiber direction failure was considered by Farley et al. [12], and in this research as well. Composite failure is defined as occurring when the fiber-direction strain reaches the critical level given in Table 3.2.

It should also be noted that, coincidentally, the fiber-direction failure strain of the reinforcement is approximately equal to the base material yield strain (composite fiber-direction failure strain = 7.14 (10^{-3}) in/in and base aluminum 7075 yield strain = 7.25 (10^{-3}) in/in). This means that when fiber direction yield is reached in a base material element at the edge of the reinforcement, the reinforcement will be near failure.

3.4.3 Boundary and Symmetry Conditions

The boundary and symmetry conditions are exactly the same as in the unreinforced analysis. The only important item to note is that due to the symmetry condition at the midplane, any reinforcement architecture that includes this plane is a single reinforcement when considering the full thickness, as was shown in Figure 3.23. Architectures that do not include this plane actually consist of two separate reinforcements when considering the full thickness, one on each side of the X-Z plane. Again, this will be explained clearly in the next chapter. A quarter symmetry model is shown in Figure 3.24.

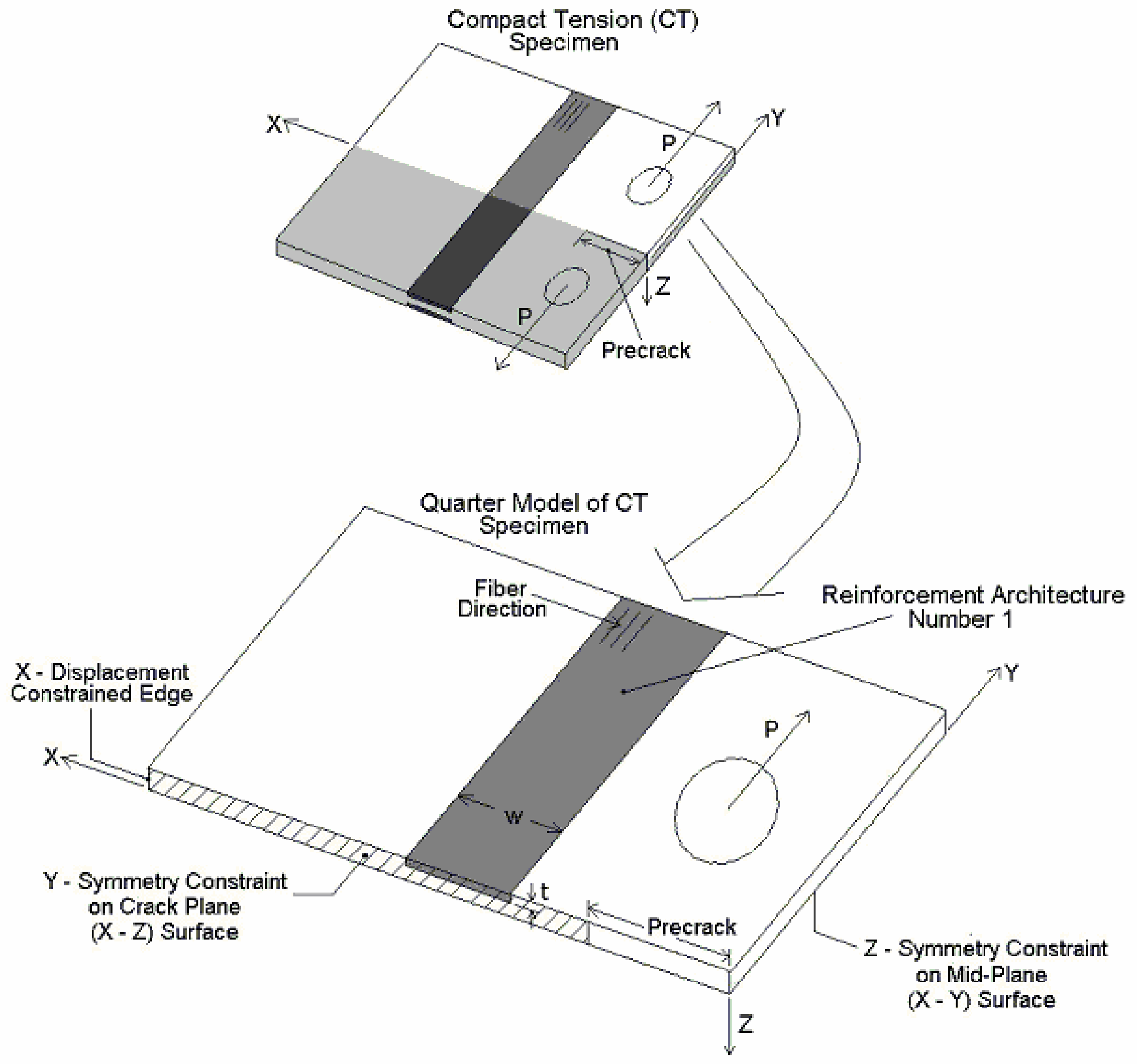

Figure 3.24 Quarter-Symmetry Model of Reinforced Specimen, Boundary Conditions, and Displacement

3.4.4 Finite Element Mesh

Since the crack propagation area, approximately from the leading edge of the reinforcement to the initial fatigued crack tip, is the same for every architecture, each reinforced model consisted of two separate portions: 1 - a portion consisting of the loading hole and crack propagation region, and 2 - a portion consisting of the reinforcement and the remaining base material. A close-up of the plane that separates these two portions, which is located at X = 1.175 inches, is shown in Figure 3.25. Therefore, instead of having to regenerate an entire model for each architecture, only the portion containing the reinforcement architecture has to be recreated. The reinforcement architecture portion is then

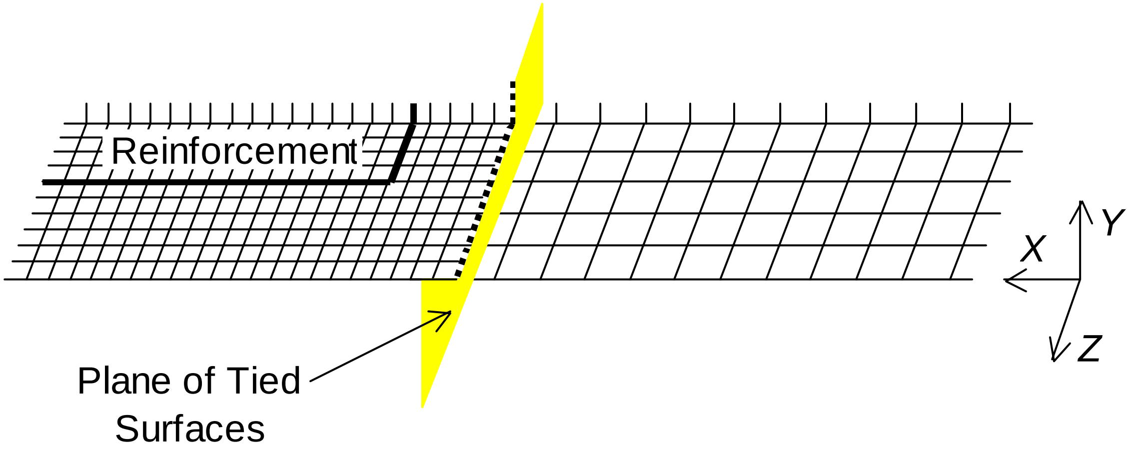

Figure 3.25 Close-Up of Tied Surfaces and Mesh Differences

connected to the crack propagation portion using the tie command in ABAQUS. Using the tie command to connect the two portions also allowed for a finer mesh density in the reinforcement architecture portion, within the reinforcement, and around the base material adjacent to the reinforcement where high stress gradients might occur. In the reinforcement cross-section the element lengths in both the X- and Z-directions is about 0.005 inches along an edge, or about 125 microns. The Y-direction element size was maintained at 0.01 inches. An analysis was performed on an unreinforced model to determine whether tied surfaces having non-coincident meshes alter crack growth response. Negligible differences occurred.

Most of the elements used in the portion containing the reinforcement are reduced integration, 8-node brick elements (C3D8R). These elements have been used in other, more complex analyses with ABAQUS (which actually include composite progressive failure [13]) and are suitable for this problem as well. The added displacement terms of the incompatible mode elements are also not needed in this portion, since reinforcement failure occurs before the crack reaches the leading edge of the reinforcement, which is shown later. Several other element sizes and types have been tried for the reinforcement. However, there was no difference in the fracture response up to initial failure of the composite reinforcement.

In some of the reinforcement architectures, wedge elements (C3D6) are also used. Due to the angular geometries involved in some cross-sections, as will be seen in the next chapter, and potential locking issues, wedge elements are limited to a small region.

The tied surface also limits the maximum amount of both inner (midplane) and outer (surface) crack propagation. Since the reinforcement part consists only of C3D8R and C3D6 elements, they are unable to adequately capture displacement fields, thus the maximum crack propagation length is 0.31 inches. This is the distance from the initial crack tip to the tied surface. As will be shown later, all initial reinforcement tensile failures and maximum loads occur well before this limit is reached. The remaining 0.025 inches from the tied surface to the reinforcement leading edge interface is required in order to limit artificial stress discontinuity contributions from change in materials, element type, tie surface constraints, and element size changes all occurring at the same point. As the strain contours will show, this is an adequate distance, as the contours are smooth and continuous after crossing the tied boundary, and before reaching the reinforcement leading edge.

A typical finite element mesh of the standard reinforcement case is shown in Figure 3.26. As discussed, two different types of 3-D elements are used for this analysis: wedge and brick elements. Of the brick elements, two linear sub-types are used: incompatible mode elements (C3D8I) and reduced integration elements (C3D8R). The wedge elements used are full integration linear wedges (C3D6). Figure 3.26 shows the location of each element type

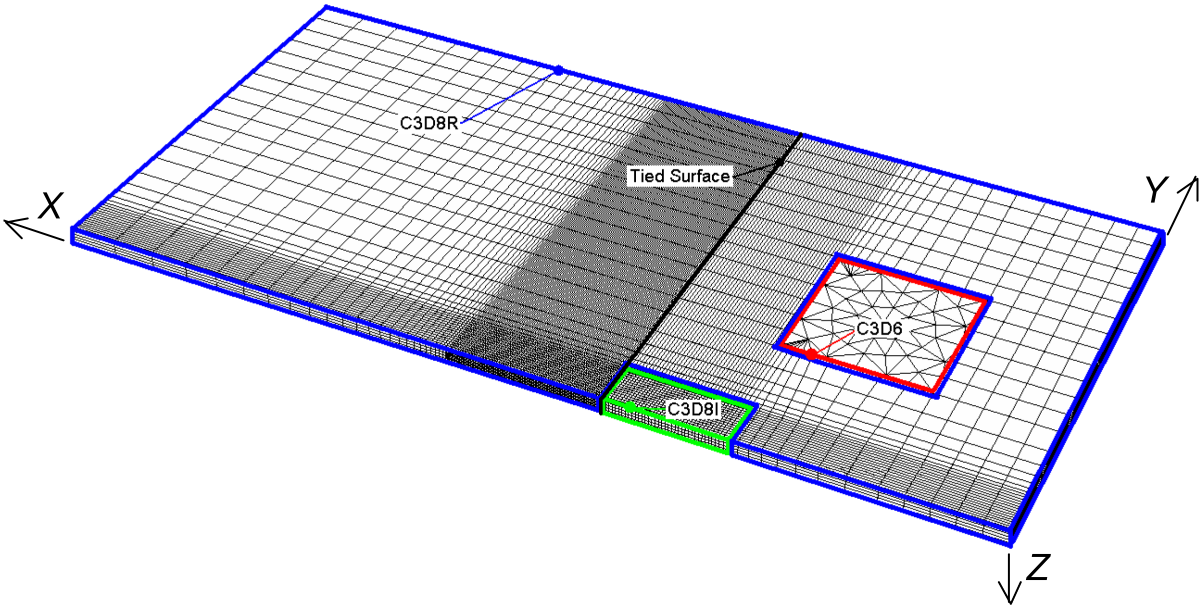

Figure 3.26 Finite Element Mesh of Reinforced Compact Tension Specimen with Element Types and Tie Boundary Highlighted

within the compact tension geometry, as well as the reinforcement region. As seen in Figure 3.26, the mesh is much more refined at the regions of interest, i.e., the crack propagation region (similar to the unreinforced case) and the reinforcement region.

Considerations for the analysis of a reinforced compact tension geometry have now been described. The maximum loads from two three-dimensional analyses using ABAQUS are compared with the maximum loads from two similarly modelled two-dimensional analyses of reinforced cases from Farley et al. [12]. Both cases involve two rectangular composite reinforcement strips on the outer surfaces. However, one case is modelled without an interface (e.g., welded), and one is modelled with an epoxy adhesive interface. A cross section of the reinforcement and interface are shown in Figure 3.27. The interface is shown in Figure 3.27, and the interface thickness, t_{int}, is 0.003 inches. Contact constraints are imposed between the leading and trailing edges of the reinforcement for the epoxy interface case. For the model without an interface, the interface material property is the same as the base 7075 aluminum. The epoxy interface is modelled as a linear-elastic material with a shear modulus of 0.1 Msi. The total thickness, t, in the figure is 0.02 inches.

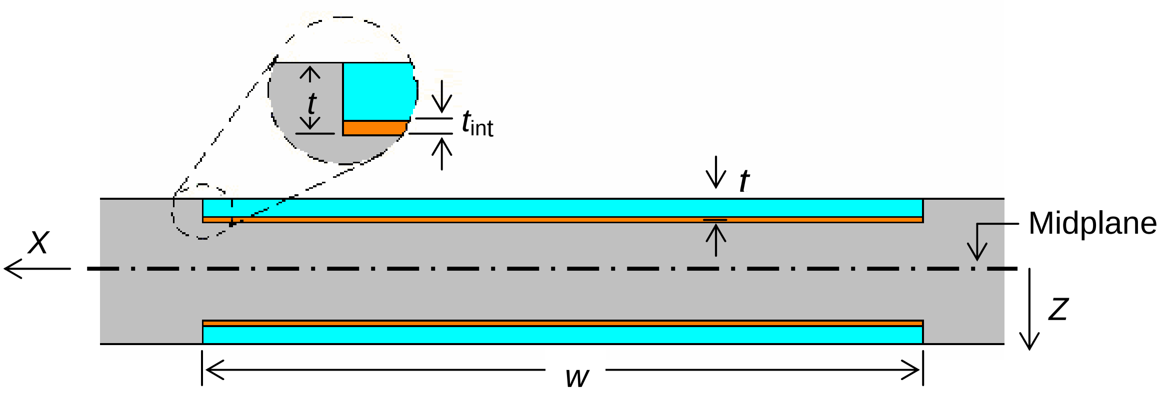

Figure 3.27 Cross-Section of Reinforcement and Interface

The maximum loads of the three comparison cases are shown in Table 3.3. One unreinforced case and the two reinforced cases are compared. Only two experiments were

Table 3.3 Comparisons of Maximum Loads

P_{Max} (lbs)	Experiment (Farley et al. [12])	FRANC2D (Farley et al. [12])	ABAQUS
Unreinforced	2478	2375	2425
Reinforced (epoxy interface)	2600	2631	2653
Reinforced (no interface)	N/A	2830	2845

performed: one using the unreinforced specimen, and another on the reinforced specimen with the epoxy interface. As can be concluded from Table 3.3, the ABAQUS analysis results are close to the maximum loads predicted by the two-dimensional FRANC2D analysis and the data from the experiment. As also shown in Table 3.3, and shown from Farley et al. [12], the reinforcement without an interface performs better than one that includes the interface. As previously mentioned, interface modelling is not the focus of this research, and thus will not be discussed further.

Results from using the three-dimensional ABAQUS analysis to study the unreinforced and reinforced compact tension specimens have been compared with previous published results. The strain predictions from the three-dimensional analysis have been presented. Attention now turns to the study of various reinforcement architectures. Descriptions of the different reinforcement architectures follow in the next chapter.

Chapter 4 CASE STUDIES

This chapter outlines the different reinforcement architectures analyzed in this research. Dimensions, constituent materials, and initial rationale for choosing each of the different reinforcement architectures are discussed next. As previously mentioned, all reinforced architectures have a constant cross-sectional area of 0.02 in^2 for the full thickness, thus 0.01 in^2 for the half-thickness. Each reinforcement architecture is assigned an architecture number, and separated into rectangular and triangular reinforcement cross-sections. The rectangular reinforcements will be described first, followed by the triangular. All subsequent discussions of reinforcement thickness and cross-sectional area apply to the quarter model. Therefore, for a reinforcement thickness of 0.02 inches, the total reinforcement thickness is 0.04 inches. This also means that a single reinforcement on the outer surface is actually two separate reinforcements for the full thickness, while a single reinforcement on the inner surface is still a single reinforcement for the full thickness, but twice as thick. All of the reinforcements are composed of the unidirectional composite, unless otherwise specified. A table summarizing architecture geometry, dimensions, and constituent materials is given at the end of each subsection.

4.1 Rectangular Reinforcement Architectures

4.1.1 Architecture 1

Architecture 1 consists of a single rectangular reinforcement on the surface (or two reinforcements on each surface due to midplane symmetry). Each reinforcement is 0.5 inches wide and 0.02 inches thick (w = 0.5 inches and t = 0.02 inches). This is similar to the previously mentioned architecture from Farley et al. [12] and is the baseline situation. This architecture is shown in Figure 4.1.

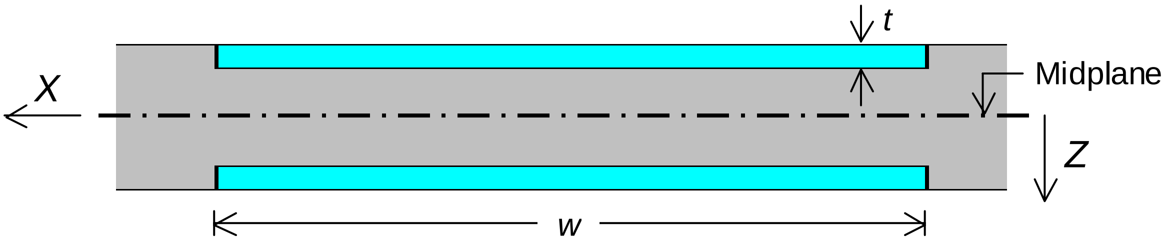

Figure 4.1 Architecture 1

4.1.2 Architecture 2

Architecture 2 is also a rectangular reinforcement, as shown in Figure 4.2. It has the same dimensions as architecture 1, however it is placed at the midplane, and is therefore a single reinforcement. This is a direct comparison to architecture 1, considering at the effect of location on the fracture response.

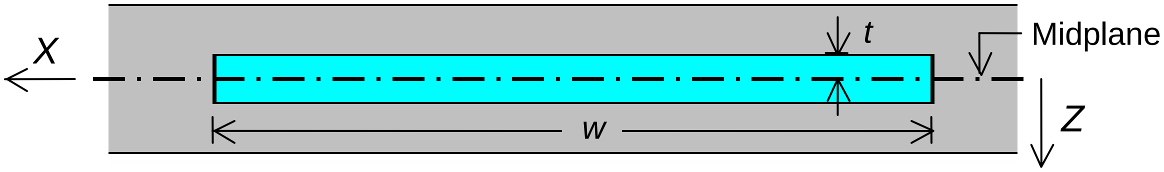

Figure 4.2 Architecture 2

4.1.3 Architecture 3

The effect of reinforcement thickness is analyzed in architecture 3. This architecture is a single reinforcement placed at the midplane, and is 0.04 inches thick. However, due to the constraint on the cross-sectional area, it is only 0.25 inches wide. This is a comparison to architecture 2, since both are located at the midplane, as shown in Figure 4.3.

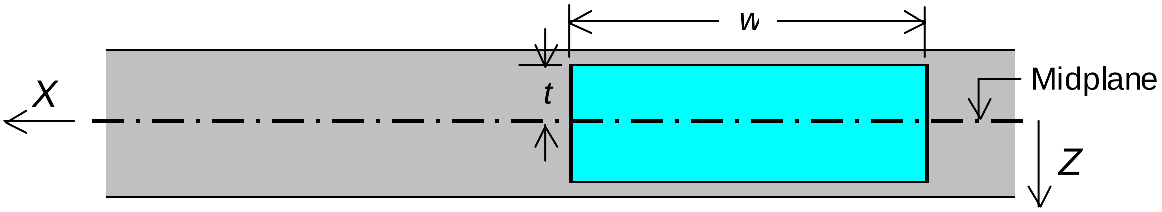

Figure 4.3 Architecture 3

4.1.4 Architecture 4

Due to the sharp corners in the previous rectangular architectures, giving rise to possible points of stress concentration, architecture number 4 uses a rounded leading edge to investigate the effect of leading edge geometry. This is a good comparison to architecture number 1, since it has the same width of 0.5 inches, thickness of 0.02 inches, and is located on the outer surface. The edge of the reinforcement is modelled as a quarter-circle, with a radius equal to the reinforcement thickness ($r = t = 0.02$ inches). It should be noted that this architecture has a slightly lower cross-sectional area than architecture 1 (0.0098 in^2 vs. 0.01 in^2). Architecture 4 is shown in Figure 4.4.

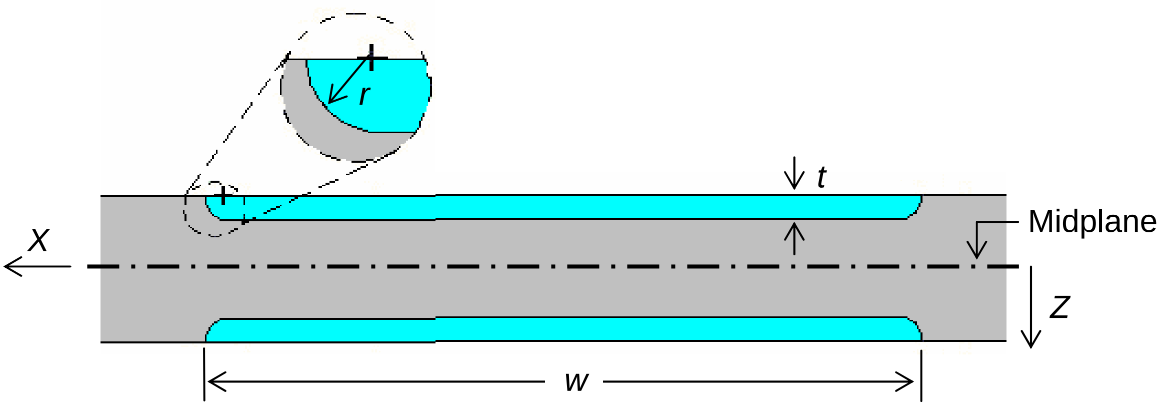

Figure 4.4 Architecture 4

4.1.5 Architecture 5

The effect of the width and spacing of multiple reinforcements is investigated with architecture 5. Another reason for investigating this architecture is to study how it would fail progressively, although this was not pursued in this research. This architecture consists of six discrete rectangular reinforcements, each 0.04 by 0.04 inches, placed at the midplane. The center-to-center spacing between each successive reinforcement is 0.1 inches, equal to the total plate thickness ($S = 0.1$ inches). The total width from the leading edge of the first reinforcement to the trailing edge of the last reinforcement is 0.54 inches. This total width is similar to the width of architecture 2. Architecture 5 also has the same total thickness as architecture 3. Comparing architectures 2 and 3 to architecture 5 provides insight into the effect of segmented reinforcements on fracture response. It should be noted that the total cross-sectional area of all six reinforcements is slightly lower than architectures 1 through 3 (0.0096 in^2 vs. 0.01 in^2). Architecture 5 is shown in Figure 4.5.

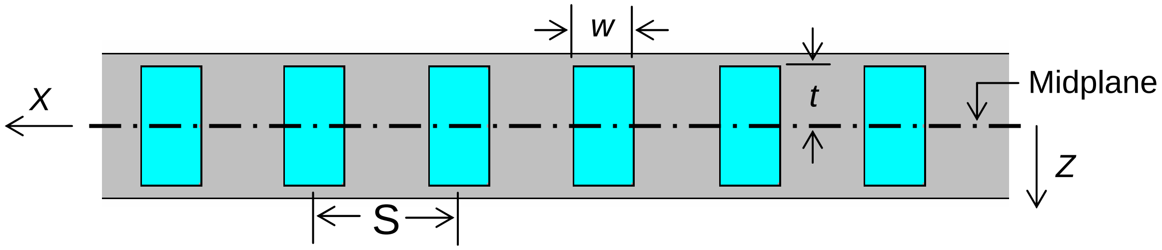

Figure 4.5 Architecture 5

Table 4.1 below summarizes all of the rectangular cross-section reinforcement architectures. The dimensions for each architecture are placed in terms of the dimensions for architecture 1.

Table 4.1 Table of Rectangular Reinforcement Architectures

		Rationale
1.	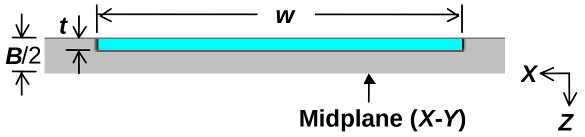	**Previous Work**
2.	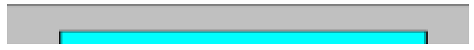	**Location**
3.	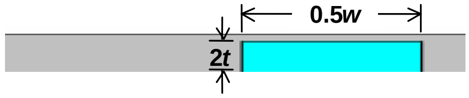	**Thickness**
4.	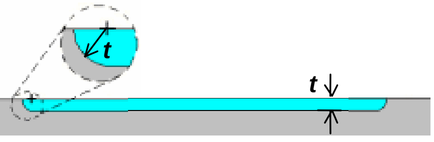	**Stress Concentration**
5.	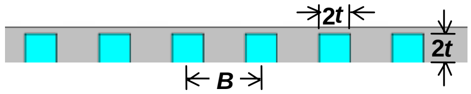	**Width and Spacing**

■ **Unidirectional reinforcement**

▨ **Base material – 7075-T6 Al**

The rectangular architectures have been described at this point. As previously mentioned, the triangular architectures are described next.

4.2 Triangular Reinforcement Architectures

The remaining architectures, six through eleven, have triangular reinforcement cross-sections. These are included to investigate how geometric (sharp vs. flat leading edge) and material changes influence fracture response, given the same total cross-sectional area. All triangular reinforcement architectures have a maximum thickness of 0.04 inches and a width of 0.5 inches (t = 0.04 inches and w = 0.5 inches). Another reason for investigating these triangular architectures is to study how each would fail progressively, although this was not pursued in this research.

4.2.1 Architecture 6

Architecture 6 consists of a triangular reinforcement on the outer surface. This architecture is used to investigate the fracture response of a sharp leading edge reinforcement versus a flat leading edge, as in architecture 1. Architecture 6 is shown in Figure 4.6.

Figure 4.6 Architecture 6

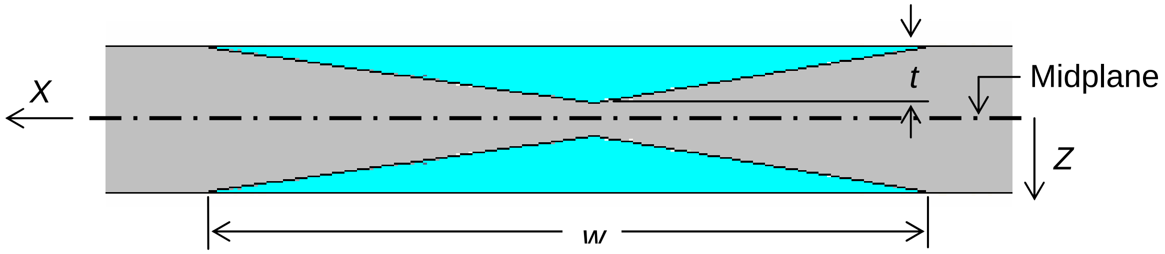

4.2.2 Architecture 7

Analogous to the comparison of location between architectures 1 and 2, architecture 7 shown in Figure 4.7 has a triangular reinforcement placed on the midplane. Keep in mind the symmetry constraint at the midplane, thus the inner triangular reinforcement architectures are actually diamonds at the full thickness. Architecture 7 can be compared to architecture 6.

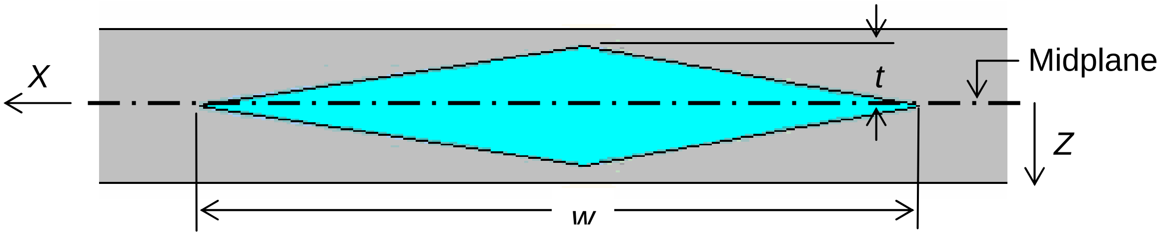

Figure 4.7 Architecture 7

Reinforcement architectures eight through eleven still consist of triangular reinforcements, however aluminum alloys of greater and smaller yield stress (Al-Li and 1100-Al alloys, respectively) than the base aluminum 7075 are applied to the tip. This is done to investigate what influence material changes at the leading edge, where reinforcement failure is expected to occur, would have on the fracture response.

4.2.3 Architecture 8

Architecture 8 shown in Figure 4.8 has the same overall cross-section as architecture 7, however with an 1100-Al at the tip. The length of this tip is 10 percent of the reinforcement half-width, or 0.025 inches (*k* = 0.025 inches).

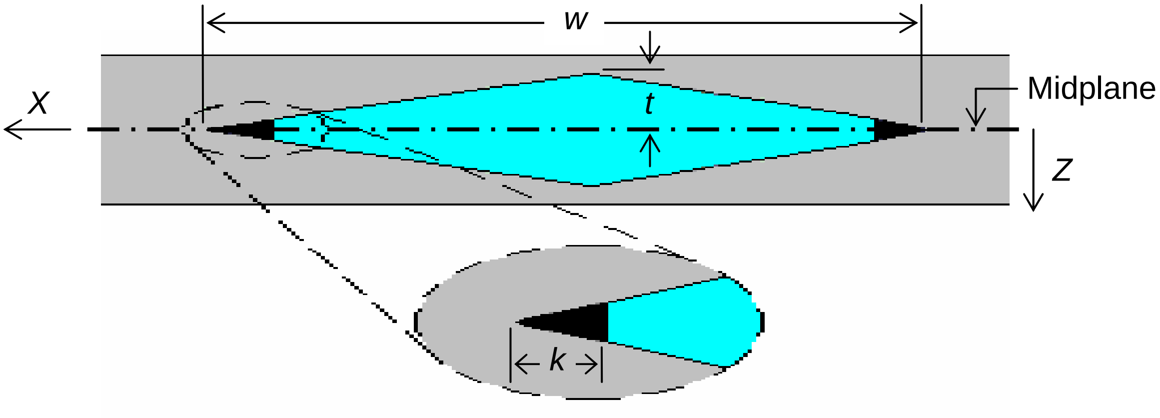

Figure 4.8 Architecture 8

4.2.4 Architecture 9

Architecture 9 is similar to architecture 8, however, instead the 0.025 inch tip is composed of an Al-Li alloy. Comparisons of architectures 7, 8, and 9 provide insight into the influence of how the addition of a small aluminum region at the tip of the triangular reinforcement with properties that differ from the base material influences fracture response. Architecture 9 is shown in Figure 4.9.

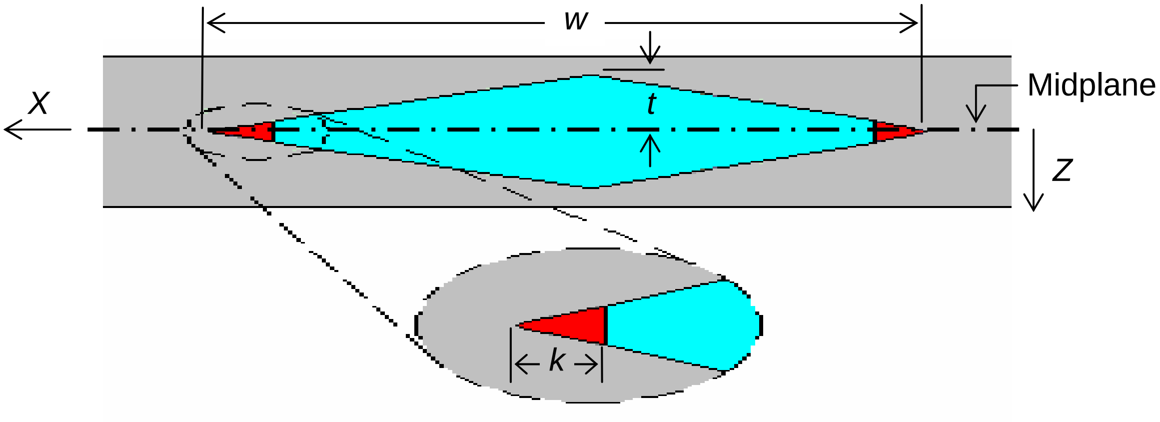

Figure 4.9 Architecture 9

4.2.5 Architecture 10

An 1100-Al tip is also used for architecture 10 shown in Figure 4.10, however the length of this tip is increased approximately two and a half times that of architecture 8, giving a tip length of 0.0625 inches (k = 0.0625 inches). The cross-sectional geometry

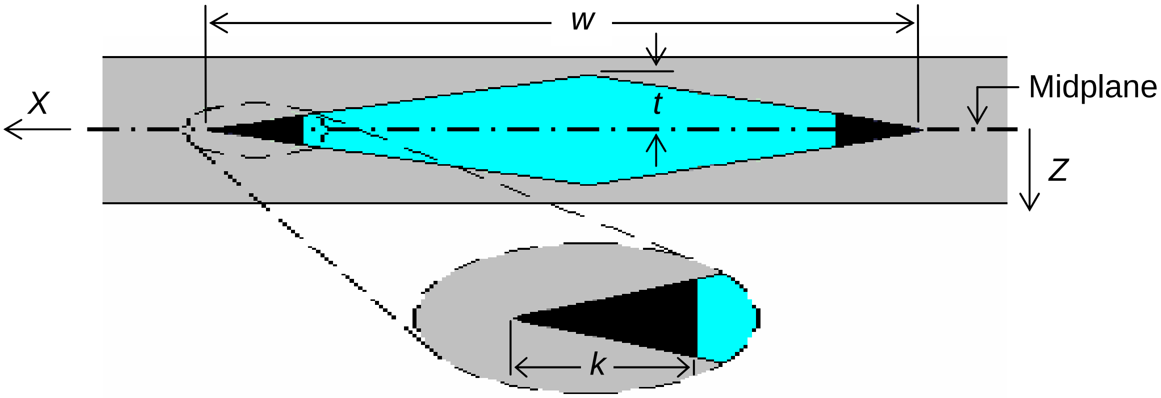

Figure 4.10 Architecture 10

remains the same, so comparing architectures 8 and 10 can provide insight into the influence of aluminum tip size on fracture response.

4.2.6 Architecture 11

Architecture 11 has approximately the same overall geometry as architecture 8, however, the reinforcement position is on the surface, and not on the midplane. Comparing architecture 11 to architecture 8 provides insight into the coupling effect of location and leading edge material on the fracture response. Architecture 11 is shown in Figure 4.11.

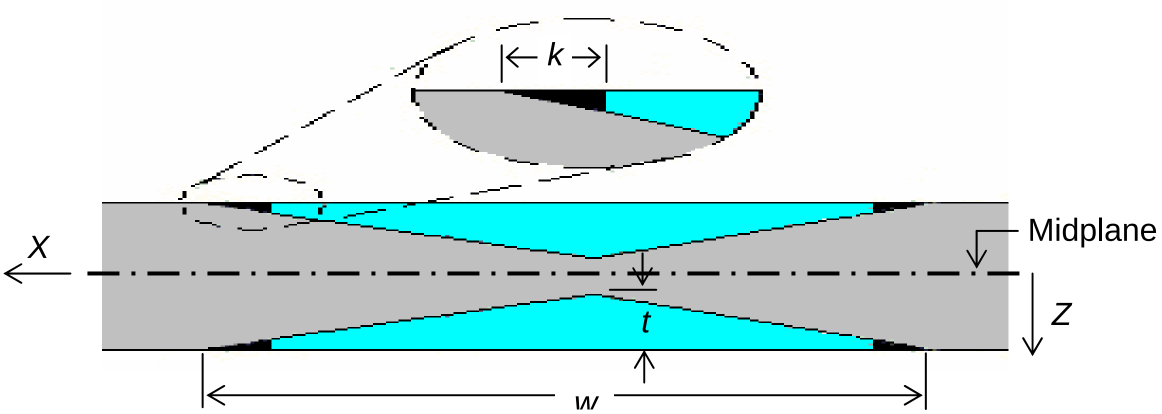

Figure 4.11 Architecture 11

A summary of the triangular reinforcement architectures is shown in Table 4.2. As previously mentioned, all triangular reinforcements have the same width and maximum thickness. The only changing dimension is the length, *k*.

All of the architectures have been fully described. The next chapter gives the results of each of the reinforcement architectures, and describes performances changes between each compared architecture.

Table 4.2 Table of Triangular Reinforcement Architectures

		Rationale
6.	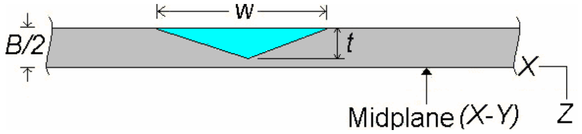	**Alternative to Rectangle**
7.	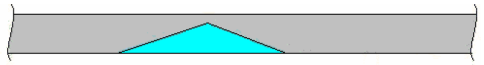	**Location**
8.	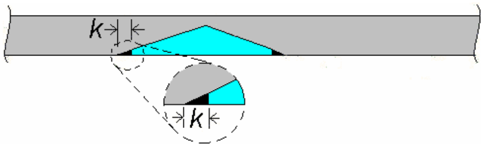	**Leading Edge Material**
9.	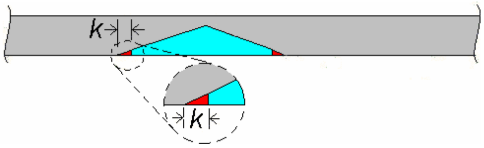	**Leading Edge Material**
10.	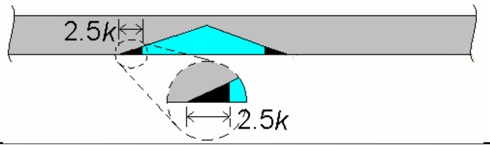	**Leading Edge Material - Length**
11.	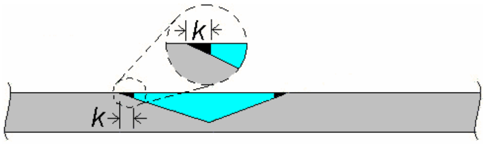	**Leading Edge Material - Location**

🟦 **Unidirectional reinforcement**

▨ **Base material – 7075-T6 Al**

⬛ **1100 - Al**

🟥 **Al - Li**

Chapter 5 RESULTS AND DISCUSSION

In this chapter gives results from the analysis of each of the reinforced architectures described in Chapter 4 are discussed. The rectangular and triangular reinforcement architectures are discussed separately. As the discussion proceeds, each of the architectures is compared to suitable counterparts, as mentioned in Chapter 4. For each comparison, important mechanics-related issues are presented to explain why one architecture performs better than another. Tables summarizing the performance of the architectures are given throughout the chapter.

5.1 Rectangular Reinforcement Architectures

Similar to what was done in Chapter 4, the rectangular reinforcement architectures are discussed first. Each architecture is discussed in a similar format, using the same contour plot perspective, same contour plot scaling, and same scaling of the load vs. crack length relation. This format is fully described during the discussion of architecture 1.

5.1.1 Architecture 1

The relation between the pin load, which is required to produce the pin displacement, and surface crack length for the unreinforced case and architecture 1 are shown in Figure 5.1. As seen, the relation for architecture 1 exhibits a monotonically decreasing slope until the maximum load at the initial fiber direction tensile failure of 2843 lbs. The surface crack length at maximum load is approximately 0.13 inches. Comparing these values to the baseline unreinforced case, the maximum load has been increased by approximately 17 percent. Although the surface crack length has been reduced by approximately 23 percent relative to the unreinforced case, an increased maximum load is the primary objective in this research. Therefore, architecture 1 provides an overall improvement in performance relative to the unreinforced case.

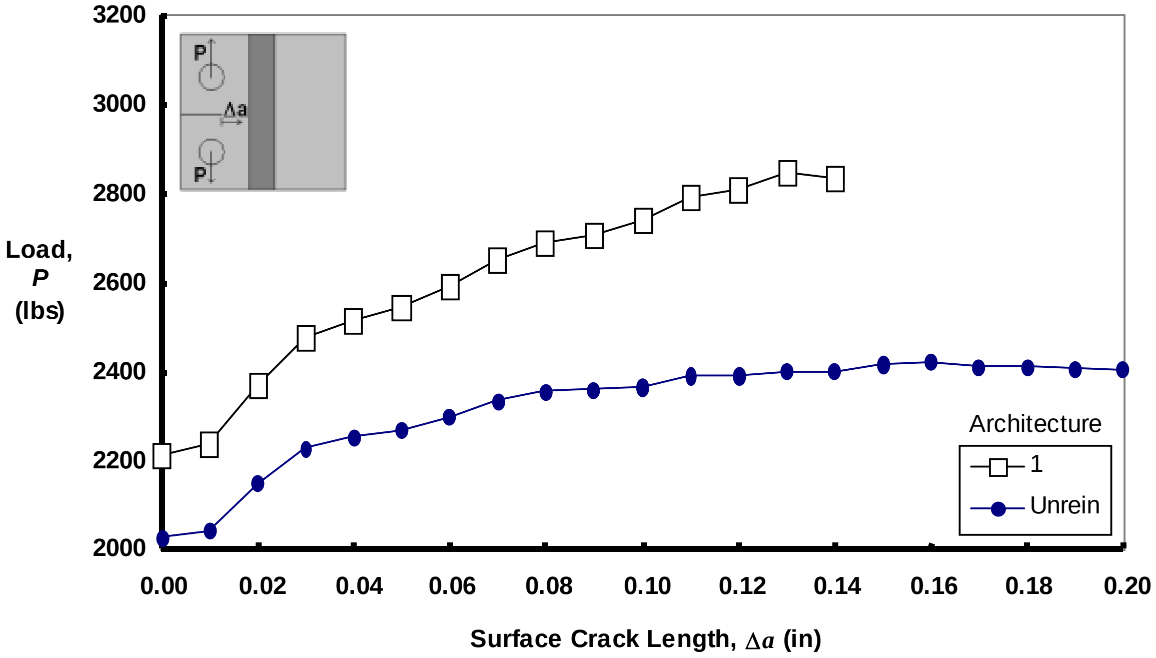

Figure 5.1 Load as a Function of Surface Crack Length for Unreinforced and Architecture 1

From Farley et al. [12], load sharing between the base material and the reinforcement was identified as an important mechanism for improving the performance of the reinforced compact tension specimen relative to an unreinforced one. It is expected that the reinforcing material is the main load-carrying mechanism, and when the reinforcement reaches failure levels, the specimen will fail catastrophically. As a measure of how much load the reinforcement is carrying relative to the load applied, the Y-direction (loading direction) load in the reinforcement is normalized by the reaction force measured at the pin due to the applied displacement, according to the following equation below:

$$R_f = \frac{F_{\mathrm{Rein}}}{F_{\mathrm{Pin}}} \qquad \text{(Eq. 5.1)}$$

where:

R_f = Load ratio

F_{Rein} = Sum of reinforcement nodal reaction forces

$F_{\mathrm{Pin}} = P$ (from Figure 2.2) = Reaction force at pin due to applied displacement at pin

Only the Y-direction loads are considered, since this is the direction in which the load is applied for Mode I testing. Reaction load in the reinforcement is primarily in this direction as well. Also, only the unidirectional composite reaction forces are considered, since the unidirectional composite will be the main load carrying mechanism, and failure of the unidirectional composite will most likely result in catastrophic reinforcement failure and unstable crack growth. At the end of each step in the analysis, equilibrium is achieved, so force equilibrium is still valid. Therefore, the remaining amount of load (F_{Pin} - F_{Rein}) is the amount of load carried by the remaining material.

The load ratio, R_f, as a function of surface crack length for architecture 1 is shown in Figure 5.2. Four different contour plots of extensional strain, ε_{yy}, are also shown corresponding to four different surface crack length conditions denoted on the plot by points A, B, C, and D. Point A corresponds to the initially straight (no tunnelling) precrack just prior to crack extension, and point D corresponds to initial fiber tensile failure in the composite reinforcement. Each of the extensional strain contour plots are of the same cross-section as in Figure 3.19. However, in the plots of Figure 5.2, the perspective is shifted in order to encompass the entire crack propagation area as well as a portion of the leading edge of the reinforcement, and the contour color bands are rescaled to denote yield of the base material in the extensional direction. Accordingly, the extensional strains are normalized by the extensional yield strain, ε_0. The crack front is depicted as a series of dots in Figure 5.2. As can be seen, the relation between R_f and surface crack length has a monotonically increasing slope to initial failure of the composite. Just prior to any crack growth, condition A, the reinforcement supports approximately 33 percent of the load, and the precrack is straight. The extensional strain contours through the thickness are highly curved at this point, despite the straight crack front, and a considerable amount of material has yielded. There is a considerable difference in amount of yielded material between the inner region of the specimen (Z = 0) and outer surface (Z = -B/2). At condition B, the reinforcement is supporting approximately 45 percent of the total load, and crack tunnelling has developed. Results from Dawicke et al. [16] also report a large degree of tunnelling within the first plate thickness of crack growth. Considerable extensional yielding of the base material ahead of the crack front is seen for the condition at point B, and has actually increased relative to

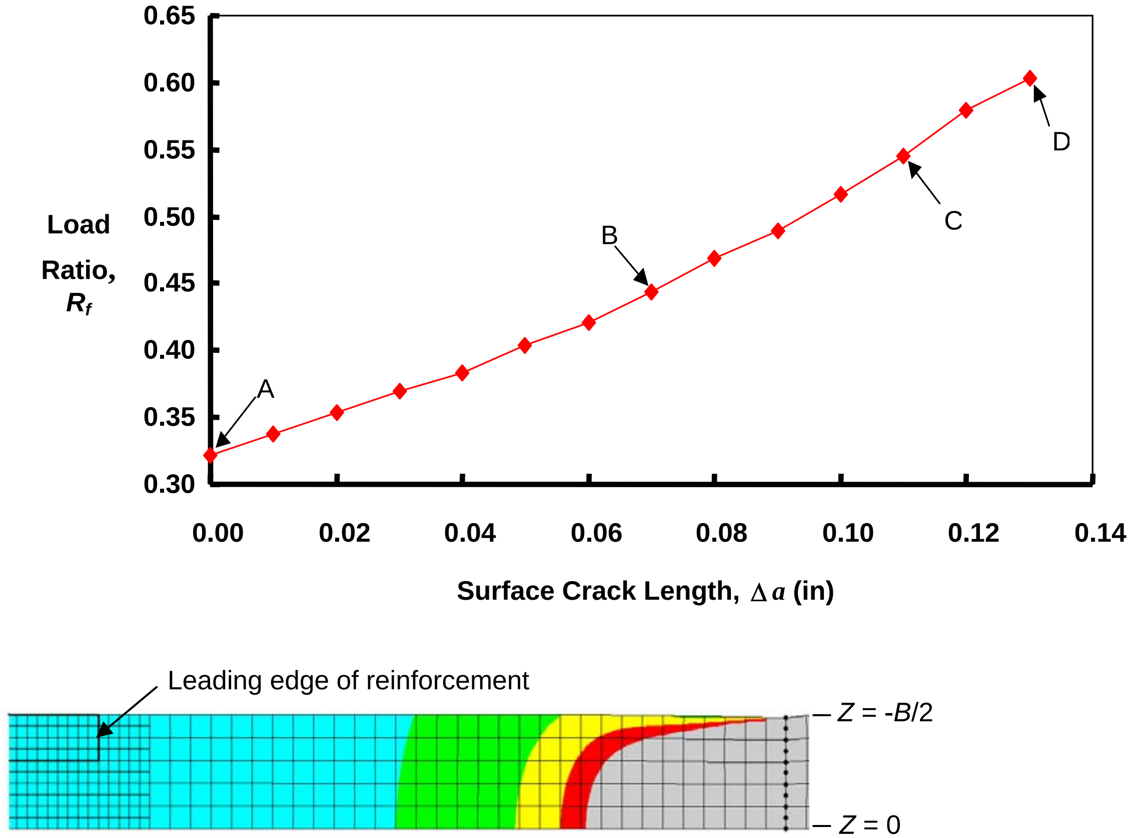

a) Strain contours of condition A

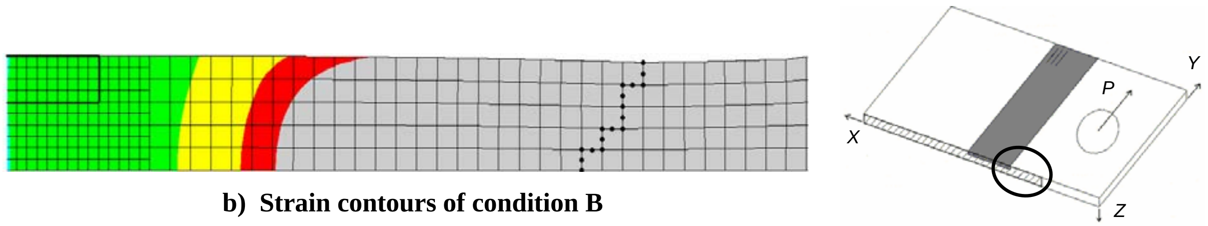

b) Strain contours of condition B

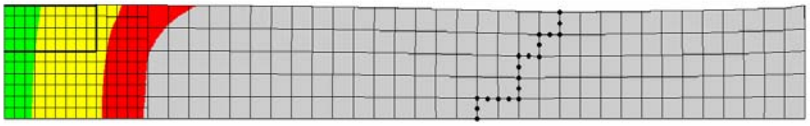

c) Strain contours of condition C

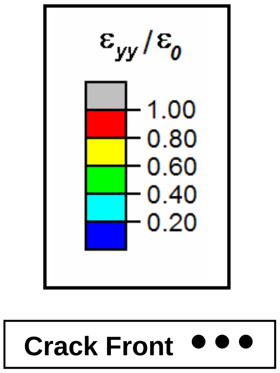

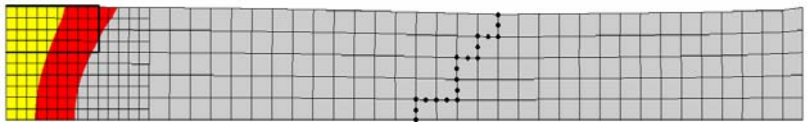

d) Strain contours of condition D

Figure 5.2 Load Ratio as a Function of Surface Crack Length and Evolution of Extensional Strain ε_{yy} for Architecture 1 condition A. From condition B to C, R_f increases, supporting approximately 55 percent of the total load, while the crack tunnelling magnitude increases only slightly. The amount of extensionally yielded base material ahead of the crack front has increased. At initial composite reinforcement failure, condition D, the reinforcement is carrying approximately 60 percent of the total load. Crack tunnelling magnitude is still the same as at condition C.

The continually increasing slope of the load ratio vs. crack length curve of Figure 5.2 is due to the gradients in the X-direction of extensional strain component ε_{yy} ahead of the crack tip. At condition A, the strains do not vary much in the X-direction in the reinforcement. However, as the load increases, because of the closeness of the contours near the yield strain contour, strain in the reinforcement increases more rapidly, thus the load in the reinforcement begins to increase more rapidly at condition B. From the perspective of the reinforcement, as the strains and strain gradients increase, the load in the reinforcement begins to increase faster due to these higher strains and strain gradients, as shown at condition C. The load in the reinforcement continues to increase in this way up to initial reinforcement failure at condition D.

It should be noted that since trends in the relation between R_f and crack length are similar for each architecture, plots of R_f as a function of surface crack growth are not shown for the remaining architectures. Also, since initial composite failure is the main point of interest, and this will coincide with maximum load, full evolution of the extensional yield strain contours as in Figures 5.2a) – d) will not be shown for subsequent architectures, and will be limited only to the condition of initial reinforcement failure.

Due to this important connection between R_f and the contours of extensional strain component, ε_{yy}, the nature of the dependence of the contours as a function of architecture is crucial. As more architectures are discussed, the actual connection between the load ratio and overall maximum load becomes apparent. In all subsequent extensional strain contour plots, the contour color bands are chosen such that the extensional failure strain of the composite reinforcement falls approximately at the center of the red contour band, as shown in Figure 5.3b). The dotted line in Figure 5.3b) indicates this strain contour. Once this contour reaches the composite reinforcement leading edge, the composite reinforcement element will fail. In addition, in subsequent figures, all extensional strain contour plots are shown at the same location within the specimen (parallel to the crack plane at $Y = 0$), and scaled to the same size, unless otherwise noted. The distance from the reinforcement leading edge to the left extreme is 0.25 inches.

Figure 3.19 of the unreinforced case is also re-shown and re-scaled in Figure 5.3a) for comparison. This figure shows that the reinforced architecture has a similarly shaped extensional strain contour, however, this strain contour is less curved in the thickness direction. This is due to local stiffening effects of the reinforcement. Because of local stiffening, increasingly larger pin displacements, and therefore larger loads, must be applied in order to reach the critical CTOA along the crack front. This is the reason why there is a continued increase in the load as the surface crack approaches the reinforcement. This also means that larger applied loads are required to achieve strain-based failure at the reinforcement's interior corner leading edge, where initial composite failure occurs. How this extensional failure strain contour changes through the thickness as it approaches the reinforcement leading edge is an important characteristic to note when comparing the different architectures.

Another important characteristic to pay attention to for each architecture is how quickly the extensional strains decrease within the reinforcement. This is similar to what occurs for the unreinforced case. Strain levels are relatively high within the plastic zone and for the first one to two plate thicknesses ahead of the plastic zone. However, due to the sharp decreasing strain gradient over these one to two plate thicknesses, strains become fairly low and the strain gradients are small.

For architecture 1, in the X-direction, the strain contours become approximately uniform through the thickness a short distance away from the reinforcement leading edge. The strains decrease quickly with distance from the reinforcement leading edge, as shown in Figure 5.3. At a distance equal to one-half of the total reinforcement width, the extensional strain is approximately 20 percent of the failure strain occurring at the leading edge. This means that some portion of the width of the reinforcement (which is not shown at this scale) is not being loaded in tension, and is actually in very slight compression.

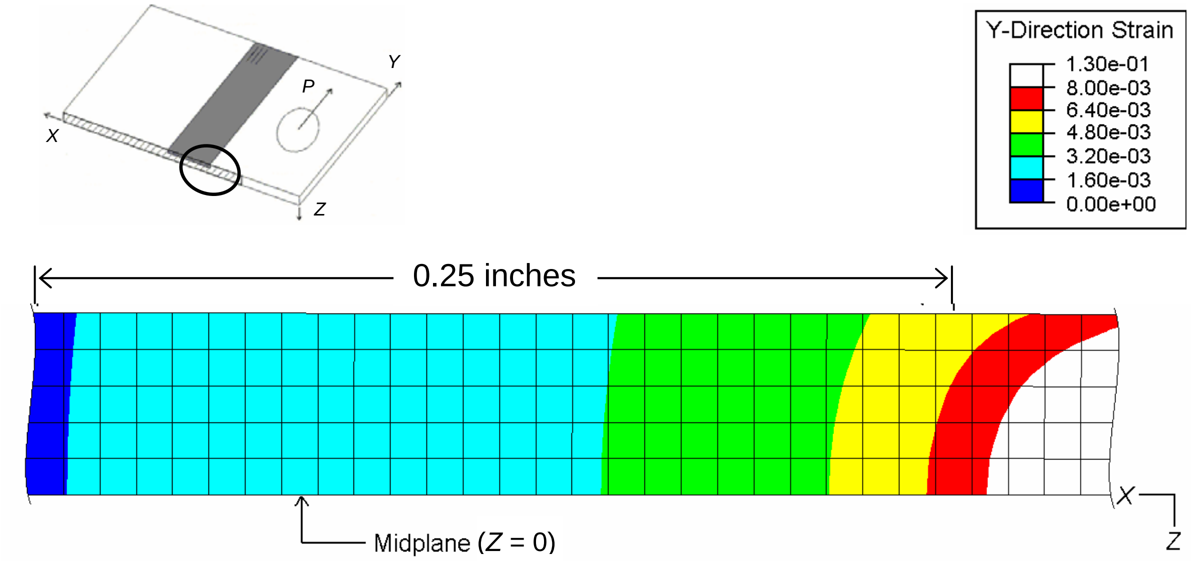

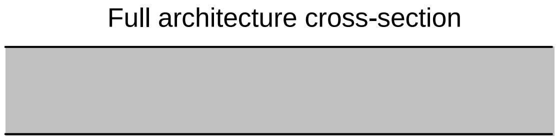

Parameter	Normalized Value
Load	1.000
Crack Length	1.000
R_f	N/A

a) Unreinforced

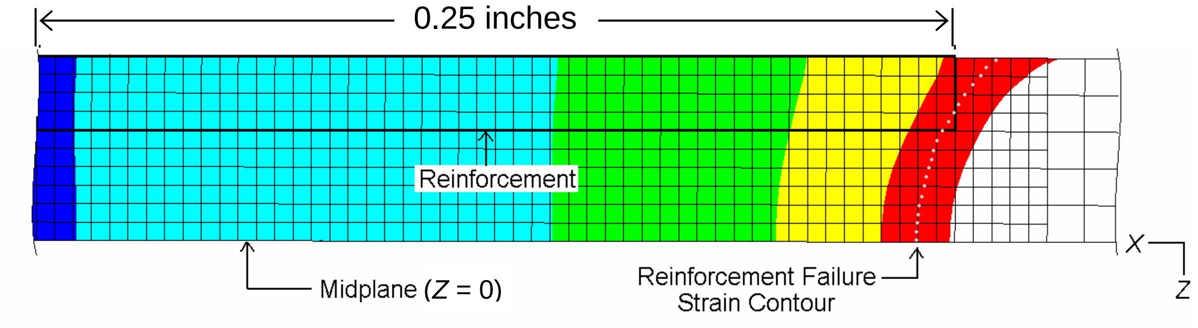

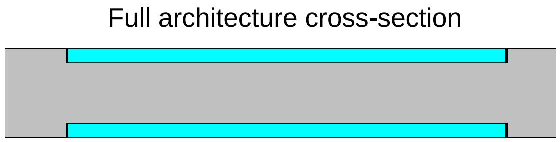

Parameter	Normalized Value
Load	1.172
Crack Length	0.813
R_f	0.603

b) Architecture 1

Figure 5.3 Contours of Extensional Strain ε_{yy} and Performance for Unreinforced and Architecture 1

For architecture 1, at initial composite fiber tensile failure, the load ratio, R_f, is equal to 0.603. The reinforcement is carrying about 60 percent of the total applied load of 2843 lbs. Normalizing this to the maximum load of the unreinforced case, the normalized maximum load for architecture 1 is 1.17. From Figure 5.3b), it is seen that the composite initially fails at the inner corner leading edge along the crack plane due to the shape of the "approaching" extensional strain due to increasing applied pin displacement. At maximum load, the surface crack length, normalized to the surface crack length at maximum load for the unreinforced case, is 0.813 (0.13 in). This means that the surface crack length at maximum load is only approximately 81 percent of the unreinforced case. This goes back to the previous discussion on the increasingly large plastic zone size of the crack tip, in that increasing applied loads, due to the inclusion of the reinforcement, further extends the plastic zone size. Also, as previously mentioned, surface crack length is only of secondary importance to maximum load.

Also shown in Figure 5.3, and as shown in subsequent contour plot comparisons, are tables summarizing the architecture performance. The maximum load and crack length at maximum load in these tables are both normalized to the maximum load and crack length at maximum load of the unreinforced case.

5.1.2 Architecture 2

The response curve for this architecture is given in Figure 5.4, along with the unreinforced case, and architecture 1. This is the comparison of location. There is little difference between the response curves of architecture 1 and architecture 2. Both have the same normalized maximum loads of 1.17 (2843 lbs), and normalized surface crack lengths at maximum load of 0.813 (0.13 in).

The extensional strain contour plots of architectures 1 and 2 are shown in Figure 5.5. Comparing these two architectures, the contours of architecture 2 are less curved through the thickness than the contours of architecture 1. The reinforcement creates an area of greater

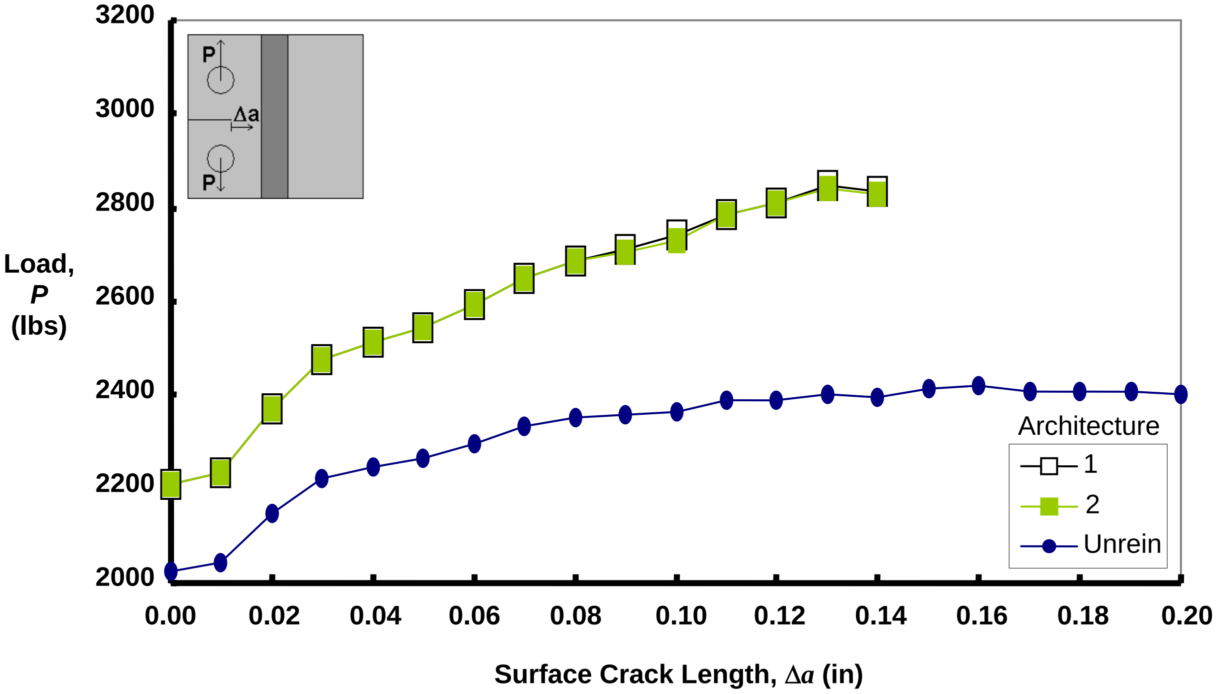

Figure 5.4 Load as a Function of Surface Crack Length for Architecture 1, Architecture 2, and Unreinforced

local stiffening at the midplane of the plate. Therefore, as the failure-producing extensional strain approaches, this failure surface flattens and initial reinforcement failure actually occurs on the outer corner of the reinforcement. R_f is only slightly higher due to involvement of more of the entire leading edge at initial failure (0.607 versus 0.603 for architecture 1). However, looking at the strain contour along the reinforcement width of architecture 2, the strains decrease at approximately the same rate in the X-direction as for architecture 1 at initial failure. Although at the leading edge slightly more reinforcement is straining in architecture 2, thus contributing to supporting the applied load, along the width the same amount of material is being strained at the same level, thus carrying the same amount of load along its width. The area of slightly higher strain at the leading edge of architecture 2 compared to architecture 1 is relatively small, given the overall reinforcement areas.

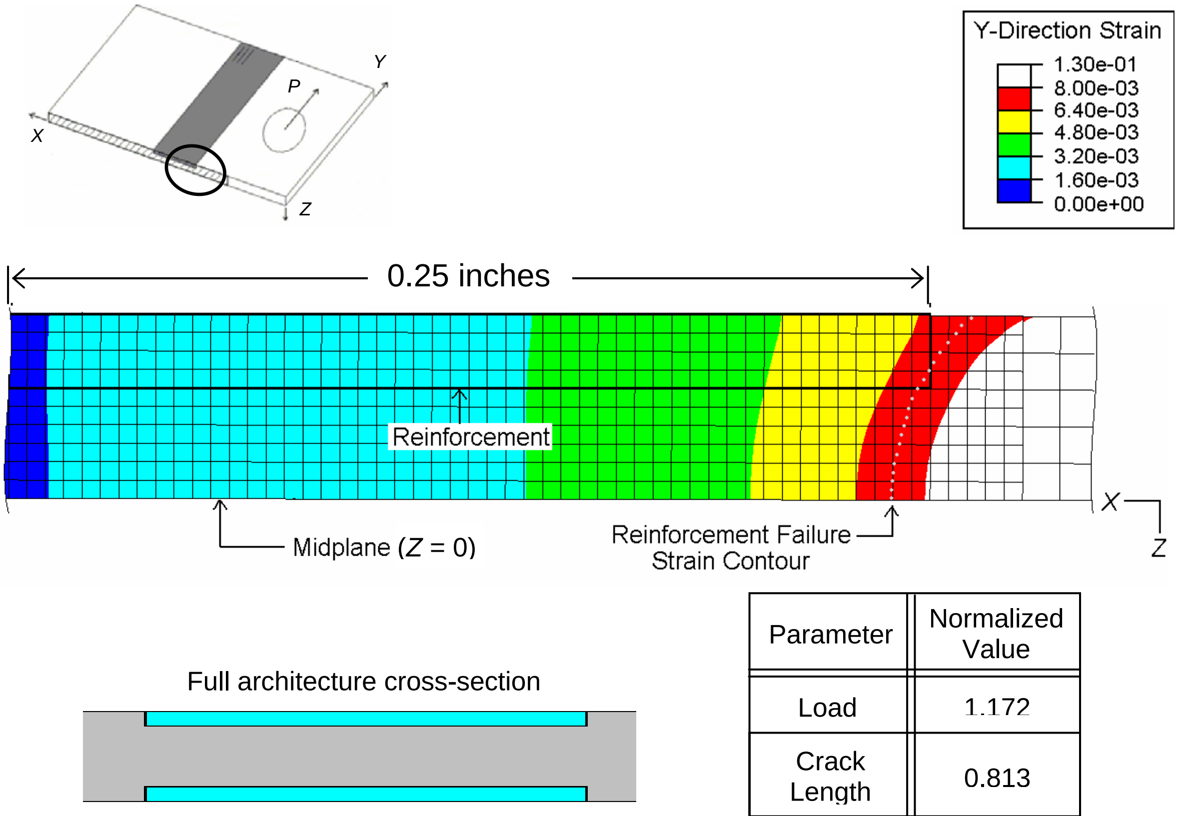

Parameter	Normalized Value
Load	1.172
Crack Length	0.813
R_f	0.603

a) Architecture 1

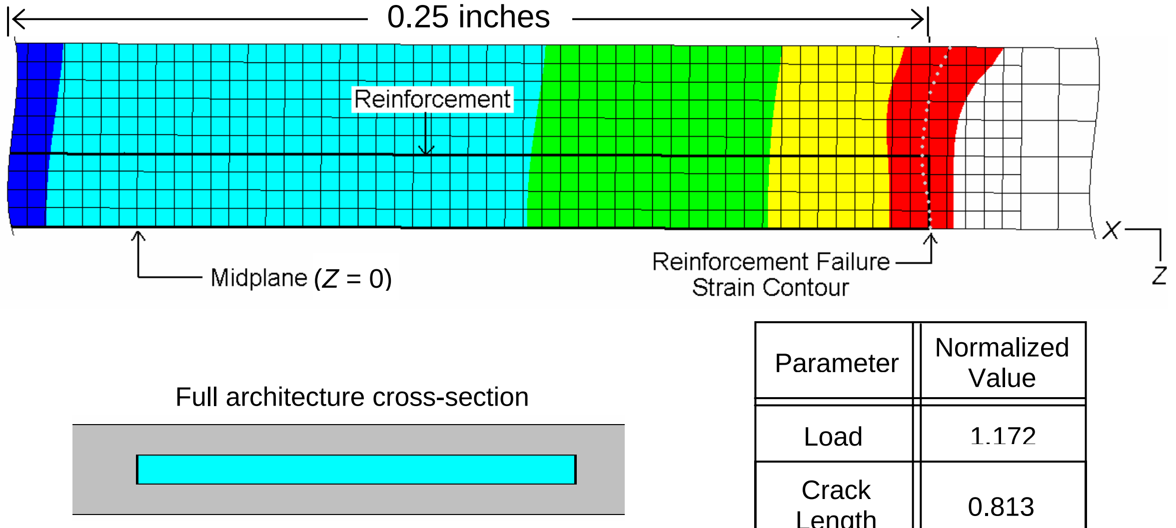

Parameter	Normalized Value
Load	1.172
Crack Length	0.813
R_f	0.607

b) Architecture 2

Figure 5.5 Contours of Extensional Strain ε_{yy} and Performance for Architecture 1 and Architecture 2

5.1.3 Architecture 3

The load as a function of crack length for architecture 3 is given in Figure 5.6, along with the response curves for architecture 2 and the unreinforced case for comparison. The maximum load at initial fiber direction tensile failure of the reinforcement (3102 lbs) is much higher than both the unreinforced case and architecture 2. The normalized maximum load for architecture 3 is 1.279. The normalized maximum crack length for this architecture is 0.938 (0.15 in). Therefore, comparing to architecture 2, for a reinforcement twice as thick, but half as wide, there is an approximately 9 percent increase in maximum load.

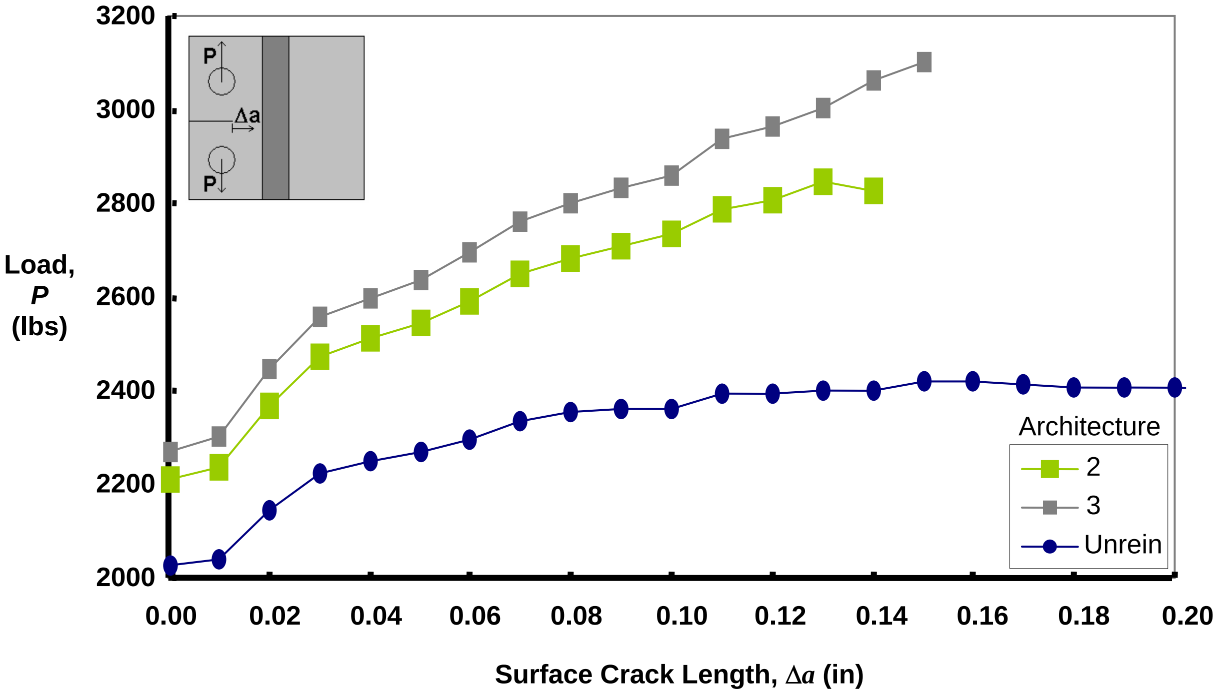

Figure 5.6 Load as a Function of Surface Crack Length for Architecture 2, Architecture 3, and Unreinforced

The extensional strain contours at initial reinforcement failure for architectures 2 and 3 are shown in Figure 5.7. The load ratio, R_f, for architecture 3 is 0.851, much higher than the 0.607 load ratio of architecture 2. For architecture 3, the extensional strain contours are nearly flat through the thickness, when compared to architecture 2. Initial failure occurs at the midplane, at the inside surface of the reinforcement leading edge. Since strain gradients through the thickness are not as high than along the width, because of this thicker

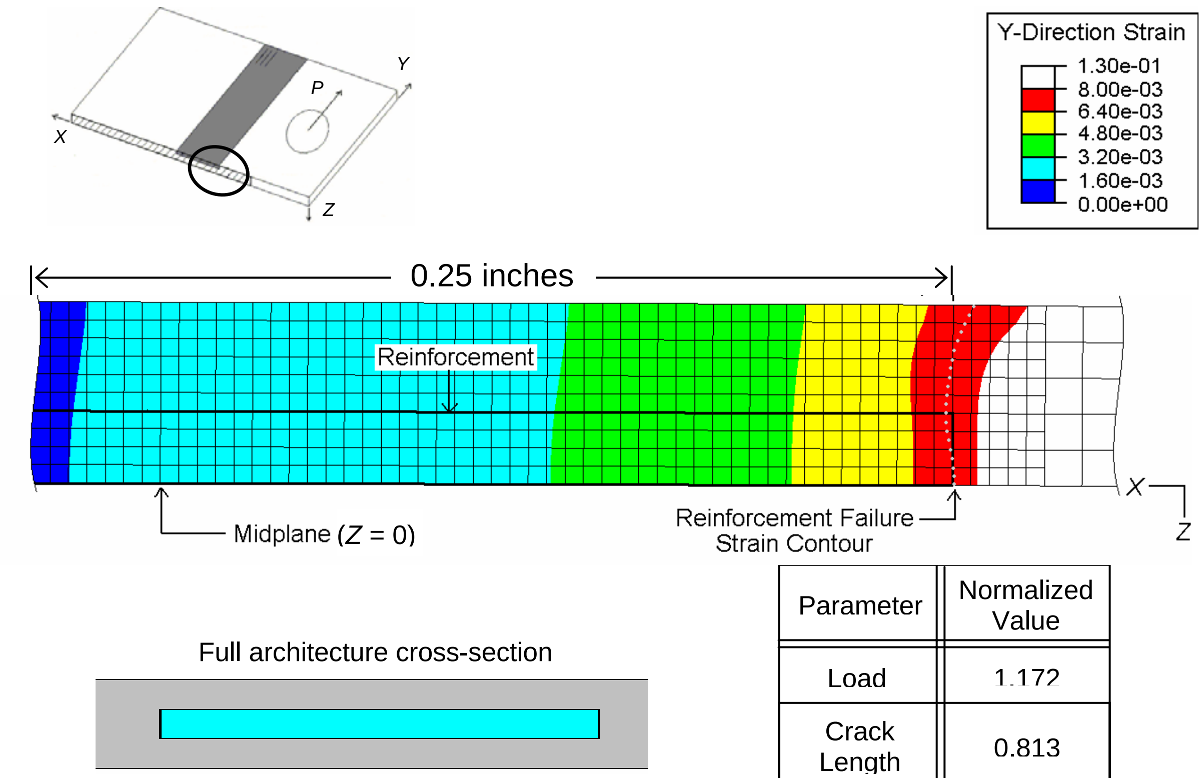

Parameter	Normalized Value
Load	1.172
Crack Length	0.813
R_f	0.607

a) Architecture 2

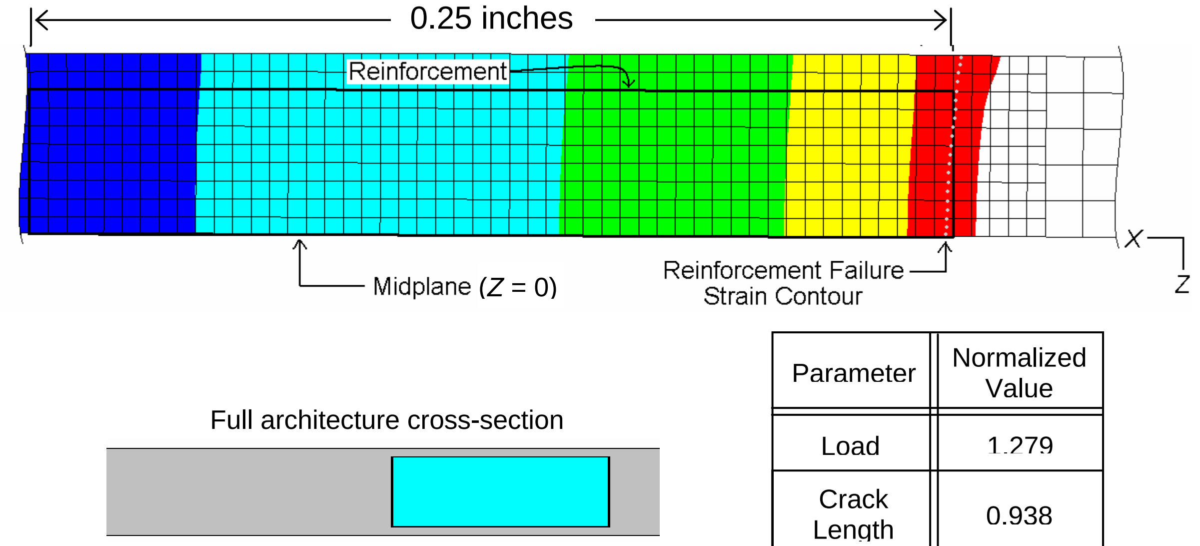

Parameter	Normalized Value
Load	1.279
Crack Length	0.938
R_f	0.851

b) Architecture 3

Figure 5.7 Contours of Extensional Strain ε_{yy} and Performance for Architecture 2 and Architecture 3 reinforcement, there is more reinforcement being involved at initial failure through the thickness due to this very flat incoming failure contour. Not only is more reinforcement involved in extensional straining through the thickness, more reinforcement is involved along the width as well. For architectures 1 and 2, only half of the reinforcement width is shown. However, for architecture 3, the entire width is shown. As shown in Figure 5.7, the strains along the reinforcement width decrease much quicker in the X-direction for architecture 3 than for architecture 2. This is due to more of the stiff reinforcement being involved, thus causing strains to decrease quicker along the X-direction. This also means that a larger percentage of reinforcement is at an overall higher strain level than in architecture 2, and thus more reinforcement along both the width and the thickness is supporting the total load, as the increased load ratio, R_f suggests.

5.1.4 Architecture 4

The load vs. crack length relation for architecture 4 is shown in Figure 5.8. Also shown are the curves for architecture 1 and the unreinforced case for comparison. The normalized maximum load is 1.183 for architecture 4, and the normalized crack length at maximum load is 0.875. This is 2868 lbs and 0.14 in, respectively. Compared to architecture 1, despite having a slightly lower cross-sectional area, rounding the leading edge results in a slightly higher maximum load, and surface crack length.

Extensional strain contours for architectures 4 and 1 are shown in Figure 5.9. R_f for architecture 4 is 0.618, while for architecture 1, 0.603. The strain contours through the thickness have approximately the same shape, however, more of the reinforcement leading edge of architecture 4 is near the failure strain at initial failure. Initial failure occurs approximately at the middle of the circumference of the quarter-circular leading edge for architecture 4, as opposed to failure at the sharp corner of architecture 1. Along with leading edge involvement, the strain contours are slightly shifted along the width of the

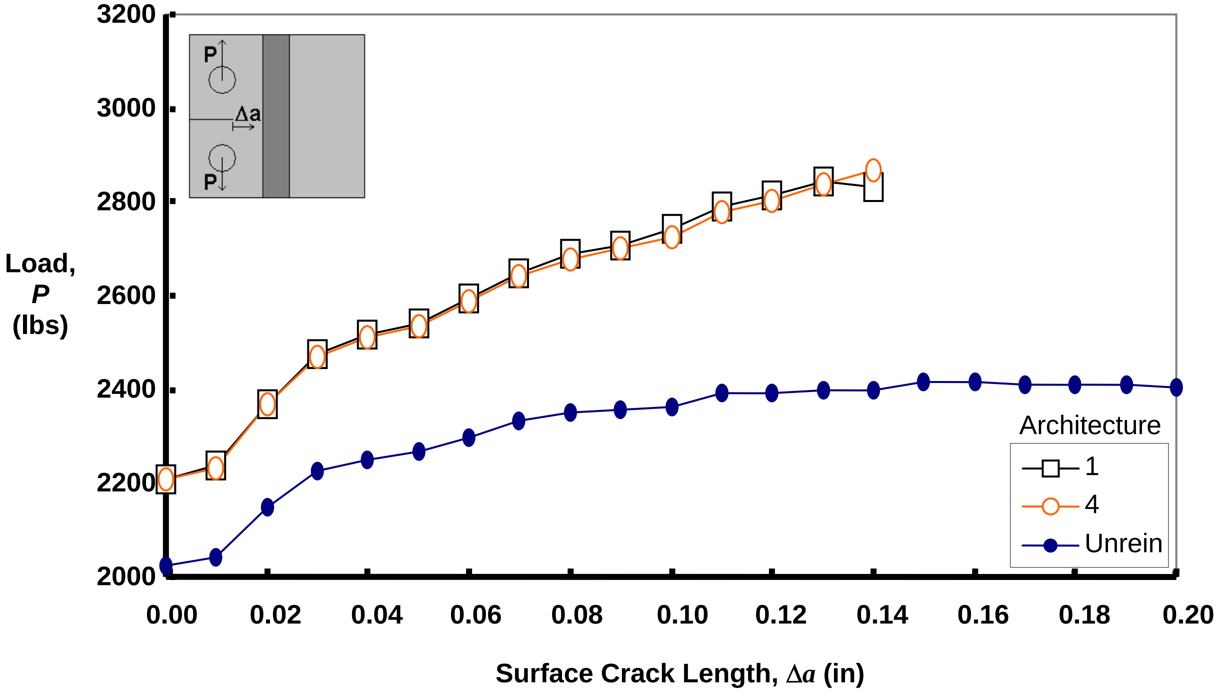

Figure 5.8 Load as a Function of Surface Crack Length for Architecture 1, Architecture 4, and Unreinforced

reinforcement compared to architecture 1. This means that more of the reinforcement along its width is at higher levels of strain, thus supporting more of the load. Because of the rounded leading edge, the failure extensional strain contour does not encounter the leading edge, until a slightly larger amount of surface crack length, when compared to architecture 1.

5.1.5 Architecture 5

The load as a function of surface crack length is shown in Figure 5.10 for architectures 2, 3, 5, and the unreinforced case. The normalized maximum load for architecture 5 is 1.167 (2830 lbs), and the normalized crack length is 0.875 (0.14 in). The maximum load for this case is lower than both architectures 2 and 3, however the maximum crack length falls between these two architectures.

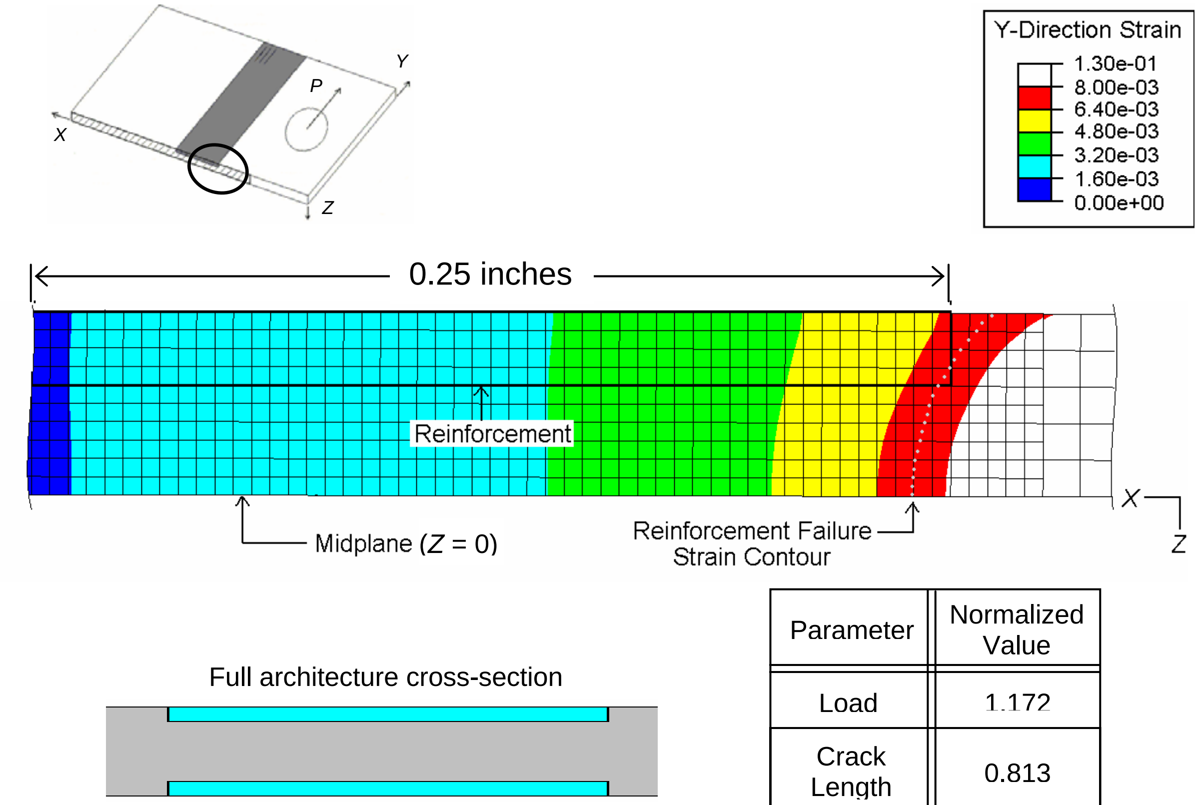

Parameter	Normalized Value
Load	1.172
Crack Length	0.813
R_f	0.603

a) Architecture 1

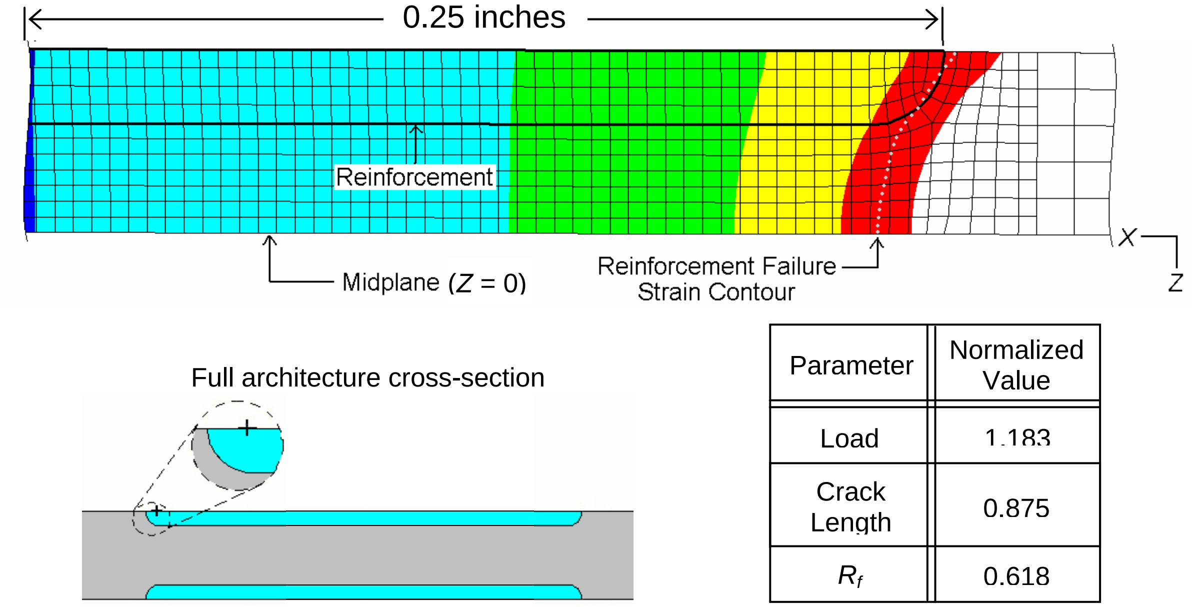

Parameter	Normalized Value
Load	1.183
Crack Length	0.875
R_f	0.618

b) Architecture 4

Figure 5.9 Contours of Extensional Strain ε_{yy} and Performance for Architecture 1 and Architecture 4

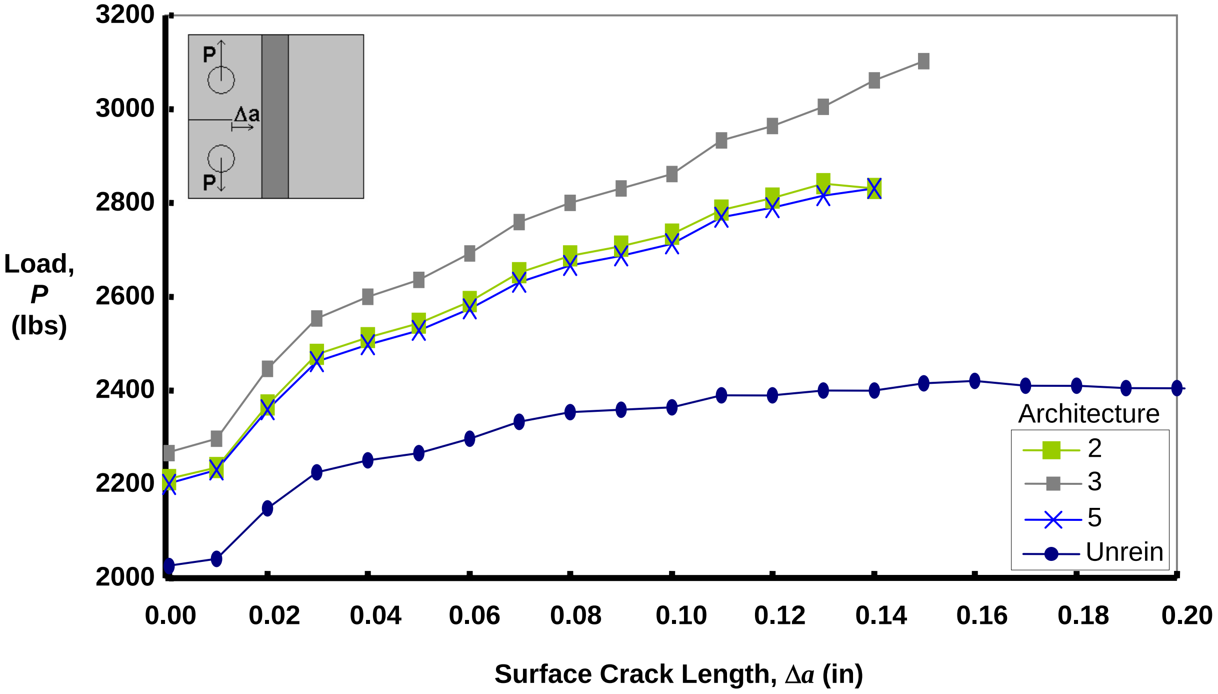

Figure 5.10 Load as a Function of Surface Crack Length for Architecture 2, Architecture 3, Architecture 5, and Unreinforced

Extensional strain contours are shown for architectures 2, 3, and 5 in Figure 5.11. The load ratio R_f for architecture 5 is 0.584. This is the total load of all discrete reinforcements summed. This is lower than both architectures 2 and 3. In this figure, although there are six discrete reinforcements total, only three are shown for scale. As shown in the figure, the strain contours are flatter through the thickness, similar to architecture 3. Initial failure occurs on the leading reinforcement's leading edge at the midplane, also similar to architecture 3. Although the thickness of the individual reinforcements is the same as the thickness of architecture 3, the maximum load is considerably lower. Along the width, the strain contours for architecture 5 are similar to architecture 2. This means that the reinforcements further down (the reinforcements not shown) are not significantly strained. Due to this fairly large distance between discrete

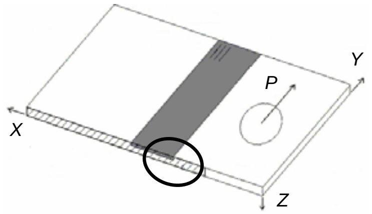

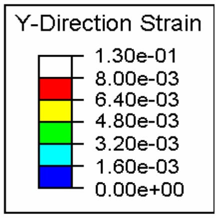

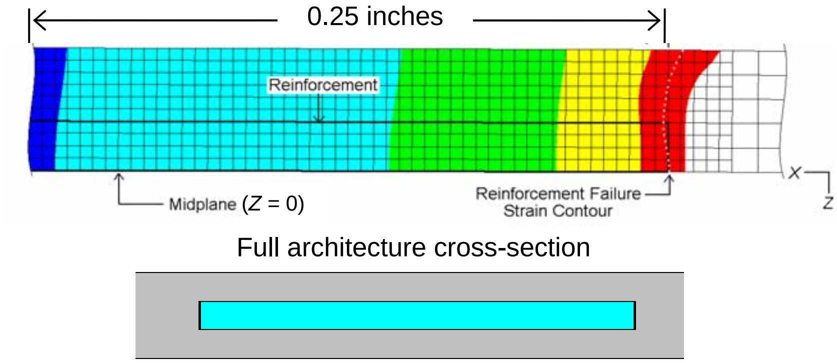

Parameter	Normalized Value
Load	1.172
Crack Length	0.813
R_f	0.607

a) Architecture 2

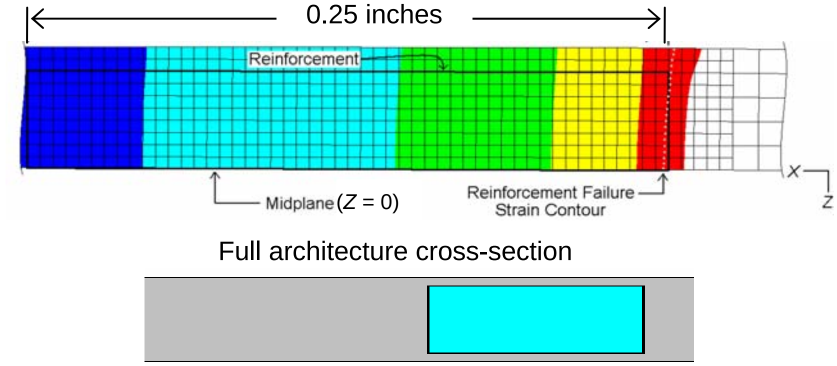

Parameter	Normalized Value
Load	1.279
Crack Length	0.938
R_f	0.851

b) Architecture 3

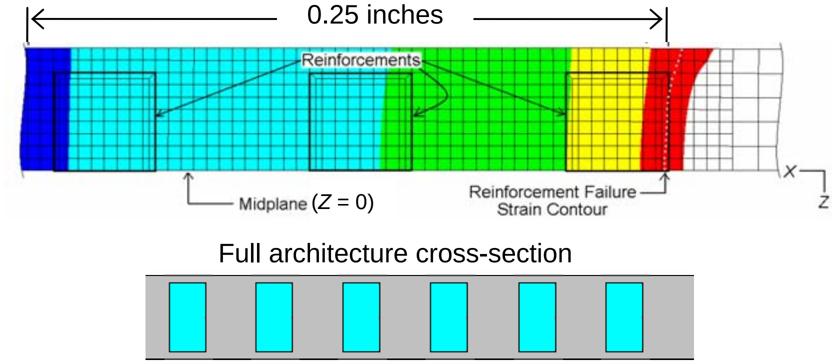

Parameter	Normalized Value
Load	1.167
Crack Length	0.875
R_f	0.584

c) Architecture 5

Figure 5.11 Contours of Extensional Strain ε_{yy} and Performance for Architecture 2, Architecture 3, and Architecture 5

reinforcements, these reinforcements are not contributing any load support at initial reinforcement failure. Since all these reinforcements are thicker than in architecture 2, the reinforcement segments at low strain comprise a fairly large total cross-sectional area that is not supporting load. Because of this, maximum load is lower.

Table 5.1 summarizes the performance of all of the rectangular reinforcements at initial failure, including normalized maximum load, normalized surface crack length at maximum load, and load ratio.

Table 5.1 Summary of Results: Rectangular Reinforcement Architectures

Architecture Number	Maximum Load (lbs)	Normalized Surface Crack Length at Max Load (in)	Normalized Max Load to Unreinforced Case	Load Ratio, R_f
0 (Unreinforced)	2425	1	1	N/A
1	2845	0.813	1.173	0.603
2	2843	0.813	1.172	0.607
3	3102	0.938	1.279	0.851
4	2868	0.875	1.183	0.618
5	2830	0.875	1.167	0.584

As shown in Table 5.1, and more clearly in Figure 5.12, R_f seems to follow the trend of maximum load. This supports the idea from Farley et al. [12] that load sharing is the main mechanism of load increase in in-situ selectively reinforced metals. The strain contours coincide with the idea that the more reinforcement that is involved in strain and high levels of strain, the more load that is transferred to the reinforcement, therefore higher maximum loads.

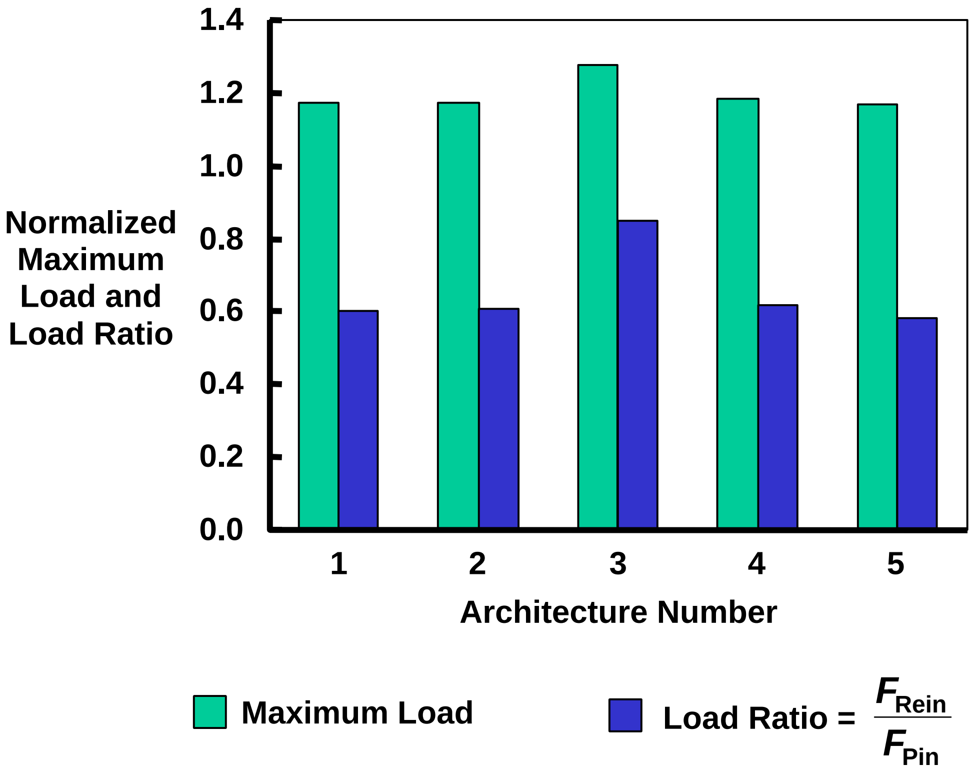

Figure 5.12 Bar Chart Comparison of Maximum Loads and R_f for Rectangular Architectures

The results of all of the rectangular reinforcement architectures have been discussed. As initially mentioned, the results of the triangular reinforcement architectures are described next.

5.2 Triangular Reinforcement Architectures

The remaining architectures are considered triangular. The contour plot perspectives, contour plot scaling, load vs. surface crack length curve scaling, and load ratio calculations are still similar to those from the rectangular reinforcement architectures. As previously stated, the overall width and maximum thickness of each of the triangular architectures are the same.

5.2.1 Architecture 6

The response curve of load as a function of surface crack length for architectures 6 and 1, and the unreinforced case are shown in Figure 5.13. The normalized maximum load for architecture 6 is 1.154, which is slightly lower than architecture 1 of 1.172. The normalized maximum crack length is 0.875, which is slightly longer than that of architecture 1 of 0.813.

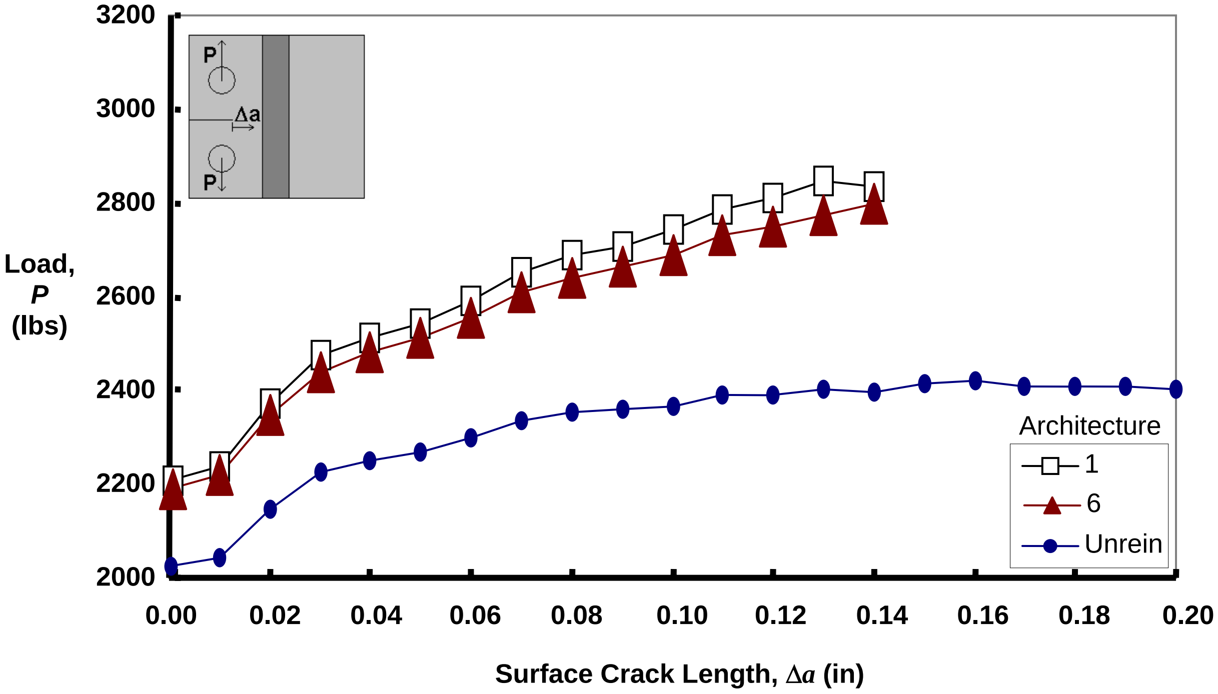

Figure 5.13 Load as a Function of Surface Crack Length for Architecture 1, Architecture 6, and Unreinforced

The extensional strain contour plot for architecture 1 and architecture 6 is shown in Figure 5.14. The load ratio for architecture 6 is 0.577, which is slightly lower than architecture 1. The failure strain contours are almost identical, yet slightly shifted along the crack propagation direction for architecture 6. The amount of this shift is approximately equal to the additional amount of surface crack extension. Failure occurs at the sharp leading edge, as opposed to the inner corner of architecture 1. Due to the sharp leading edge, there is basically no reinforcement through the thickness at the sharp leading edge. Because of this, only the first leading edge elements at the reinforcement tip are resisting the highest amount

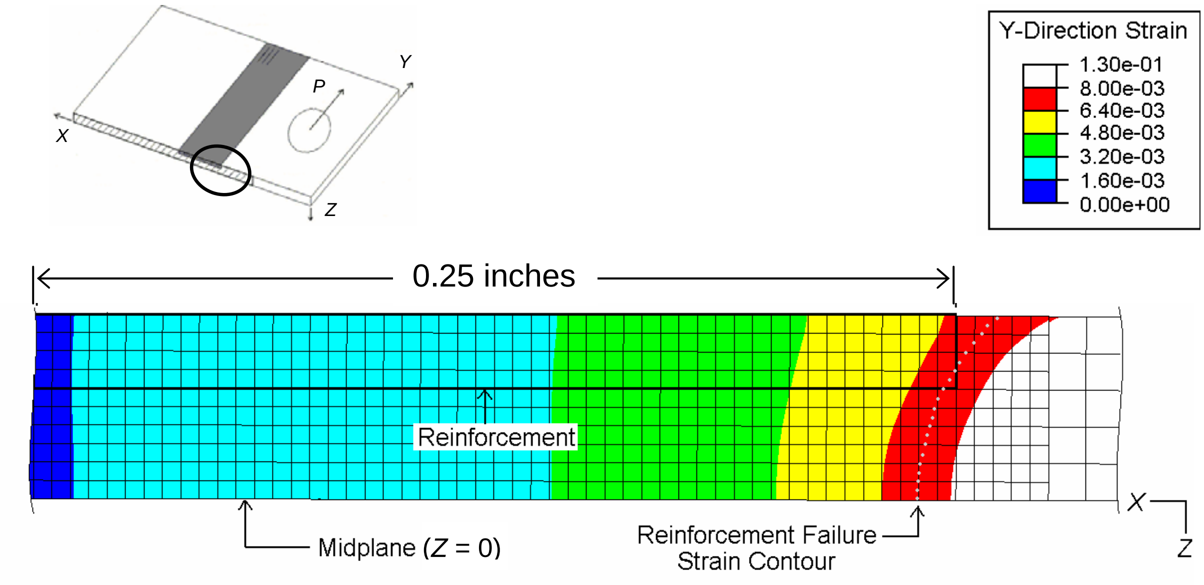

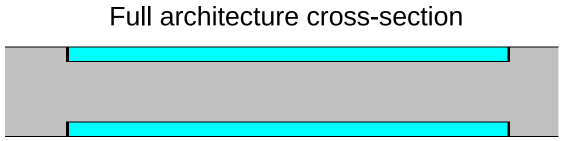

Parameter	Normalized Value
Load	1.172
Crack Length	0.813
R_f	0.603

a) Architecture 1

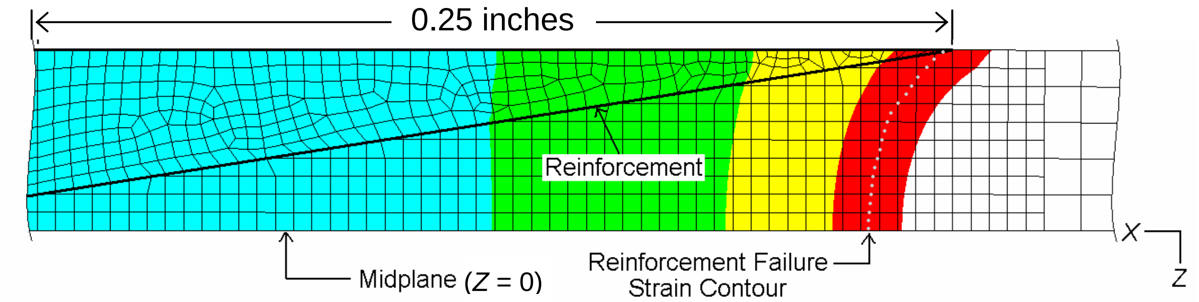

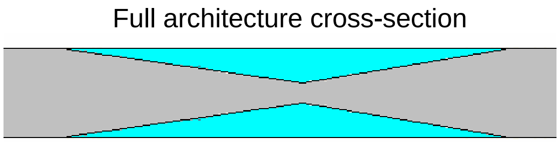

Parameter	Normalized Value
Load	1.154
Crack Length	0.875
R_f	0.577

b) Architecture 6

Figure 5.14 Contours of Extensional Strain ε_{yy} and Performance for Architecture 1 and Architecture 6

of reinforcement strain. Compared to architecture 1, there is a considerably larger reinforcement area at the reinforcement leading edge that is close to the failure strain (i.e., reinforcement area in red). However, in architecture 6, there is a much smaller area near the failure strain. Due to this lack of load support at the highly strained leading edge, the normalized maximum load is not as high as in architecture 6, and not as much load is being transferred to the reinforcement, as the lower R_f suggests. Also, although architecture 6 does eventually reach the same thickness as architecture 1, it is not until about one-quarter of the width from the leading edge. At this point, the strains are already relatively low, thus the remaining thicker reinforcement is being strained, but at a much lower level than right at the sharp tip. This phenomenon is common to most triangular reinforcement architectures.

One very important thing to note about this specific architecture is that the composite reinforcement fails at approximately 0.04 inches up in the Y-direction from the crack plane. In all other architectures, failure occurs along the crack plane. This is a specific case in which the reinforcement fails along the 45-degree band of maximum strain through the thickness, described in Section 3.3.6, in Figure 3.20. Due to the surface location of the reinforcement and the sharp leading edge, maximum failure strain is reached along these maximum strain bands on the surface, rather than close to the midplane. To keep a consistent scale, Figure 5.14 still shows the contours along the crack plane, as the strain at the leading edge element on this plane is still extremely close to the failure strain. There was also very little difference between the strain contours along the crack plane, and the contours along the failure surface.

5.2.2 Architecture 7

The load vs. surface crack length response curve for architecture 7 is shown in Figure 5.15, along with architecture 6 and the unreinforced case for comparison. The normalized maximum load for this case is 1.133, which is even lower than the normalized maximum load for architecture 6, which is 1.154. The normalized crack growth for architecture 7 is also lower at 0.750.

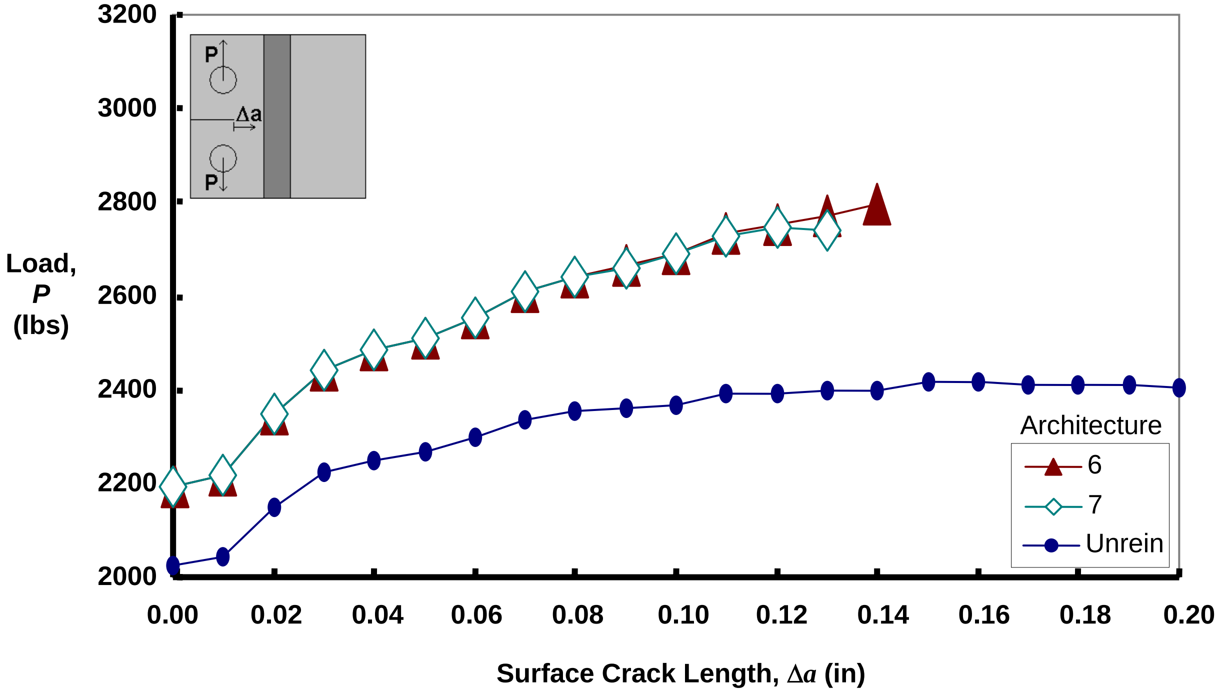

Figure 5.15 Load as a Function of Surface Crack Length for Architecture 1, Architecture 6, and Unreinforced

The extensional strain contours for architectures 6 and 7 are shown in Figure 5.16. The general shape of the failure strain contours through the thickness for both architectures are similar. As previously mentioned, due to a lack of local stiffness in the direction through the thickness at the sharp leading edge, there is not enough reinforcement material local to the leading edge to alter the strain contours through the thickness. Failure initiates at the sharp leading edge, and even less reinforcement is near the failure strain than in architecture 6, due to the shape of the nonlinear incoming failure strain contour. This is one factor that decreases the load that the reinforcement supports, with a relatively lower R_f of 0.534, as well as the decreased surface crack length. The strains along the width of the reinforcement also die out quicker for architecture 7 compared to architecture 6. Similar to the previous architectures, the lower the strain levels and the less material that is strained along the width, the less load potential the structure has, as the lower R_f suggests.

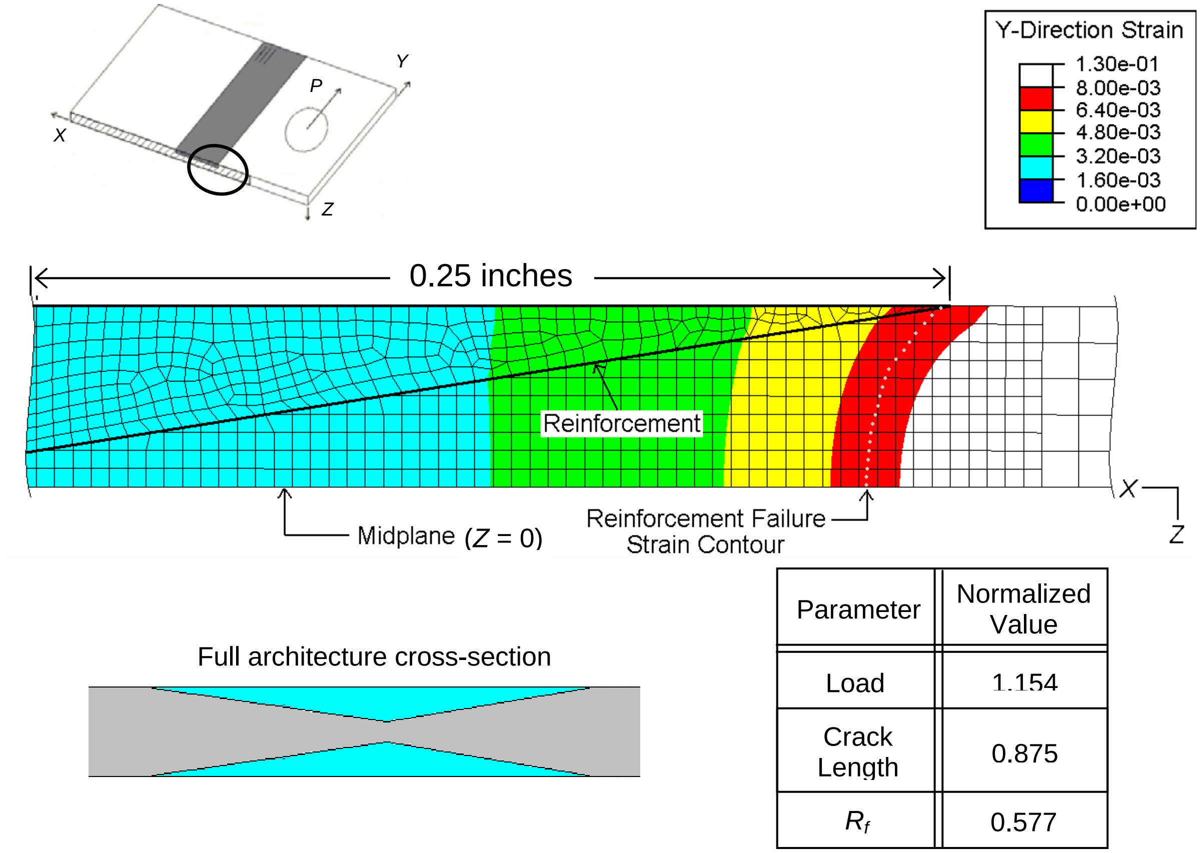

Parameter	Normalized Value
Load	1.154
Crack Length	0.875
R_f	0.577

a) Architecture 6

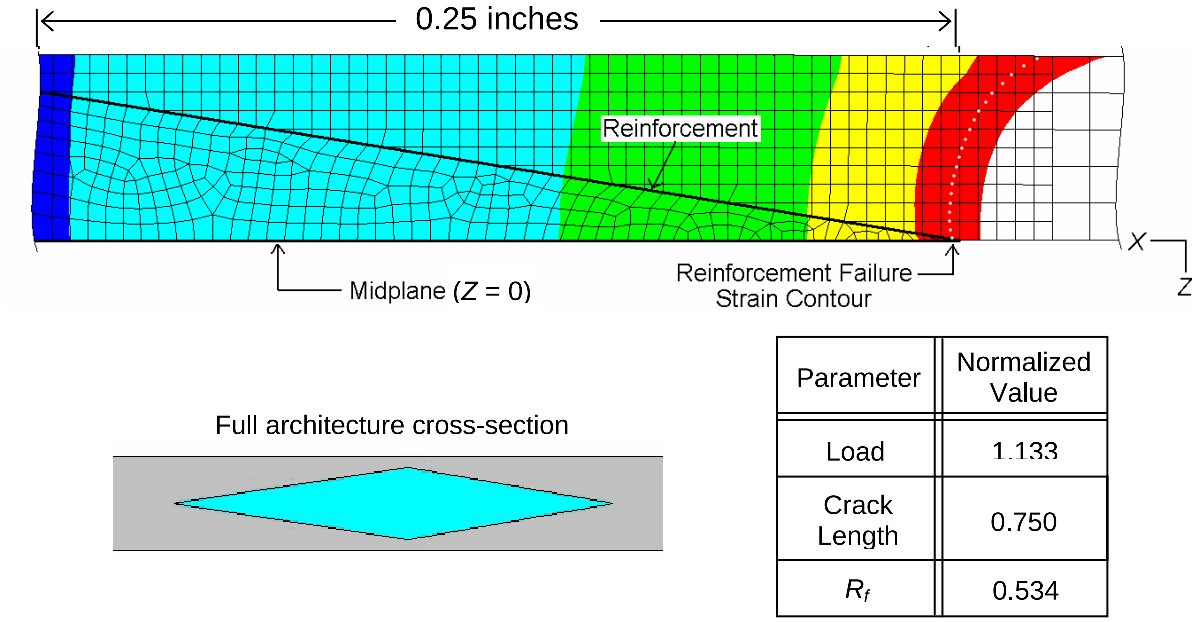

Parameter	Normalized Value
Load	1.133
Crack Length	0.750
R_f	0.534

b) Architecture 7

Figure 5.16 Contours of Extensional Strain ε_{yy} and Performance for Architecture 1 and Architecture 6

As mentioned in the Case Studies chapter, along with the unidirectional composite, other aluminum alloys will be applied within the reinforcement architecture cross-section. The remaining architectures all have different aluminum alloys applied at the sharp leading edge of the reinforcement.

5.2.3 Architecture 8

The load as a function of crack length for architecture 8, along with architecture 7 and the unreinforced case, are shown in Figure 5.17. Both the normalized maximum load and the normalized surface crack length for architecture 8 (1.149 and 0.875, respectively) are slightly higher than for architecture 7.

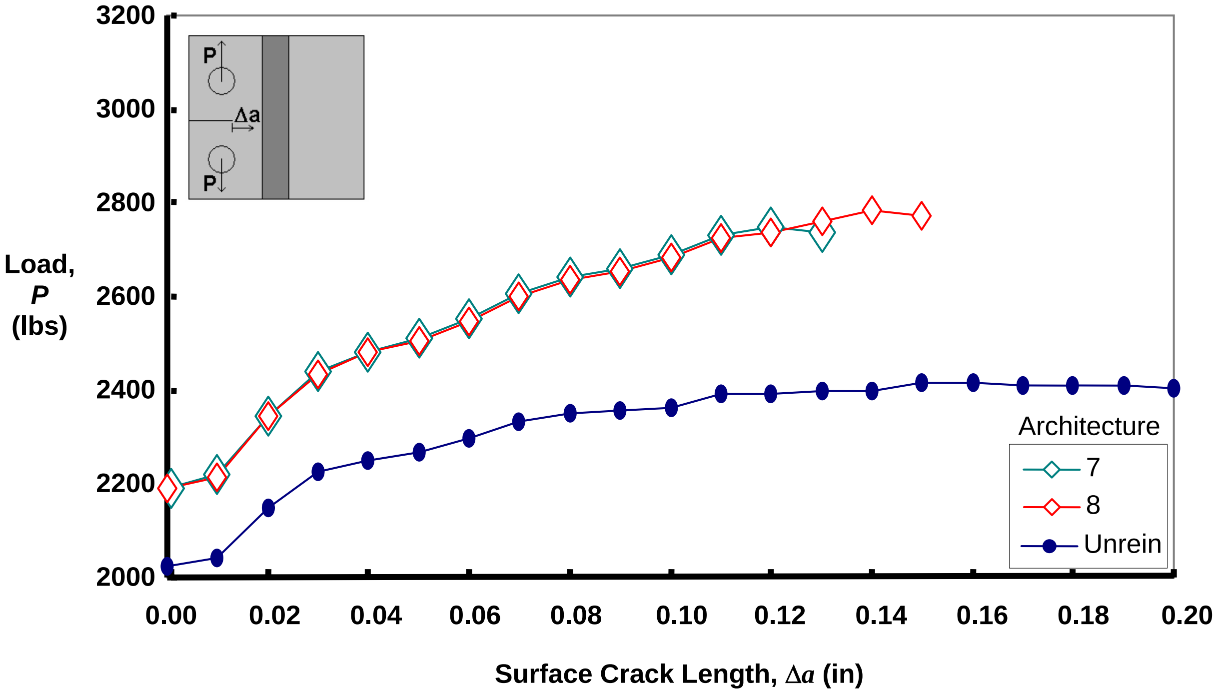

Figure 5.17 Load as a Function of Surface Crack Length for Architecture 7, Architecture 8, and Unreinforced

The extensional strain contours show a slight flattening of the composite failure strain contour, as shown in Figure 5.18. Failure essentially occurs over the short, flat leading edge of the composite reinforcement, right after the 1100 aluminum tip. The load ratio for architecture 8 is also slightly higher at 0.581, compared to architecture 7. This flattening

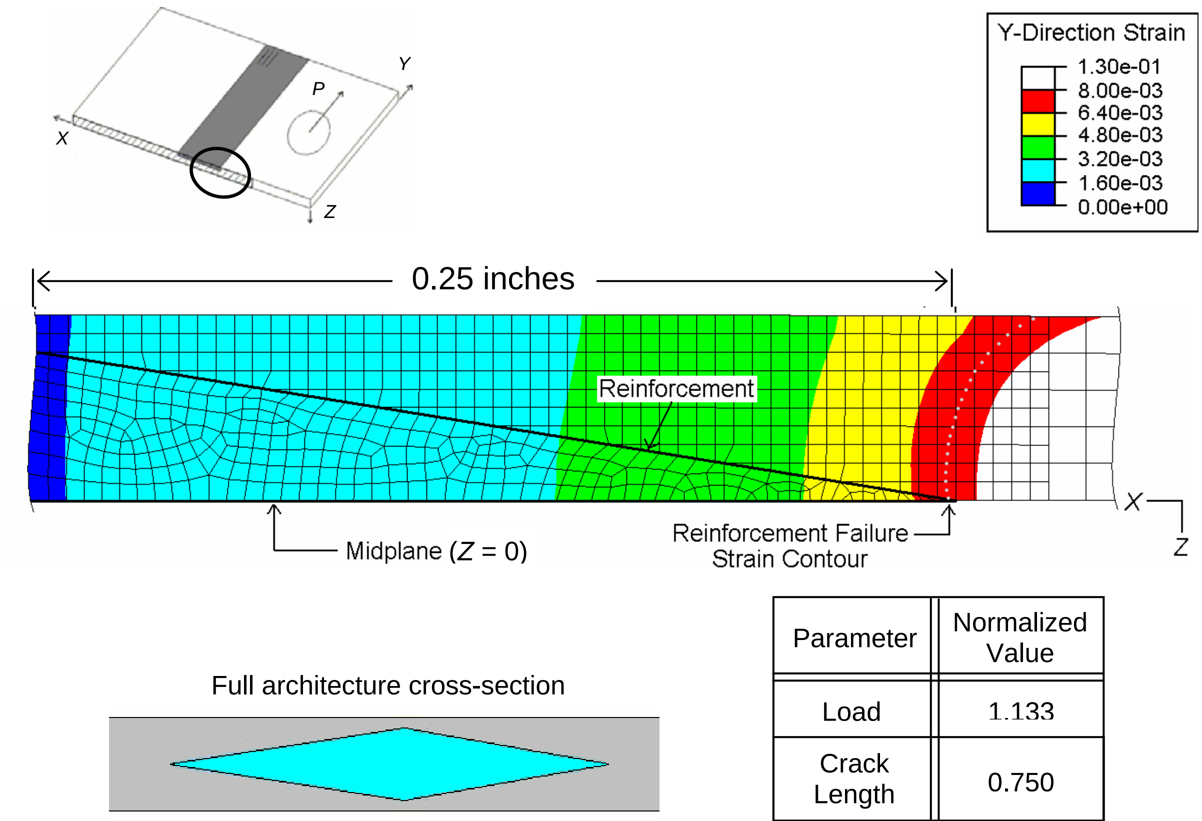

Parameter	Normalized Value
Load	1.133
Crack Length	0.750
R_f	0.534

a) Architecture 7

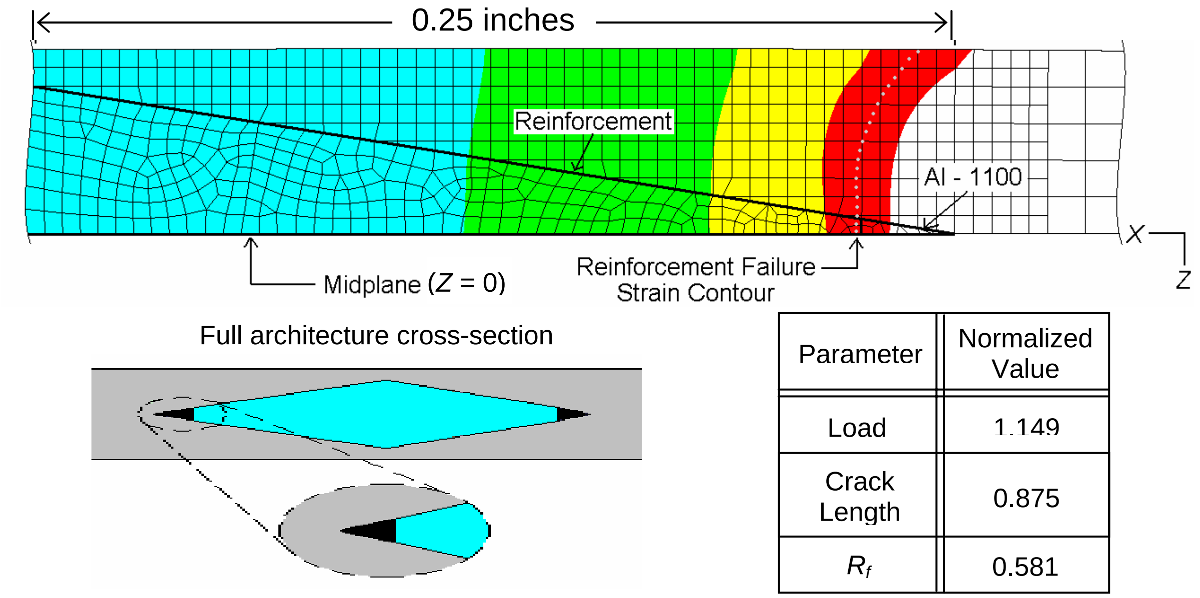

Parameter	Normalized Value
Load	1.149
Crack Length	0.875
R_f	0.581

b) Architecture 8

Figure 5.18 Contours of Extensional Strain ε_{yy} and Performance for Architecture 7 and Architecture 8

occurs due to the essentially straight leading edge of the composite. Although there is only a very small flat leading edge, more material is still being strained to near failure through the thickness, giving rise to a larger maximum load and measured R_f. Also, the amount of 1100 aluminum in the crack propagation direction is essentially equal to the amount of increased surface crack length. The failure strain of the 1100 aluminum is never reached. Along the reinforcement width, more material is being strained in tension. As seen in Figure 5.18, for a given strain level (i.e., color contour band), architecture 8 has a larger reinforcement area at a particular strain level through the thickness. Therefore, more of the composite reinforcement is supporting the total applied load, as the increased measured R_f suggests.

5.2.4 Architecture 9

The load vs. crack length curves for architectures 9, 8, and the unreinforced case are shown in Figure 5.19. The normalized surface crack lengths are the same (0.875), and the

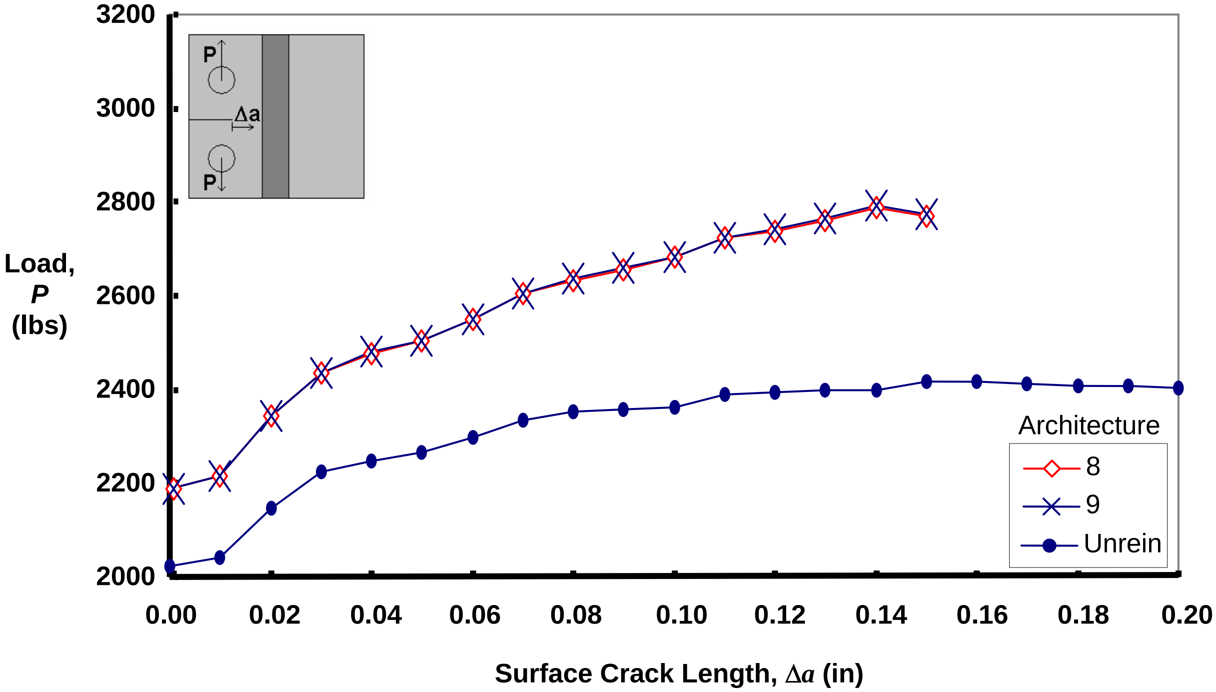

Figure 5.19 Load as a Function of Surface Crack Length for Architecture 8, Architecture 9, and Unreinforced

normalized maximum loads are also very similar. However, architecture 9 does exhibit a very slightly higher maximum load of 1.151.

The extensional strain contour plots are essentially the same both through the thickness and along the reinforcement width along the X-direction for both architectures 8 and 9, as shown in Figure 5.20. The load ratios are also the same at 0.581. The reason for the very slightly higher normalized maximum load is the stiffer Al-Li alloy at the tip of architecture 9 versus the 1100-Al tip of architecture 8. Keep in mind that this is a very small amount of aluminum at the reinforcement tip (less than 1 percent of total reinforcement cross-sectional area). The failure strain of the Al-Li is never reached.

5.2.5 Architecture 10

The load as a function of crack length response curves for this architecture are shown in Figure 5.21, along with architecture 8 and the unreinforced case. The normalized maximum load of 1.160 is larger for architecture 10 than the normalized maximum load of 1.149 for architecture 8. The normalized maximum crack length of 1.063 is also larger than even the unreinforced case.

The extensional strain contour plots for architectures 8 and 10 are shown in Figure 5.22. As depicted in the figure, initial reinforcement failure actually occurs at the leading edge, outer corner, similar to the inner rectangular case of architecture 2. The load ratio for architecture 10 (0.639) is also larger than architecture 8 (0.581). The failure strain contour for architecture 10 is significantly flatter than architecture 8, involving more of the entire leading edge close to the failure strain, thus raising the amount of load transfer, as R_f shows. Similar to the comparison between architectures 7 and 8, the additional amount of surface crack length is approximately equal to the added length of the 1100 aluminum tip. Again, the failure strain of the 1100 aluminum is never reached. Also, along the reinforcement width along the X-direction, more of the reinforcement of architecture 10 is strained due to

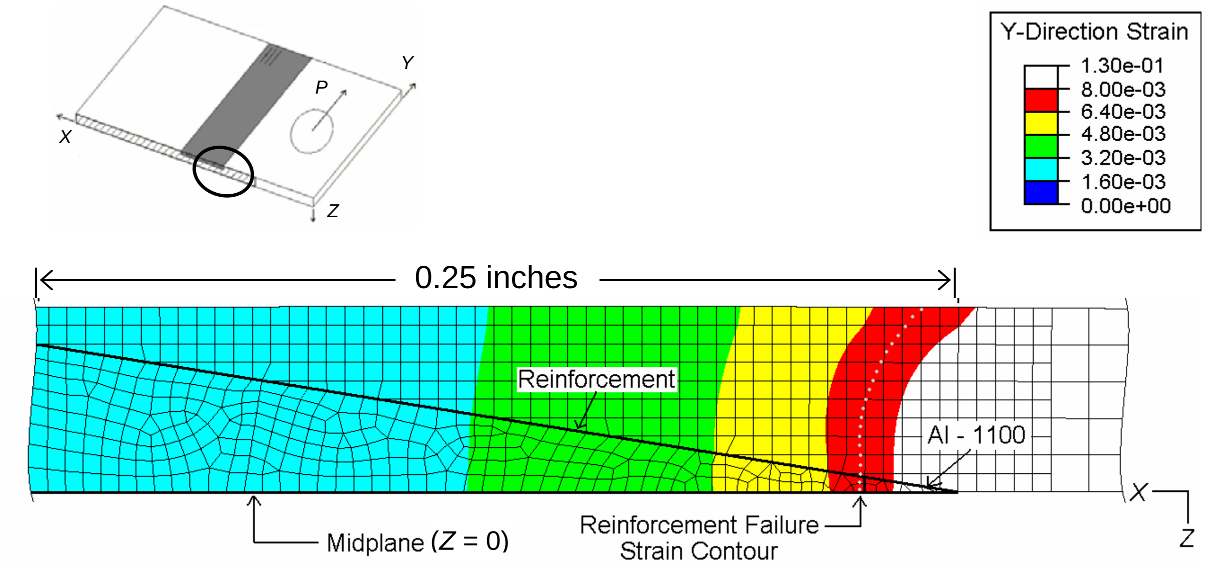

Full architecture cross-section

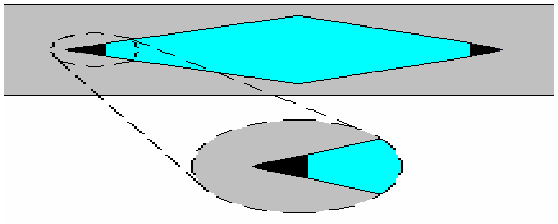

Parameter	Normalized Value
Load	1.149
Crack Length	0.875
R_f	0.581

a) Architecture 8

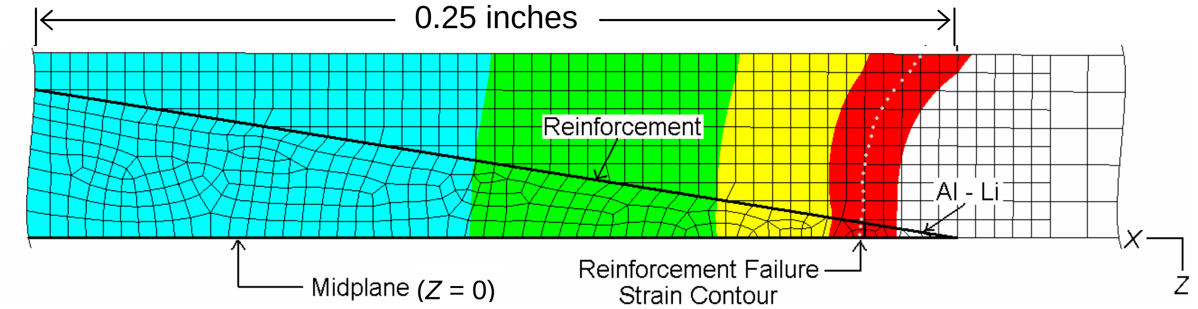

Full architecture cross-section

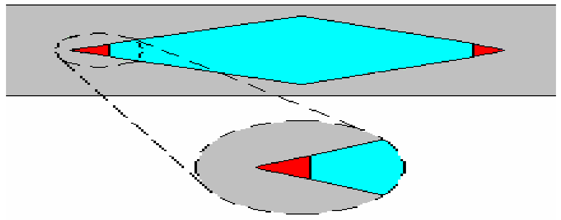

Parameter	Normalized Value
Load	1.151
Crack Length	0.875
R_f	0.581

b) Architecture 9

Figure 5.20 Contours of Extensional Strain ε_{yy} and Performance for Architecture 8 and Architecture 9

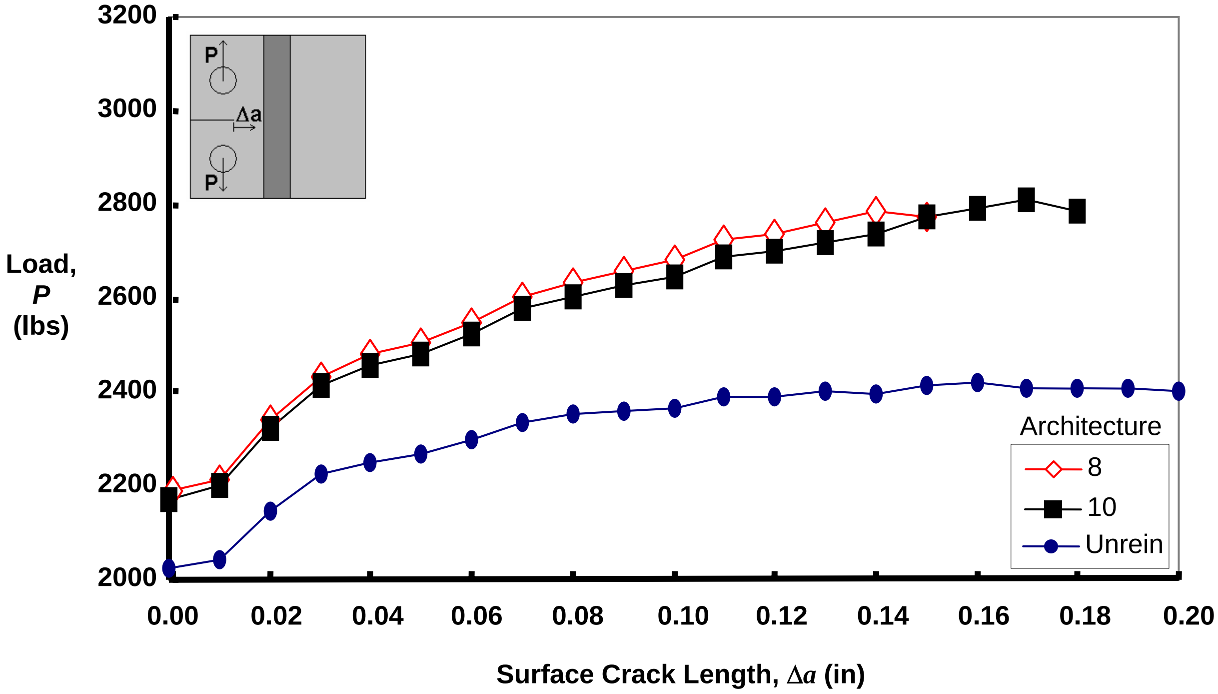

Figure 5.21 Load as a Function of Surface Crack Length for Architecture 8, Architecture 10, and Unreinforced

reinforcement thickening, thus carrying more load along the width than architecture 8. Similar to the comparison between architectures 7 and 8, even more reinforcement cross-sectional area is involved at a given strain level, increasing the load carried by the reinforcement, as the higher R_f suggests, thus a higher maximum load.

5.2.6 Architecture 11

The fracture response curves for architecture 6, architecture 11, and the unreinforced case are shown in Figure 5.23. Both the normalized maximum load (1.163) and normalized crack length (0.938) of architecture 11 are greater than those of architecture 6.

As shown in Figure 5.24, the extensional strain contours between architecture 6 and architecture 11 are similar, however the contours are shifted along the *X*-direction, similar to

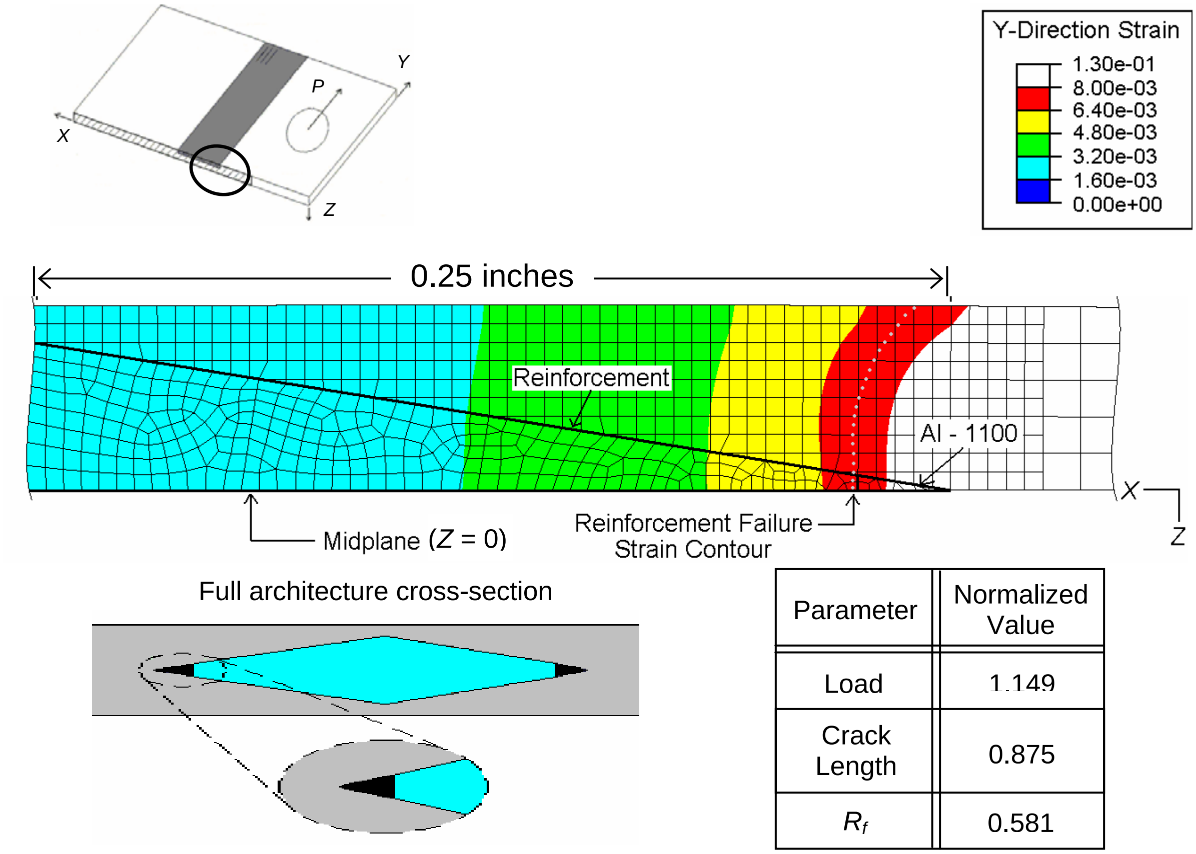

Parameter	Normalized Value
Load	1.149
Crack Length	0.875
R_f	0.581

a) Architecture 8

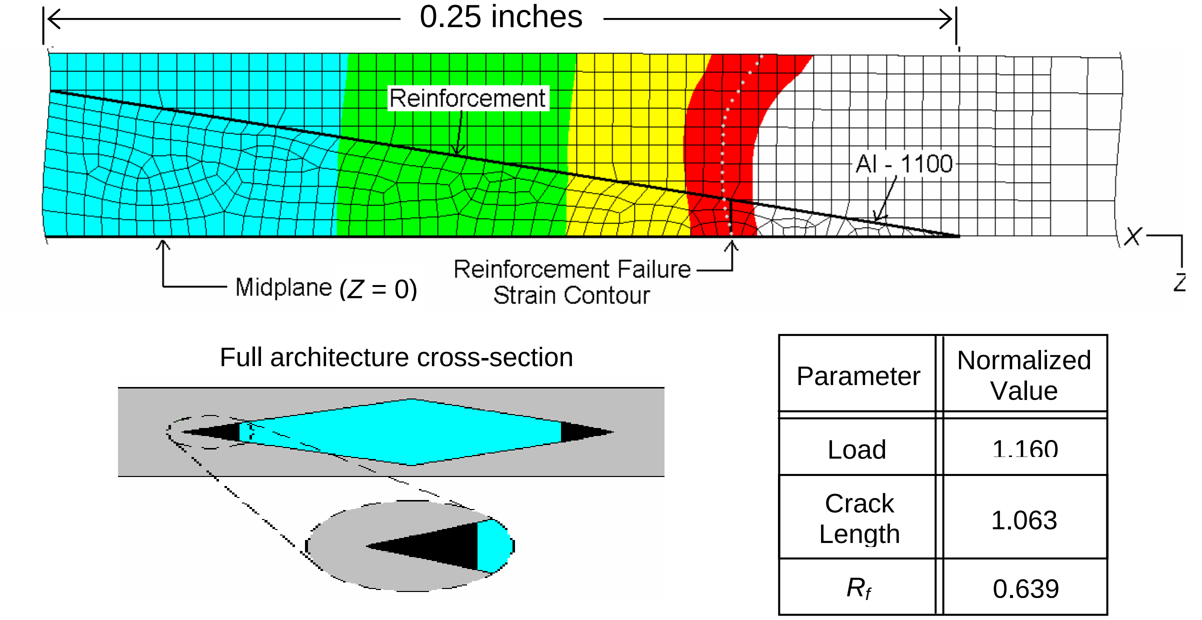

Parameter	Normalized Value
Load	1.160
Crack Length	1.063
R_f	0.639

b) Architecture 10

Figure 5.22 Contours of Extensional Strain ε_{yy} and Performance for Architecture 8 and Architecture 10

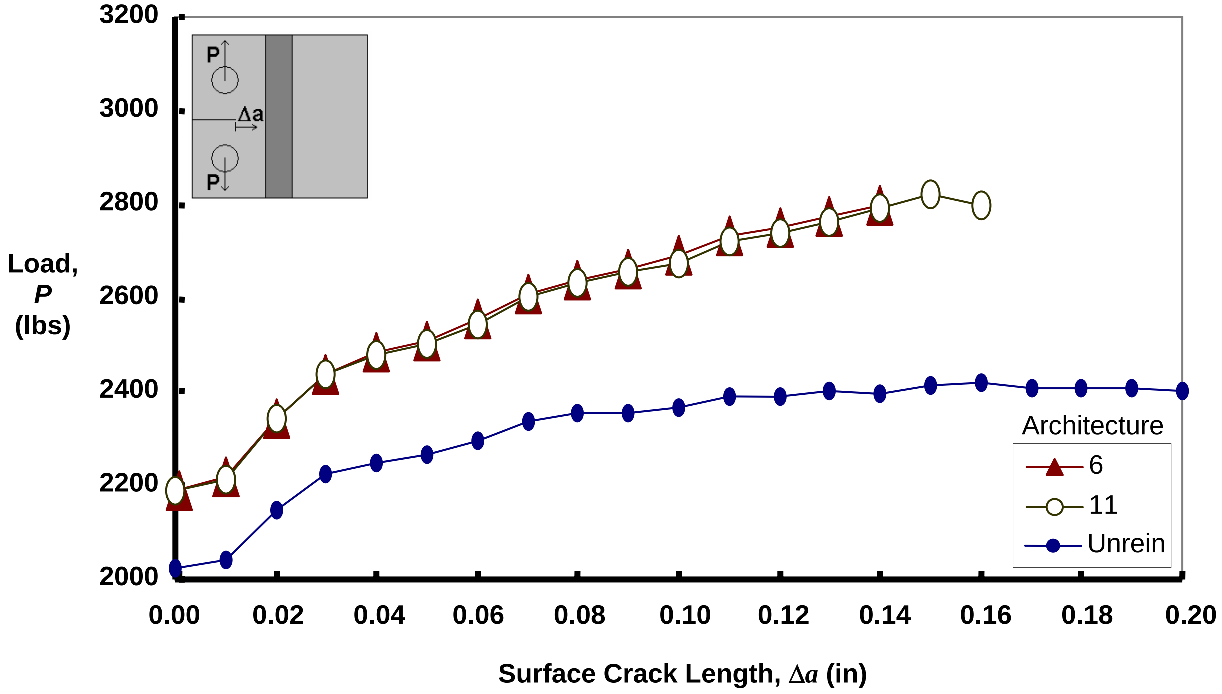

Figure 5.23 Load as a Function of Surface Crack Length for Architecture 6, Architecture 11, and Unreinforced

the comparison between architectures 7 and 8. This is also the reason for the increase in maximum load at initial failure; more reinforcement is strained, thus carrying more load, and increasing maximum load. Initial fiber direction tensile failure of the reinforcement occurs at the inside corner leading edge along the crack plane, as opposed to architecture 6. The failure strain of the 1100 aluminum is never reached in this case either. However, of all the architectures, the 1100 aluminum in this architecture does reach about 75 percent of the failure strain, while all others reach less than 20 percent of the failure strain, based on the maximum principle strain. The reason for this is because of the aluminum tip's location at the free surface, which assumes a plane-stress like state, and causes it to yield sooner, as mentioned in Chapter 2.

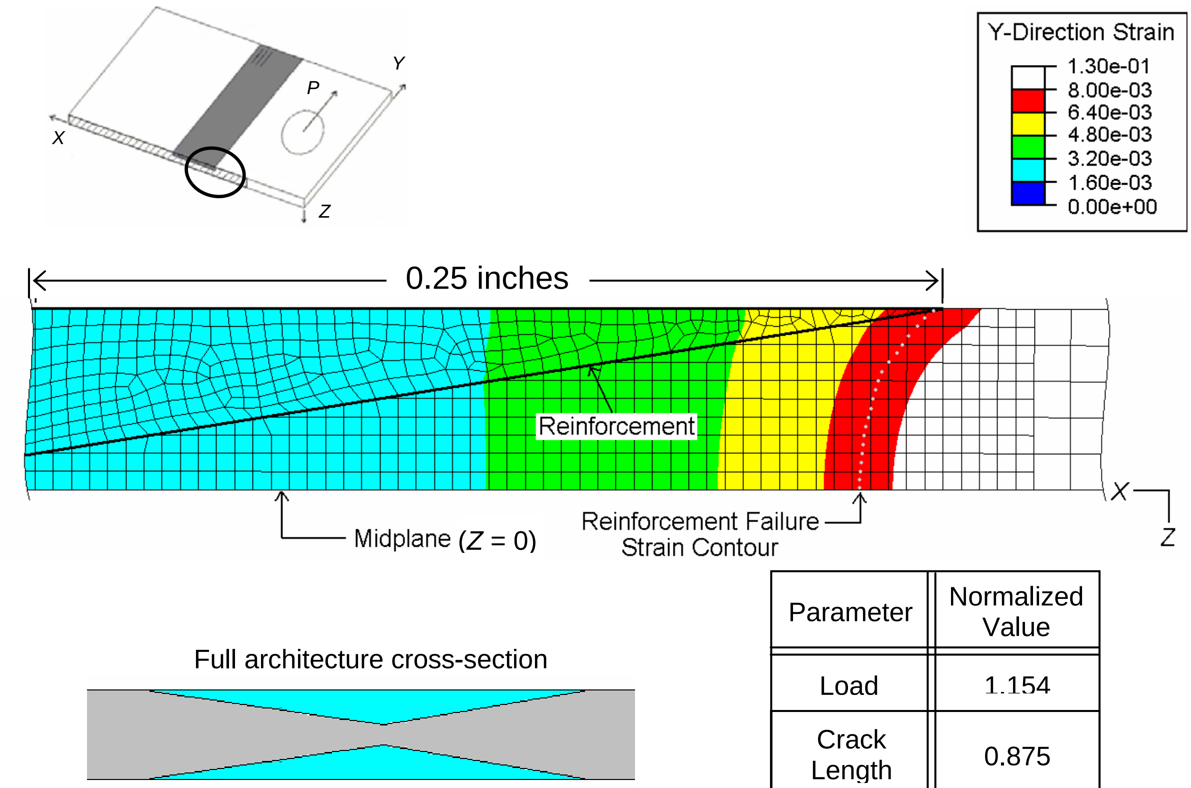

Parameter	Normalized Value
Load	1.154
Crack Length	0.875
R_f	0.577

a) Architecture 6

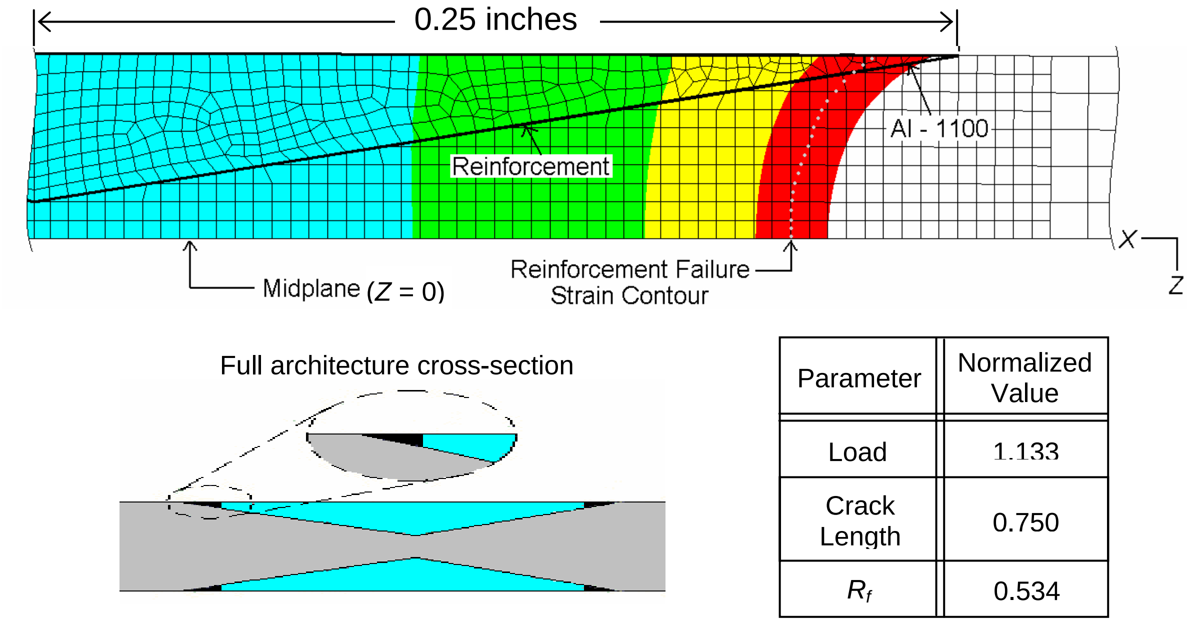

Parameter	Normalized Value
Load	1.133
Crack Length	0.750
R_f	0.534

b) Architecture 11

Figure 5.24 Contours of Extensional Strain ε_{yy} and Performance for Architecture 6 and Architecture 11

Table 5.2 summarizes the performance of all of the triangular reinforcements at initial failure, including normalized maximum load, normalized surface crack length at maximum load, and load ratio. A bar chart comparing the normalized maximum load and load ratio is given in Figure 5.25. As shown in the Table 5.2 and more clearly in Figure 5.25, the load ratio, R_f, follows the trend of normalized maximum load, similar to the rectangular architectures.

Table 5.2 Summary of Results: Triangular Reinforcement Architectures

Architecture Number	Maximum Load (lbs)	Normalized Surface Crack Length at Max Load (in)	Normalized Max Load to Unreinforced Case	Load Ratio, R_f
0 (Unreinforced)	2425	1	1	N/A
6	2798	0.875	1.154	0.577
7	2748	0.750	1.133	0.534
8	2786	0.875	1.149	0.581
9	2791	0.875	1.151	0.581
10	2812	1.063	1.160	0.639
11	2821	0.938	1.163	0.607

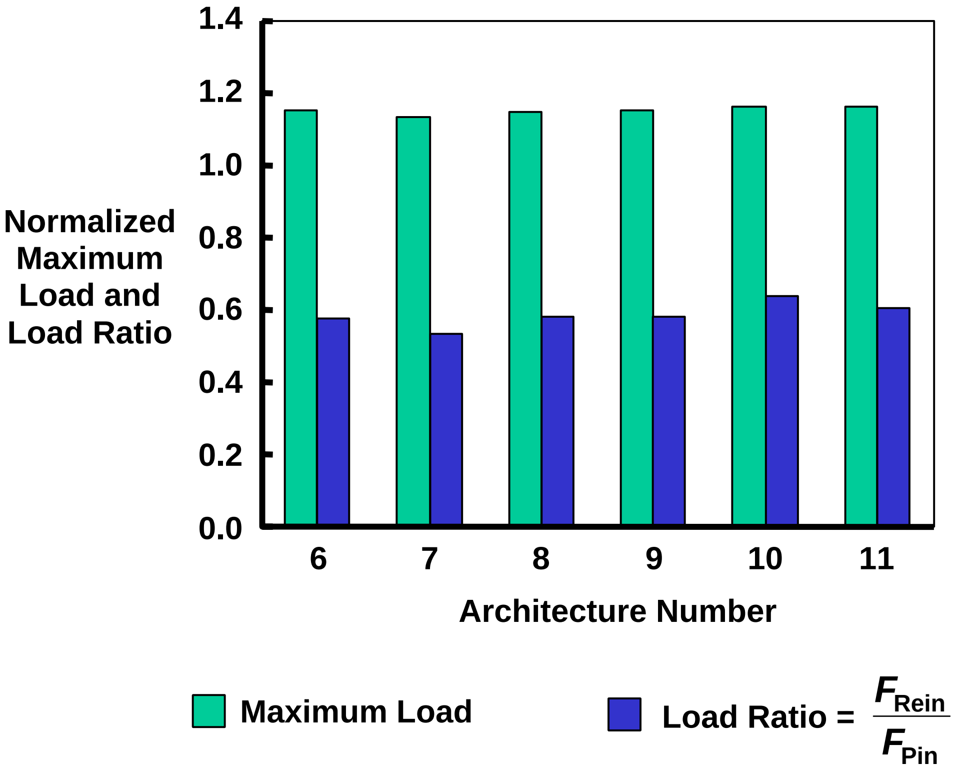

Figure 5.25 Bar Chart Comparison of Maximum Loads and R_f for Triangular Architectures

The results of each of the reinforcement architectures have been given. Each architecture has been compared to a suitable counterpart, and reasons for performance changes have been discussed. The next chapter summarizes the accomplishments of the research relative to the original objectives. Also included are additional peripheral comments regarding selective reinforcement and other suggestions.

Chapter 6 CONCLUSION

A 3-D crack propagation simulation was developed for in-situ selectively reinforced compact tension geometries. Crack propagation was modelled as quasi-static, and a Python script was developed to automate the analysis by releasing nodal constraints (simulating crack propagation) and increasing applied displacement. ABAQUS/Standard was used as the finite element analysis solver. The criteria used for crack propagation was the critical crack tip opening angle. Since this analysis assumes a flat fracture surface, only a quarter-symmetry model was needed. This analysis also approximates tunnelling. The material through which the crack propagates is modelled as elastic-perfectly plastic.

Eleven different reinforcement architectures were investigated, all using the same cross-sectional area. All eleven reinforcement architectures exhibited greater maximum loads than the unreinforced case, showing a 13 to 28 percent increase. This is a relatively large increase, given the fact that the reinforcement comprises only an approximately seven percent volumetric replacement of the entire compact tension specimen volume. For the cases considered, reinforcement geometry gave the largest changes in performance, with the rectangular reinforcements performing better than the triangular reinforcements. Architecture 3 exhibited the largest maximum load at initial failure, showing a 28 percent increase from the unreinforced case. This was the 80 percent thick, rectangular composite reinforcement placed at the midplane. For almost every architecture considered, failure occurred on the leading edge, at a point relatively close to the midplane.

Load sharing is the main mechanism in which maximum load is increased in in-situ selectively reinforced compact tension specimens, as suggested from Farley et al. [12]. The reinforcement architectures investigated possess a higher maximum load at initial failure relative to the unreinforced case. As the maximum load increases, the percentage of the load that the reinforcement carries also increases. How the extensional strain varies throughout the reinforcement shows how the load is distributed. Strain gradients through the thickness and along the width of the reinforcement both show how reinforcement architecture influences how much load the reinforcement carries, and ultimately maximum load. The more reinforcement that is involved in and at high levels of strain, the larger the maximum load.

For these cases, initial composite reinforcement failure occurs when the fiber direction extensional strain reaches the tensile strain failure limit for this composite. Failure of the reinforcement is dependent on the strain fields created by the approaching crack front. The size and shape of the strain fields depend upon the amount of applied loading. Due to the presence of the reinforcement increasing the overall stiffness, larger loads are applied in order to achieve the critical CTOA at the crack front. However, due to increased local stiffening as the failure strain of the composite reinforcement approaches the reinforcement leading edge, the shape of the strain fields are altered.

Although architecture 5 did not perform as well as the other rectangular architectures, it does show potential for a more efficient use of reinforcement. As previously suggested, the three trailing reinforcements not shown in Figure 5.11 are not strained very highly, and may not be contributing any significant load carrying capacity. Removing these reinforcements may not be overly detrimental to the performance. As Abada et al. [45] shows, comparing the geometry of architecture 1, a rectangular reinforcement architecture completely through the thickness, but with only half of the total composite reinforcement volume, exhibits higher performance. The comparison of architectures 7 and 10 also show a more efficient use of reinforcement, despite a lower total cross-sectional area of unidirectional composite reinforcement.

As with any numerical analysis, the actual experiments must be performed to support the results of the numerical models. The analyses described in this research assume things that may not reflect exactly what goes on experimentally. As previously mentioned, in Farley et al. [12], only a single experimental test was done on an unreinforced case and a reinforced case with an epoxy interface. In this research, the reinforcement was assumed to be “perfectly bonded” to the base material. In actuality, there would be some interface effects between the composite and the base aluminum. Due to the added complexity of such a topic, it was not included in this research. Another detail not included in this research, but also important are the different failure modes of the composite itself. Matrix tensile and shear failures would be important to include, as these would also effect the response. Only fiber-direction tensile failure was included in Farley et al. [12], and therefore in this research as well. In the single reinforced experiment from Farley et al. [12], no matrix tensile failures were seen, although these failures might not have been seen, since the epoxy interface would fail long before matrix tensile failure was reached. As previously mentioned, no other failure strengths were given in Farley et al. [12]. To that end, polynomial-type composite failure schemes (such as the Tsai-Wu failure criterion given in [7]) could not be used either. Finally, as previously stated, the effect of a rotated fracture surface on in-situ selectively reinforced compact tension specimens would also be an important consideration, as this rotation would be a definite possibility for this case.

Besides overall performance, other specifics must be taken into account for each architecture. For example, architectures 1 and 2 had similar performance. However, one architecture may be easier to manufacture than the other. Also, suppose that some of these in-situ selective reinforcements schemes are meant to be used on the surface skin of a structure. If this structure is prone to impact, the interior architectures may be more suitable than architectures placed at the outer surface.

REFERENCES

1. "Aircraft Accident Report: Aloha Airlines, Flight 243, Boeing 737-299, N73711, Near Maui, Hawaii, April 28, 1988," Technical Report No. NTSB/AAR-89/03, National Transportation Safety Board.

2. Harris, C. E., 1990, "NASA Aircraft Structural Integrity Program," NASA TM-102637.

3. Norris, G. and Wagner, M., 2001, *Boeing 777 – The Technological Marvel*, MBI Publishing Company, Oscela, WI.

4. Rothman, A., July 2004, "Airbus' 'Big Baby' is Too Big," *Seattle Post-Intelligencer,* Seattle, WA, http://seattlepi.nwsource.com/business/182471_airbusproblem17.html Accessed Nov. 29, 2005.

5. Boeing News Release, June 2003, *"Boeing 7E7 Structure Will Be Made of Composite Materials,"* http://www.boeing.com/news/releases/2003/q2/nr_030612g.html Accessed June 27, 2005.

6. Blichfeldt, B. and McCarty, J. E., 1972, "Analytical and Experimental Investigation of Aircraft Metal Structures Reinforced with Filamentary Composites," NASA CR-2039.

7. Hyer, M. W., 1998, *Stress Analysis of Fiber-Reinforced Composite Materials*, McGraw-Hill, Boston, MA.

8. Garratt, M. D., Bucci, R. J., and Kulak, M., 2004, "FCG Evaluation of New Lower Wing Concept," Proceedings of 15th AeroMat Conference, Seattle, WA.

9. Fredell, R. S., Mueller, R., Borsboom, C., and Buktus, L., 1994, "Bonded Repair of Multiple Site Damage with Glare Fibre Metal Laminate Patches," Proceedings of 1994 USAF Structural Integrity Program Conference, 1994.

10. Bucci, R. J., Private Communication, April 3, 2006.

11. Farley, G. L., 2004, "Selective Reinforcement to Enhance the Structural Performance of Metallic Compression Panels," AIAA-2004-2050, Proc. 45th AIAA/ASCE/ASME/AHS/ASC Structures, Structural Dynamics and Materials Conference, Palm Springs, CA, April 19-22.

12. Farley, G. L., Newman, J. A., and James, M. A., 2004, "Selective Reinforcement to Improve Fracture Toughness and Fatigue Crack Growth Resistance in Metallic

Structures," AIAA-2004-1924, Proc. 45th AIAA/ASCE/AHS/ASC Structures, Structural Dynamics and Materials Conference, Palm Springs, CA.

13. Hibbitt, Karlsson, and Sorenson, 2003, *ABAQUS User's Manual, Version 6.4*, Pawtucket, RI.

14. "Standard Test Method for Plane-Strain Fracture Toughness of Metallic Materials," *Annual Book of ASTM Standards*, **3.01**(E399), ASTM International, West Conshohocken, PA, 1999.

15. Dowling, N. E., 1999, *Mechanical Behavior of Materials, 2nd Edition*, Prentice Hall, Upper Saddle River, NJ.

16. Dawicke, D. S., Sutton, M. A., Newman, J. C., and Bigelow, C. A., 1993, "Measurement and Analysis of Critical CTOA for an Aluminum Alloy Sheet," NASA-TM-109024.

17. Sutton, M. A., Deng, X., Ma, F., Newman, J. C., and James, M., 2000, "Development and Application of a Crack Tip Opening Displacement-Based Mixed Mode Fracture Criterion," *International Journal of Solids and Structures*, **37**, pp. 3591-3618.

18. Yang, S., Chao, Y. J., and Sutton, M. A., 1993, "Higher Order Asymptotic Crack Tip Fields in a Power Law Hardening Material," *Engineering Fracture Mechanics*, **45**, pp. 1-20.

19. Chao, Y. J. and Sutton, M. A., 1994, "On the Fracture of Solids Characterized by One or Two Parameters: Theory and Practice," *Journal of the Mechanics and Physics of Solids*, **42**, pp. 629-647.

20. Hancock, J. W., Reuter, W. G., and Parks, D. M., 1993, "Constraint and Toughness Parameterized by T," ASTM STP 1171, pp. 41-63.

21. Roose, E., Eisele, U., and Silcher, H., "Effect of Stress State on the Ductile Fracture Behavior of Large-Scale Specimens: Constraint Effects in Fracture," ASTM STP 1171, 41-63, 1993.

22. Wells, A. A., 1961, "Unstable Crack Propagation in Metals: Cleavage and Fast Fracture," Proc. of the Cranfield Crack Propagation Symposium 1, pp. 210-230.

23. Rice, J. R. and Sorenson, E. P., 1978, "Continuing Crack Tip Deformation and Fracture for Plane Strain Crack Growth in Elastic-Plastic Solids," *Journal of Mechanics and Physics of Solids*, **26**, pp. 163-186.

24. Shih, C. F., de Lorenzi, H. G., and Andrews, W. R., 1979, "Studies on Crack Initiation and Stable Crack Growth," ASTM STP 668, pp. 65-120.

25. Hellman, D. and Schwalbe, K. H., 1986, “On the Experimental Determination of CTOD Based R-Curves,” Proc. of the Conference on Crack Tip Opening Displacement in Elastic-Plastic Fracture Mechanics, pp. 115-132.

26. Andersson, H., 1973, “Finite Element Representation of Stable Crack Growth,” *Journal of Mechanics and Physics of Solids*, **21**, pp. 337-356.

27. de Koning, A. U., 1977, “A Contribution to the Analysis of Quasi Static Crack Growth in Steel Materials,” *Fracture*, **3**, pp. 25-31.

28. Demofonti, G. and Rizzi, L., 1991, “Experimental Evaluation of CTOA in Controlling Unstable Ductile Fracture Propagation,” ESIS Pub. 9, pp. 693-703.

29. Dawicke, D. S., Newman, J. C., and Bigelow, C. A., 1995, “Three-Dimensional CTOA and Constraint Effects During Stable Tearing in a Thin-Sheet Material,” NASA-TM-109183.

30. Dawicke, D. S., 1995, “Fracture Testing of 2324-T39 Aluminum Alloy,” NASA-CR-198177.

31. Nakamura, T. and Parks, D. M., 1990, “Three-Dimensional Crack Front Fields in a Thin Ductile Plate,” *Journal of Mechanics and Physics of Solids*, **38**, pp. 787-812.

32. Newman, J. C., Bigelow, C. A., and Shivakumar, K. N., 1993, “Three-Dimensional Elastic-Plastic Finite-Element Analyses of Constraint Variations in Cracked Bodies,” *Engineering Fracture Mechanics*, **46**, pp. 1-13.

33. James, M. A. and Newman, J. C., 2003, “The Effect of Crack Tunnelling on Crack Growth: Experiments and CTOA Analyses,” *Engineering Fracture Mechanics*, **70**, pp. 457-468.

34. Hom, C. L. and McMeeking, R. M., 1990, “Large Crack Tip Opening in Thin Elastic-Plastic Sheets,” *International Journal of Fracture*, **45**, pp. 103-122.

35. Gullerud, A. S., Dodds, R. H., Hampton, R. W., and Dawicke, D. S., 1999, “Three-Dimensional Modelling of Ductile Crack Growth in Thin Sheet Metals: Computational Aspects and Validation,” *Engineering Fracture Mechanics*, **63**, pp. 347-374.

36. Dawicke, D. S., Newman, J. C., Starnes, J. H., Rose, C. A., Young, R. D., and Seshadri, B. R., 2000, “Residual Strength Analysis Methodology: Laboratory Coupons to Structural Components,” Technical Document No. 20040086966, NASA Center for AeroSpace Information.

37. James, M. A., Newman, J. C., and Johnston, W. M., 2002, “Three-Dimensional Analyses of Crack Tip Opening Angles and δ_5-Resistance Curves for 2024-T351 Aluminum Alloy,” ASTM STP 1406, pp. 279-297.

38. Seshadri, B. R. and Newman, J. C., 1998, “Analyses of Buckling and Stable Tearing in Thin-Sheet Materials,” NASA-TM-208428.

39. Cook, R. D., Malkus, D. S., Plesha, M. E., and Witt, R. J., 2002, *Concepts and Applications of Finite Element Analysis, 4th Edition*, John Wiley & Sons, Inc., New York, NY.

40. Kapania, R. K., Makhecha, D. P., Johnson, E. R., Simon, J., and Dillard, D. A., 2004, “Modelling Stable and Unstable Crack Growth Observed in Quasi-Static Adhesively Bonded Beam Tests,” IMECE2004-59765, Proc. of 2004 ASME International Mechanical Engineering Congress and Exposition, Anaheim, CA.

41. Fehily, C., 2002, *Visual Quickstart Guide: Python*, Peachpit Press, Berkeley, CA.

42. Sanford, R. J., 2003, *Principles of Fracture Mechanics*, Prentice Hall, Upper Saddle River, NJ.

43. Holt, J. M. and Ho, C. Y., eds., 1996, *Structural Alloys Handbook, 1996 Edition,* CINDAS/Purdue University, West Lafayette, IN.

44. *Metals Handbook, Vol. 2, 10th Edition*, ASM International, 1990.

45. Abada, C. H., Farley, G. L., and Hyer, M. W., 2006, “Fracture Response Enhancement of Aluminum Using In-Situ Selective Reinforcement,” AIAA-2006-2004, Proc. of 2006 47th AIAA/ASCE/AHS/ASC Structures, Structural Dynamics and Materials Conference, Newport, RI, May 1-4.

Appendix A ABAQUS AND PYTHON SCRIPT

The following script is written in Python. It is an object-based programming language, similar to C. This is the primary language ABAQUS uses to read, store, and manage data. Python scripts can be written to modify and create parts, material properties, loads, steps, interactions, and almost any aspect of an ABAQUS model. They can also be written to read from and write to ABAQUS input files, output databases, any text-based file, as well as creating and running ABAQUS jobs.

In this analysis, the original model of the compact tension specimen was built using ABAQUS/CAE. The initial load was applied to the specimen, and several node and element sets were defined within CAE. At this point, the input file was written. The Python script below takes this ABAQUS model data and initial loading contained in the input file as an argument. It then builds on this original input file to propagate the crack through the CT specimen, using the crack-tip opening angle criterion.

Although this script does automate crack propagation and progressive failure, many things must be pre-defined by the user in order for this script to be successful. These will be mentioned in subsequent comments as they arise throughout the code, but the two main ones worth mentioning at this point are the constraint block file and the displacement block file. The use of these two files lends flexibility to the code, but adds a level of complexity on the part of the user when setting up the problem.

Due to the nature of the problem, only two types of loading (or unloading) are required: an applied displacement at the pin, and a symmetry constraint removal along the crack front, to simulate crack propagation. Because ABAQUS only needs a single text-based input file deck, this makes it easy, in theory, to just append additional loading/unloading blocks (with minor changes) to the end of the original input file. These blocks must also accurately reflect the original ABAQUS model, so, if possible, must be independent of any internally created objects from ABAQUS/CAE. This is crucial when creating models with different reinforcement geometries, material properties, and meshes. Because of this, great care must be taken when creating the original models in ABAQUS/CAE. Every referenced node and element set within the script must be given a name within CAE. However, once this is done, these two blocks can be easily altered due to its constant text file size, positioning, etc.

Two restart input files are created to further minimize total run time and file creation. Each restart file consists of only a single step containing either a displacement or constraint removal block, thus they have fairly short run times. When the script is first run, the first restart file restarts from the last step in the initial input file written from ABAQUS/CAE. The next input file restarts from the first file. Using alternating restart indices in the job names, only two restart files are needed, since they can continually overwrite the old ones.

In order to understand the script more clearly, the higher-level functions are described in detail, followed by their lower level constituent functions. The inputs, user-defined items, code flow, and important output variables are commented to each. The version of code below is for a reinforced compact tension specimen, and the analysis ends when either the reinforcement has failed, or the user-defined crack length has been reached. Some remnants of other versions, some of which include progressive failure, other failure modes, or critical CTOA variation through the thickness still remain, but are ignored in this version.

```
# The following function is the main function a user will call when
# running a job.  It initializes all of the necessary files for use in
# the rest of the script.  The inputs are all user-defined: the
# critical CTOA (“critCtoa”), the name of the ABAQUS input file written
# from ABAQUS/CAE (“jobname”), the CTOA measurement point given in
# number of elements behind the crack tip (“measpoint”), the
# terminating midplane crack length given in number of elements (“n”),
# and the reinforcement failure strains (“strainFail”).  The failure
# strains are input in a list form, starting with the fiber direction
# tensile failure strain.
#
# The original input file text is copied to the master input file.  All
# lock and “Steps.txt” files are removed from the directory where
# ABAQUS is being run.  The displacement and constraint block files are
# then copied from master files.  The variable “critCtoa” is redefined
# here as a list containing the coefficients to the equations
# specifying the variation in critical CTOA.  The input file is then
# run, and the function “MasterRun” is called.

def Test(critCtoa, jobname, spread, measpoint, n, strainFail, numcpus):
      carriage='\012'
      inputFile=open(jobname+'.inp')
      outputFile=open('Master.inp','w')
      lines=inputFile.readlines()
      for line in lines:
```

```
              newLine=line
              outputFile.write(newLine)
      inputFile.close()
      outputFile.close()
      ConstraintBlockCopy(jobname)
      import os
      os.system('rm Loads.txt')
      os.system('rm *.lck')
      os.system('rm StatusTest.txt')
      os.system('rm Steps.txt')
      File=open('Steps.txt','w')
      File.write('1'+carriage)
      File.close()
      inputFile=open('Loads.txt','w')
      inputFile.writelines(str(critCtoa)+', '+str(jobname)+',
'+str(spread)+', '+str(measpoint)+', '+str(strainFail)+carriage)
      inputFile.close()
      inputFile=open('StatusTest.txt','w')
      inputFile.writelines(str(critCtoa)+', '+str(jobname)+',
'+str(spread)+', '+str(measpoint)+', '+str(strainFail)+carriage)
      inputFile.close()
      os.system('cp displacementBlockMaster.txt displacementBlock.txt')
      os.system('cp constraintBlockMaster.txt constraintBlock.txt')
      critCtoa=CtoaCalc(critCtoa, spread)
      os.system('abaqus job='+jobname+' cpus='+str(numcpus)+'
interactive')
      MasterRun(critCtoa, jobname, spread, measpoint, n, strainFail,
numcpus)
      return

# The following function copies only the pertinent lines of the
# constraint removal step, and creates a text file that contains the
# relevant information to define the constraints.
#
# After reading in the original file, “jobname”, the file is then
# searched for the beginning of the constraint removal step.  From this
# characteristic statement on, the text is copied to another file,
# “constraintBlockMaster.txt”.

def ConstraintBlockCopy(jobname):
        inputFile=open(jobname+'.inp')
        lines=inputFile.readlines()
        inputFile.close()
        addline='\012'
        index=lines.index('** STEP: Step-2'+addline)
        outputFile=open('constraintBlockMaster.txt','w')
        outputFile.writelines(lines[(index-2):])
        outputFile.close()
        return

# The following function takes in the user-defined constant critical
# CTOA, “critCtoa”.  It also takes two times the difference between the
# constant critical CTOA and the initial critical CTOA, “spread”.  It
# outputs the coefficients to the assumed quadratic equation that will
# describe the x-direction change in critical CTOA for each through-
# thickness profile.
#
```

```
# After initializing a number of lists, the coefficients for initial
# critical CTOA variation as a function of profile crack length is
# calculated.  These coefficients are returned as a nested list.

def CtoaCalc(critCtoa, spread):
        y0=[0,0,0,0,0]
        y10=[0,0,0,0,0]
        A=[0,0,0,0,0]
        B=[0,0,0,0,0]
        C=[0,0,0,0,0]
        D=float(spread)/(0.04**2)
        E=critCtoa-float(spread)/2
        for n in range(0,5):
                y0[n]=D*(n*0.01)**2+E+0.01
                y10[n]=critCtoa
                A[n]=(y0[n]-critCtoa)/0.0081
                B[n]=-0.2*A[n]
                C[n]=0.01*A[n]+critCtoa
        for n in range(0,4):
                A[n]=A[4]
                B[n]=B[4]
                C[n]=C[4]
        return [A, B, C, D, E, y0]

# This following routine calls almost all of the functions that will be
# defined from this point on.  It is a self-recursive function, with
# the following inputs: the critical CTOA coefficient list
# (“critCtoa”), the job name (“jobname”), the CTOA variation measure
# (“spread”), the CTOD measurement point (“measpoint”), the terminating
# tunnelled crack length (“n”), the failure strains (“strainFail”), and
# the number of cpus to be used for each execution of ABAQUS
# (“numcpus”).  This function will output a single input file
# containing full crack propagation, as well as the relevant loads and
# crack lengths.
#
# This function contains the most important, yet painstaking pre-
# defined element sets.  These are the node sets used to define the
# symmetry constraints along the crack propagation surface.  These sets
# are named in ABAQUS/CAE.  For ease, these were defined in the part
# module, so different reinforcement geometries could be partitioned,
# and different meshes used.  This is the reason for the “Hole-1” part
# instance prefix that is automatically included once the input file is
# written.  In the part module, the naming convention must be “C-
# (thickness position index)-(profile crack length index)”, and must
# start after the initial constraints of BC1, BC2, BC3, BC4, and BC5.
# For example, for an element at the midplane, 0.2 inches from the
# blunted crack tip, the name would be “C-0-20”.  For an element on the
# surface, 0.05 inches from the blunted crack tip, its name would be
# “C-4-5”.
#
# Because of the importance of this function, details of the logic
# itself are given.  After reading in the appropriate inputs, important
# data is extracted from the previously run job.  In order to better
# keep track of where in the analysis the script is, the previous step
# number, user-defined critical CTOA, and measurement point are all
# printed to the screen and to the file, “StatusTest.txt”.  The index,
# “k”, is used for a progressive failure version of this script, but
```

```
# the script below is rewritten to ignore this.  The strains in the
# reinforcement are read in and checked to see if failure has occurred,
# and assigns a value to the index “m”.  The measured CTOD’s are
# then read in and the list “minU2” is created.  For the first few
# steps, “minU2” is altered to reflect the consecutive constraint
# removal after the initial crack tip.  Next, a restart job name is
# created.  If the user-defined crack length has been reached, the
# important files are copied to a directory, and the script it ended.
# If the reinforcement has failed, then the last step is rerun with an
# increased number of increments to more accurately find the point of
# reinforcement failure, the important files are copied to a directory,
# then the script is ended.  If the critical CTOA has been reached
# according to the variable, “minU2”, then the constraint block is
# altered to reflect the removal of the specified constraints.  The
# step number corresponding to a surface constraint release is also
# created and appended in order to more easily track surface crack
# growth.  The constraint block is appended to the restart job file and
# the file is run.  The “MasterRun” function itself is then recalled.
# If the critical CTOA has not been reached along any profile, then the
# displacement block is altered to reflect a larger applied pin
# displacement.  This new displacement block is appended to the restart
# file, and the file is run.  The “MasterRun” function is again
# recalled.
#
# One of the main advantages of this function is the ease in restarting
# a job from a specific step.  Occassionally, ABAQUS/Standard fails to
# complete a job due to memory problems or other system failures.  Jobs
# can be rerun quite easily, just by using the last successfully
# completed job name.

def MasterRun(critCtoa, jobname, spread, measpoint, n, strainFail,
numcpus):
      import os
      carriage='\012'
      previousData=ExtractLastData(jobname)
      globalDispl=previousData[0]
      stepnumber=previousData[1]
      incrNumber=previousData[2]
      stepSize=previousData[3]
      outputCtoa=critCtoa[0][4]*0.1**2+critCtoa[1][4]*0.1+critCtoa[2][4]
      print stepnumber,'-', outputCtoa,'-', spread, '-', measpoint
      k=[0,1,0,[0,0,0,0]]
      FailIndex=k[2]
      maxIndeces=k[3]
      inputFile=open('StatusTest.txt','a')
      inputFile.writelines('GlobalDispl='+str(globalDispl)+',
Stepnumber='+str(stepnumber)+', IncrNumber='+str(incrNumber)+',
StepSize='+str(stepSize)+carriage)
      inputFile.close()
      m=[0,1]
      s=[0,1, globalDispl]
      m=ReadStrain(jobname, stepnumber, strainFail, incrNumber)
      incrNumber=m[1]
      minU2=ReadDispl(critCtoa, jobname, stepnumber, spread, measpoint,
maxIndeces)
      minU2=InitialRelease(stepnumber, globalDispl, minU2)
      inputFile=open('StatusTest.txt','a')
```

```
      inputFile.writelines('minU2='+str(minU2)+carriage)
      inputFile.close()
      addline=', YSYMM\012'
      inputFile=open('StatusTest.txt','a')
      inputFile.write('k='+str(k)+carriage+'m='+str(m)+carriage+'s='+str(s
)+carriage)
      inputFile.close()
      restJobname=RestartManager(jobname, stepnumber)
      if minU2[0][3] == n:
                inputFile=open('Master.inp')
                jobname='Master'+jobname[0:(jobname.find('-rest-
'))]+str(outputCtoa)+'-'+str(spread)+'-'+str(measpoint)
                outputFile=open(jobname+'.inp','w')
                lines=inputFile.readlines()
                for line in lines:
                        newLine=line
                        outputFile.write(newLine)
                inputFile.close()
                outputFile.close()
                os.system('mkdir '+jobname)
                os.system('cp Steps.txt Steps'+jobname+'.txt')
                os.system('cp StatusTest.txt StatusTest'+jobname+'.txt')
                os.system('cp Loads.txt Loads'+jobname+'.txt')
                os.system('cp *'+jobname+'*.* '+jobname)
                return
      elif m[0]==1:
            incrNumber=m[1]
            IncrEndFile(jobname, incrNumber, float(1), globalDispl,
globalDispl)
            ChangeMasterEndIncr(incrNumber, float(1), stepnumber,
globalDispl, globalDispl)
            Output='FailIndex='+str(k[2])+',
CTODIndex='+str(minU2[6])+carriage+'-'+carriage+'Initial Failure'
            print Output
            inputFile=open('StatusTest.txt','a')
            inputFile.writelines(Output+carriage)
            inputFile.close()
            inFile=open('Loads.txt','a')
            inFile.writelines(str(stepnumber)+'Initial Failure -
'+str(m[2])+' - '+str(m[3])+', ')
            inFile.close()
            os.system('abaqus job='+jobname+' oldjob='+restJobname+'
cpus='+str(numcpus)+' interactive')
            dirName='RestDir'+jobname+'-'+str(outputCtoa)+'-'+str(spread)
            os.system('mkdir '+dirName)
            os.system('cp '+jobname+'.* '+dirName)
            os.system('cp '+restJobname+'.* '+dirName)
            for i in range(1,5):
                    os.system('cp constraintBlock.txt '+dirName)
                    os.system('cp displacementBlock.txt '+dirName)
                    os.system('cp Master.inp '+dirName)
                    os.system('cp Steps.txt '+dirName)
                    os.system('cp Loads.txt '+dirName)
                    os.system('cp StatusTest.txt '+dirName)
            return
        elif minU2[5]==1:
                for i in range(0,5):
```

```
                        if minU2[i][0] > (minU2[i][2]-0.000025):
                                constraintName = 'Hole-1-1.C-'+str(i)+'-
'+str(minU2[i][3])+addline
                                if constraintName[0:10]=='Hole-1-1.C-4':
                                        outFile=open('Steps.txt','a')

outFile.write(str(stepnumber)+carriage)
                                        outFile.close()
                                ConstraintRemoval(constraintName,
globalDispl)
                stepnumber=AppendBlock('constraintBlock', restJobname,
stepnumber)
                Output='FailIndex='+str(k[2])+',
CTODIndex='+str(minU2[6])+carriage+'-'+carriage+'Constraint'
                print Output
                inputFile=open('StatusTest.txt','a')
                inputFile.writelines(Output+carriage)
                inputFile.close()
                inFile=open('Loads.txt','a')
                inFile.writelines(str(stepnumber)+', Constraint, ')
                inFile.close()
                os.system('abaqus job='+restJobname+' oldjob='+jobname+'
cpus='+str(numcpus)+' interactive')
                jobname=restJobname
                MasterRun(critCtoa, jobname, spread, measpoint, n,
strainFail, numcpus)
      else:
            FailIndex=k[2]
            displIncrement=DispConverge(minU2, FailIndex, incrNumber)
            globalDispl=AddDispl(globalDispl, displIncrement)
            stepnumber=AppendBlock('displacementBlock', restJobname,
stepnumber)
            Output='FailIndex='+str(k[2])+',
CTODIndex='+str(minU2[6])+carriage+'-'+carriage+'Displacement'
            print Output
            inputFile=open('StatusTest.txt','a')
            inputFile.writelines(Output+carriage)
            inputFile.close()
            inFile=open('Loads.txt','a')
            inFile.write(str(stepnumber)+', Displ, ')
            inFile.close()
            os.system('abaqus job='+restJobname+' oldjob='+jobname+'
cpus='+str(numcpus)+' interactive')
            jobname=restJobname
            MasterRun(critCtoa, jobname, spread, measpoint, n, strainFail,
numcpus)

# The first function called from “MasterRun” above pulls out important
# data from the previously run job that will be needed for subsequent
# functions.  It takes in the previous job name (“jobname”) as an
# input, and extracts the number of increments, pin displacement, and
# step number from the previous job input file.  These values are then
# returned in a list.
#
# Upon calling this function, the input file corresponding to the job
# name is opened.  Several unique lines of text in the input file are
# searched for, which locate the desired values.  After reformatting
```

```
# the desired values within the string-based file, the function returns
# the pin displacement, step number, and number of increments.

def ExtractLastData(jobname):
      inputFile=open(str(jobname)+'.inp')
      lines=inputFile.readlines()
      lines=[s.rstrip() for s in lines]
      addline='\012'
      for i in range(0,len(lines)):
            if lines[i]=='*Static':
                        incrLine=lines[i+1]
      for line in lines:
            if line[0:4]=='Load':
                  globDispLine=line
            elif line[0:7]=='** STEP':
                  stepLine=line
      semi=incrLine[(incrLine.find(',')+1):]
      stepSize=float(semi[0:(semi.find(','))])
      incrSize=float(incrLine[0:(incrLine.find(','))])
      incrNumber=int(round(float(1)/incrSize))
      globalDispl=float(globDispLine[12:])
      stepnumber=int(stepLine[14:])
      inputFile.close()
      return [globalDispl, stepnumber, incrNumber, stepSize]

# The next function reads in the strain values in the reinforcement.
# It uses the previous job name (“jobname”), step number
# (“stepnumber”), failure strain (“strainFail”), and number of
# increments (“incrNumber”) as inputs.  If the maximum measured fiber
# direction tensile strain is greater than the failure strain at the
# end of the step, the number of increments is increased to 15 and the
# failure index is set to one.  These two values are then returned.  If
# there is no fiber direction tensile failure, the incrementation index
# is zero, and the increment number remains as one.
#
# It should be noted that this function allows for shear failure to be
# detected as well.  However, since no shear failure values were given,
# the function just ignores these failure components.
#
# The user must define the element set “REIN” as the reinforcement
# region within ABAQUS/CAE.

def ReadStrain(jobname, stepnumber, strainFail, incrNumber):
      from odbAccess import *
      from abaqusConstants import *
      odb=openOdb(path=jobname+'.odb')
      stepname='Step-'+str(stepnumber)
      reinRegion=odb.rootAssembly.elementSets['REIN']
      strainField=odb.steps[stepname].frames[-1].fieldOutputs['LE']
      field=strainField.getSubset(region=reinRegion,
position=INTEGRATION_POINT)
      fieldValues=field.values
      s1=[]
      strainFail22=strainFail[0]
      strainFail12=strainFail[1]
      strainFail13=strainFail[2]
      strainFail23=strainFail[3]
```

```
      carriage='\012'
      for v in fieldValues:
            s1.append([v.data[1]/strainFail22,
abs(v.data[3]/strainFail12), abs(v.data[4]/strainFail13),
abs(v.data[5]/strainFail23)])
      for i in range(0, len(s1)):
            for j in range(0,4):
                  maxStrain=s1[i][j]
                  if maxStrain > 1.0:
                        incrNumber=15
                        if j==0:
                              odb.close()
                              comp='E22'
                              return [1, incrNumber, maxStrain, comp]
                        elif j==1:
                              comp='E12'
                        elif j==2:
                              comp='E13'
                        elif j==3:
                              comp='E23'
                        print str(maxStrain)+' - '+comp
      odb.close()
      return [0, 1]

# The following function reads in vertical nodal displacements from the
# previously run job and step.  It then compares these displacements to
# calculated critical CTODs.  Inputs to this function are the redefined
# nested list of coefficients (“critCtoa”), the previous job name
# (“jobname”), the previous step number (“stepnumber”), and the user-
# defined measurement point index (“measpoint”).  It outputs a list
# containing the CTODs at each through-thickness crack profile, their
# corresponding critical CTODs, the profile crack length index, the
# node number where the CTOD was measured, and the averaged critical
# CTODs.
#
# Five nodal sets are pre-defined within ABAQUS/CAE called Z0, Z1, Z2,
# Z3, and Z4.  These sets run along a line in the x-direction on the
# crack/symmetry plane.  Each set represents a different crack profile
# through the thickness of the specimen.  For example, Z0 runs along
# the midplane of the specimen, while Z4 runs close to the surface of
# the specimen.  The node set lines begin at the blunted crack tip, and
# end at 0.02 inches from the reinforcement.  Another user-defined
# variable is the critical CTOD offset, which defines the small “range”
# of critical CTODs.  It is set at 0.000025 inches.  Also, the portion
# of the model that contains the loading pin and the crack propagation
# region must be called “HOLE-1” in ABAQUS/CAE.
#
# Following the script, after reading in vertical nodal displacement
# values along each through-thickness node set; any constrained nodes
# (i.e., approximately zero displacement) are filtered out.  Next,
# critical CTOD values are calculated, depending on crack profile
# length and measurement point distance.  Finally, if the maximum CTOD
# along any profile is greater than the critical CTOD (minus a small
# displacement offset, in this case 0.000025 inches), a constraint
# removal index of 1 is returned.  This index dictates whether the next
# appended block, or step, will be a constraint removal or a
# displacement.  This index, along with the CTODs, averaged CTODs,
```

```
# critical CTODs, and profile crack lengths are returned in the list
# "minU2".

def ReadDispl(critCtoa, jobname, stepnumber, spread, measpoint,
maxIndeces):
        from odbAccess import *
        from abaqusConstants import *
        odb=openOdb(path=jobname+'.odb')
        stepname='Step-'+str(stepnumber)
        minU2=[1, 1, 1, 1, 1, 0, 0]
        for i in range(0,5):
                profile=odb.rootAssembly.nodeSets['Z'+str(i)]
                lastFrame=odb.steps[stepname].frames[-1]
                displ=lastFrame.fieldOutputs['U']
                ctod=displ.getSubset(region=profile)
                ctodValues=ctod.values
                s=[]
                for v in ctodValues:
                        if v.data[1] > 1E-17:
                                nodeCoord=odb.rootAssembly.
instances['HOLE-1-1'].nodes[(v.nodeLabel-1)].coordinates[0]
                                s.append([nodeCoord, v.data[1],
v.nodeLabel, 1, 0, 0])
                s.sort()
                for j in range(0,len(s)):
                        del s[j][0]
                x=len(s)
                if x==0:
                        minU2[i]=[0, 0, 1, 0, 0]
                elif x <= measpoint:
                        critCtod=(critCtodCalc(critCtoa, x, i, measpoint))
                        s[x-1][2]=critCtod
                        s[x-1][4]=s[x-1][0]
                        minU2[i]=s[x-1]
                else:
                        critCtod=(critCtodCalc(critCtoa, x, i, measpoint))
                        s[measpoint-1][2]=critCtod
                        s[measpoint-1][4]=s[measpoint-1][0]
                        s[measpoint-1][0]=((s[measpoint][0]+s[measpoint-
2][0])/2+s[measpoint-1][0])/2
                        minU2[i]=s[measpoint-1]
                minU2[i][3]=x
        crackLength=minU2[4][3]
        displIndex=0
        for i in range(0,5):
                if minU2[5]==1:
                        for j in range(0,5):
                                newDisplIndex=minU2[j][4]/minU2[j][2]
                                if newDisplIndex > displIndex:
                                        displIndex=newDisplIndex
                        minU2[6]=displIndex
                        break
                elif minU2[i][0] > (minU2[i][2]-0.000025):
                        minU2[5]=1
        odb.close()
        LoadRecord(jobname, stepnumber, crackLength, maxIndeces,
displIndex)
```

```
        return minU2

# The first called function from “ReadDispl” receives the following as
# inputs: the redefined nested coefficient list (“critCtoa”, which was
# initially defined as the user-defined critical CTOA), the profile
# crack length measurement number (“x”), the through-thickness
# measurement index (“i”), and the measurement point index number
# (“measpoint”).  As a sidenote, since the elements in the crack face
# plane are square, the actual measured profile crack length, through-
# thickness position, and measurement point distance are just the
# variables “x”, “i”, and “measpoint” multiplied by the element size of
# 0.01 inches. The function outputs the critical CTOD depending upon
# measurement point, through-thickness distance, and profile crack
# length.
#
# The only user-defined item is the variation in the critical CTOA as a
# function of crack profile growth for crack growth less than 0.1
# inches.  This was mentioned in the details of the previous function,
# “CtoaCalc”.  In this case, the variation is assumed to be quadratic.
#
# After redefining each coefficient from the nested coefficient list,
# “critCtoa”, measurement point and profile crack length dependencies
# are applied.  If the amount of crack growth at a specific profile is
# less than the measurement point length, the critical CTOA is
# calculated, and the critical CTOD using the total x-direction crack
# profile length is returned.  If the amount of profile crack growth is
# between the measurement point distance and 0.1 inches, the critical
# CTOA is calculated, and the critical CTOD calculated at the
# measurement point is returned.  If the amount of profile crack growth
# is larger than 0.1 inches, then it returns the critical CTOA and
# calculated critical CTOD which are constant.

def critCtodCalc(critCtoa, x, i, measpoint):
      import math
      A=critCtoa[0]
      B=critCtoa[1]
      C=critCtoa[2]
      if x < measpoint:
            critCtoa=A[i]*(0.01*x)**2+B[i]*(0.01*x)+C[i]
            critCtod=(0.01*x)*math.tan((critCtoa/2)*math.pi/180)
            return critCtod
      elif 10 > x >= measpoint:
            critCtoa=A[i]*(0.01*x)**2+B[i]*(0.01*x)+C[i]
            critCtod=(0.01*measpoint)*math.tan((critCtoa/2)* math.pi/180)
            return critCtod
      else:
            critCtoa=A[i]*0.1**2+B[i]*(0.1)+C[i]
            critCtod=(0.01*measpoint)*math.tan((critCtoa/2)* math.pi/180)
            return critCtod

# The last called function from “ReadDispl” below uses the previous
# jobname, step number, surface crack length (“crackLength”), and the
# displacement index (“displIndex”) defined as the largest ratio
# between the critical CTOD and measured CTOD.  This function outputs
# and appends to a file containing the applied pin loads and surface
# crack lengths.
#
```

```
# The user must define a node set in ABAQUS/CAE that passes through the
# center of the loading pin.  This node set is the same node set that
# the applied displacements act upon, and the node set is called
# “Load”.

def LoadRecord(jobname, stepnumber, crackLength, maxIndeces, displIndex):
        from odbAccess import *
        from abaqusConstants import *
        odb=openOdb(path=jobname+'.odb')
        stepname='Step-'+str(stepnumber)
        loadProfile=odb.rootAssembly.nodeSets['LOAD']
        lastFrame=odb.steps[stepname].frames[-1]
        loadValues=lastFrame.fieldOutputs['RF'].
getSubset(region=loadProfile).values
        s=[]
        for v in loadValues:
                s.append(v.data[1])
        sum=0
        for i in range(0,len(s)):
                sum=sum+s[i]
        inputFile=open('Steps.txt')
        outputFile=open('Loads.txt','a')
        lines=inputFile.readlines()
        lines=[x.strip() for x in lines]
        addline='\012'
        outputFile.write(str(sum)+', '+str(crackLength)+',
'+str(maxIndeces[0])+', '+str(maxIndeces[1])+', '+str(maxIndeces[2])+',
'+str(maxIndeces[3])+', '+str(displIndex)+addline)
        inputFile.close()
        outputFile.close()
        odb.close()
        return

# The next function that is called in “MasterRun” takes the following
# inputs: previous step number (“stepnumber”); the applied pin
# displacement (“globalDispl”) at that step number; and the nested list
# (“minU2”) containing the measured CTOD, critical CTOD, and crack
# growth length of each through-thickness profile, as well as the
# constraint removal index.  If applicable, it returns an altered
# nested list, “minU2”, along with an altered constraint removal block
# file.
#
# For this function, the user must define the node sets of the first
# element row in ABAQUS/CAE.  Since there are five elements through the
# thickness, these node sets must be called (starting from the midplane
# element) “BC1”, “BC2”, “BC3”, “BC4”, and “BC5”.  The constraint block
# file itself must also be pre-defined.
#
# Since this function takes the previous step as an input, in the next
# step, the first midplane constraint will be released; then in the
# following step, the next constraint; etc.  The constraint to be
# released is input into the function “ConstraintRemoval”, and “minU2”
# is altered with a new constraint removal index to denote that the
# next block will be a constraint removal block.

def InitialRelease(stepnumber, globalDispl, minU2):
      addline=', YSYMM\012'
```

```
      if 1 < stepnumber < 6:
            constraintName='BC'+str(stepnumber)+addline
            ConstraintRemoval(constraintName, globalDispl)
            minU2[5]=1
            return minU2
      else:
            return minU2

# The following function initially called in “InitialRelease” and used
# in “MasterRun” is used to remove specific constraints from the next
# step in ABAQUS.  It takes the name of the constraint
# (“constraintName”) and the pin displacement (“globalDispl”) as
# inputs.  It outputs an altered constraint block file.
#
# As mentioned previously in the introduction, the text file
# “constraintBlockMaster.txt” must be pre-defined by the user.  This
# text file is copied to “constraintBlock.txt” during the initial
# function, “Test”.
#
# After opening the constraint file and a temporary constraint file,
# the line in the text file where the input constraint name exists is
# replaced with a comment, “***”.  The applied pin displacement is also
# updated.  The temporary constraint file is re-copied to the original
# constraint file.

def ConstraintRemoval(constraintName, globalDispl):
      comment='***\012'
      inputFile=open('constraintBlock.txt')
      outputFile=open('constraintBlockNew.txt','w')
      lines=inputFile.readlines()
      for line in lines:
            if line==str(constraintName):
                  newLine=comment
            elif line[0:4]=='Load':
                  newLine='Load, 2, 2, '+str(globalDispl)+'\012'
            else:
                  newLine=line
            outputFile.write(newLine)
      inputFile.close()
      outputFile.close()
      inputFile=open('constraintBlockNew.txt')
      outputFile=open('constraintBlock.txt','w')
      lines=inputFile.readlines()
      for line in lines:
            newLine=line
            outputFile.write(newLine)
      inputFile.close()
      outputFile.close()
      return

# The next function below called in “MasterRun” uses the previous job
# name, “jobname”, and step number, “stepnumber” as inputs.  It returns
# a restart job name that depends on the restart index, and an input
# file of the same name that contains the first few lines needed for an
# ABAQUS restart input file.
#
# After reading in the step number, the function sets a restart index
```

```
# number depending on whether the stepnumber is odd or even.  The
# restart job name is then created by concatenating the original job
# name, and adding the restart index number to it.  A restart input
# file is created using the restart job name and the previous step
# number.

def RestartManager(jobname, stepnumber):
      addLine='\012'
      if (float(stepnumber%2))==1:
            restartIndex=1
      else:
            restartIndex=2
      restJobname=jobname[0:(jobname.find('-rest-'))]
      restJobname=restJobname+'-rest-'+str(restartIndex)
      inputFile=open(restJobname+'.inp', 'w')
      inputFile.write('*Heading'+addLine+'**jobname:
'+restJobname+addLine+'*Preprint, echo=NO, model=NO, history=NO,
contact=NO'+addLine+'*Restart, read, step='+str(stepnumber)+addLine)
      inputFile.close()
      return restJobname

# Once the failure has been detected at the end of a step, the
# following two functions change the increment size of the previously
# run job and the increment size of the last step of the master input
# file, respsectively.  The first one uses the previous job name,
# number of increments, step size, pin displacement, and new pin
# displacement as inputs, and alters the previous job input file with
# the updated increment size.  The second function uses the number of
# increments, step size, step number, pin displacement, and new pin
# displacement as inputs, and alters the master input file to reflect
# the changes.

def IncrEndFile(jobname, incrNumber, MaxTimeIncr, globalDispl,
newGlobalDispl):
        inputFile=open(jobname+'.inp')
        lines=inputFile.readlines()
        addline='\012'
        incrSize=float(1)/incrNumber
        for i in range(0,len(lines)):
                if lines[i]=='*Static'+addline:
                        lines[i+1]=str(incrSize)+', '+str(MaxTimeIncr)+',
1e-05, '+str(incrSize)+addline
              if lines[i]=='Load, 2, 2, '+str(globalDispl)+addline:
                    lines[i]='Load, 2, 2, '+str(newGlobalDispl)+addline
        inputFile.close()
        inputFile=open(jobname+'.inp','w')
        inputFile.writelines(lines)
        inputFile.close()

def ChangeMasterEndIncr(incrNumber, MaxTimeIncr, stepnumber, globalDispl,
newGlobalDispl):
        inputFile=open('Master.inp')
        lines=inputFile.readlines()
        inputFile.close()
        incrSize=float(1)/incrNumber
        addline='\012'
        for i in range(0,len(lines)):
```

```
                if lines[i] == '** STEP: Step-'+str(stepnumber)+addline:
                        lines[i+4]=str(incrSize)+', '+str(MaxTimeIncr)+',
1e-05, '+str(incrSize)+addline
            if lines[i]=='Load, 2, 2, '+str(globalDispl)+addline:
                        lines[i]='Load, 2, 2,
'+str(newGlobalDispl)+addline
        inputFile=open('Master.inp','w')
        inputFile.writelines(lines)
        inputFile.close()


# After the appropriate constraint removal or displacement text files
# have been altered, the following function appends these blocks to the
# end of the previously created restart file.  It uses the following
# inputs: the name of the block to be appended (“Block”), the restart
# job name (“jobname”), and the previous step number (“stepnumber”).
# This function returns the new step number, along with an altered
# restart file corresponding to the restart jobname.  It also appends
# the same block to the master input file.
#
# After reading in the step number, this value is increased by one, and
# specific lines in the block are changed to reflect this.  This new
# block is then appended to the appropriate input files, and the new
# step number is returned.

def AppendBlock(Block, jobname, stepnumber):
      inputFile=open(str(Block)+'.txt')
      outputFile=open(jobname+'.inp','a')
      outputFile2=open('Master.inp','a')
      addline='\012'
      lines=inputFile.readlines()
      stepnumber=stepnumber+1
      for line in lines:
            if line[0:7]=='** STEP':
                  newLine='** STEP: Step-'+str(stepnumber)+addline
            elif line[0:6]=='*Step,':
                  newLine='*Step, name=Step-'+str(stepnumber)+',
nlgeom=YES, inc=100'+addline
            else:
                  newLine=line
            outputFile.write(newLine)
            outputFile2.write(newLine)
      inputFile.close()
      outputFile.close()
      outputFile2.close()
      return stepnumber

# This function helps the script to converge to an applied displacement
# that achieves a critical CTOD-situation at the largest measured CTOD.
# It uses the nested list, “minU2”, as an input and returns the next
# displacement increment.  This function is only called if all measured
# CTODs are less than critical.
#
# The convergence factor can be altered by the user.  But in this case,
# a factor of 1.5 is used.
#
# After reading in the measured and critical CTODs, the difference is
```

```
# calculated, and the smallest difference is multiplied by the
# convergence factor.  This value is then returned.

def DispConverge (minU2):
      maxU=1
      for i in range(0,5):
            if (minU2[i][2]-minU2[i][0]) < maxU:
                  maxU = minU2[i][2]-minU2[i][0]
                  displIncrement=1.5*(maxU)
      return displIncrement

# The function defined below takes in the previous pin displacement and
# the next calculated increment of displacement as inputs.  It alters
# the displacement block by adding this displacement increment.
#
# The text file, “displacementBlockMaster.txt”, must be pre-defined by
# the user.
#
# After opening the displacement block text file, this function
# searches for the node set, “Load”, which defines the point of applied
# displacement.  The value of applied displacement is then altered in
# the text file, then returned.

def AddDispl (globalDispl, displIncrement):
      inputFile=open('displacementBlock.txt')
      outputFile=open('displacementBlockNew.txt','w')
      lines=inputFile.readlines()
      for line in lines:
            if line[0:4]=='Load':
                  globalDispl=globalDispl+displIncrement
                  newLine='Load, 2, 2, '+str(globalDispl)+'\012'
            else:
                  newLine=line
            outputFile.write(newLine)
      inputFile.close()
      outputFile.close()
      inputFile=open('displacementBlockNew.txt')
      outputFile=open('displacementBlock.txt','w')
      lines=inputFile.readlines()
      for line in lines:
            newLine=line
            outputFile.write(newLine)
      inputFile.close()
      outputFile.close()
      return globalDispl
```

VITA

Christopher H. Abada

Christopher H. Abada was born in St. Louis, Missouri on May 10, 1979. He attended the University of Wisconsin – Madison, and received his Bachelor's degree in Engineering Mechanics in May, 2001. After graduation, he was employed by Johnson & Johnson as a Process Engineer in Roanoke, Virginia. He entered the Engineering Science and Mechanics Department at Virginia Polytechnic Institute and State University in September, 2003 to pursue his graduate degree. In June, 2004, he moved to Hampton, Virginia to continue his research through the National Institute of Aerospace at NASA Langley Research Center.